POLITECNICO DI MILANO

Facoltà di Ingegneria dei Sistemi

Corso di Laurea Specialistica in Ingegneria Fisica

TOWARDS FREQUENCY CONVERSION OF QUANTUM MEMORY COMPATIBLE PHOTONS FOR QUANTUM REPEATER APPLICATIONS

Relatore: Prof. Gianluca VALENTINI

Correlatore: Prof. Hugues DE RIEDMATTEN

Tesi di Laurea di:

Giacomo Corrielli

matr. 735645

Anno Accademico 2010-2011

CONTENTS

Contents **3**

List of figures **7**

Abstract **8**

Introduzione **10**

Introduction **12**

1 Quantum information **14**

1.1 Introduction to quantum information 15

1.1.1 The qubit 16

1.1.2 Qubits implementation 19

1.1.3 Quantum computation 19

1.2 Quantum communication 21

1.2.1 Quantum key distribution 21

1.2.2 Long distance quantum communication 23

1.2.3 Quantum repeater 24

1.2.4 DLCZ protocol 26

1.2.5 Quantum frequency conversion 30

1.3 State of the art on quantum frequency down conversion 32

2 Difference frequency generation **34**

2.1 Classical theory of the difference frequency generation 35

2.1.1 Difference frequency generation 35

2.1.2 Weak interaction approximation 37

2.1.3 Phase matching . . . 38
2.1.4 Quasi phase matching . . . 40
2.1.5 Three wave mixing . . . 42
2.1.6 Strong pump approximation . . . 43
2.2 Quantum properties of the DFG . . . 46
2.2.1 Particle picture of classical DFG . . . 46
2.2.2 Introduction to quantum optics . . . 48
2.2.3 Fock and coherent states . . . 49
2.2.4 Quantum description of DFG . . . 51
2.2.5 Simulated quantum regime . . . 53

3 Experimental setup and techniques 54
3.1 Experiment and setup description . . . 55
3.1.1 PP-KTP crystal . . . 58
3.2 Acousto-optic modulation . . . 60
3.2.1 Physical principles . . . 60
3.2.2 Setup use and double passage configuration . . . 61
3.3 Single photon counting . . . 63
3.3.1 Introduction . . . 63
3.3.2 Pin photodiodes, APDs and SPADs functioning . . . 64
3.3.3 ID Quantique Id201 SPAD . . . 68
3.3.4 SPAD use in the experimental setup . . . 69

4 Experimental results 71
4.1 DFG characterization in classical regime . . . 72
4.1.1 Light coupling into the WG . . . 72
4.1.2 Generation efficiency . . . 73
4.1.3 Temperature . . . 74
4.1.4 Conversion efficiency . . . 76
4.1.5 Dependence on the polarizations . . . 78
4.1.6 Total efficiency . . . 80
4.2 Conversion in the simulated quantum regime . . . 82
4.2.1 Noise characterization . . . 82
4.2.2 Global efficiency . . . 87
4.2.3 Estimation of the average number of 780 nm photons per input pulse . . . 88
4.2.4 Pulse creation . . . 90
4.2.5 SPAD synchronization . . . 90

4.2.6 SPAD measurement 92
4.2.7 Spad uncertainty 93
4.2.8 Pulse reconstruction 94
4.2.9 Comparison between expected and measured count rates . . . 95
4.2.10 SNR and gate width 96
4.2.11 Conversion performances 97
4.2.12 Photon length 99

Results discussion and conclusions **101**

Bibliography **109**

LIST OF FIGURES

1.1 (a)Entanglement creation in the elementary links, (b) iterated swapping operations, (c) entanglement distribution at distance L. Nodes connected by dotted arrows are entangled. ([1], fig. 1) 24
1.2 Comparison between time performances of direct transmission (A) and several QR protocols B-G. The line B correspond to the DLCZ protocol. ([2], fig. 18) 25
1.3 Schematic of the write and read process. ([3], fig. 2) 27
1.4 Laser cooled gas of rubidium atoms in a magneto optical trap (MOT) realized in QPSA group at ICFO (Barcelona). Ensembles of cold rubidium atoms are good candidates to operate as quantum memory. The atomic cloud (at approx. 40 μK) is the small bright dot in the middle of the laser cooling beams at 780 nm. 28
1.5 Scheme for entanglement creation in elementary links. ([3], fig. 3) . . 29
1.6 Scheme for entanglement swapping. ([3], fig. 4) 30

2.1 Difference frequency generation 36
2.2 Fractional variation of the generated intensity intensity as function of the wave vector mismatch 39
2.3 Comparison between the phase matched and non phase matched situations 39
2.4 Periodically poled material. The ferroelectric domains are periodically alternated. 41
2.5 Quasi phase matching DFG generation. 41
2.6 Conversion efficiency as function of pump power. 45
2.7 Virtual energy level scheme of the three wave mixing process. 47

3.1 Overview of the experimental setup 54
3.2 Experimental setup scheme. Legend: wave guide (WG), acousto-optic modulator (AOM), avalanche photodiode (APD), half wave plate (HW), quart wave plate (QW), polarization beam splitter (PBS), lens (L), aspheric lens (AL), fiber in/out coupler (IC/OC), diffraction grating (DG), dichroic mirror (DC), neutral density filter (NDF), interference filter (IF), photodiode (PD), polarization controller (PC), movable mirror (MM), pinhole (PH), temperature controller (TEMP), electronic sequencer (SEQ) 55
3.3 Neutral density filters 56
3.4 Signal (red) and pump (blue) light mixed through a dichroic mirror. . 57
3.5 Effect on 780 nm beam when the movable mirror is present (a) or not (b) 57
3.6 Filtering stage to isolate the 1550 nm light. 58
3.7 PP-KTP crystal 59
3.8 Aom phase matching condition. 61
3.9 Commercial AOM device, model MT110, from AA Optoelectronic . . 62
3.10 Variation of the absorption coefficient as function of the incident light wavelength for some semiconductor materials, commonly used in photodetectors fabrication. The telecom window lies in between the gray dashed vertical lines.// (Source: http://www.laserfocusworld.com/) . 64
3.11 a) Schematic of the pin photodiode structure and junction electric field intensity. b) Band curvature of the material in the junction and pair separation mechanism. 65
3.12 Pictorial representation of the avalanche. 66
3.13 Current-voltage characteristics of a diode. First, SPAD is biased above breakdown (state A). When the single photon detection event takes place it goes in the state B and the current pulse is generated. The quenching circuit bring the SPAD to the state C and finally the system is restored to the initial state A, ready to another detection. (source: id201 Single-Photon Detector, application note "Single-photon detection with InGaAs/InP avalanche photodiodes") . 67
3.14 Id201 photon counter module. 68
3.15 Signadyne control unit. 69
3.16 Bloch scheme of the synchronizing program. Pulse ON/OFF set to high/low voltage the output n.1 while Trigger ON/OFF set to high/low voltage the output n.2 70

4.1 Coupling efficiency of the signal (triangle) and pump (x), measured with respect to the input pump power. 73
4.2 1550 nm power generation vs 780 nm power coupled in the waveguide. In this measurement $P_{coup}^{1570} = 135mW$. 73
4.3 1550 nm power generation vs 1570 nm power coupled in the waveguide. In this measurement $P_{coup}^{780} = 21mW$ 74
4.4 Generation efficiency variations with 1570 nm coupled power. 75
4.5 Generation efficiency variations with 1570 nm coupled power. 75
4.6 Temperature scan. 76
4.7 PD2 calibration fitting. 77
4.8 Measure of the depletion of the signal beam. (continue line): coupled 780 nm light. (x): 780 nm power at the output of the waveguide. (diamonds): signal beam depletion. 78
4.9 Comparison between η_{coup}(x) and η_{gen} (dots) as function of the pump power. We can observe that, according to their definitions, they differ almost of a factor 2. 78
4.10 Crossed polarization measurement. The brighter is the color, the higher is the 1550 nm power recorded. The range is from 2µ to 1300 µW. 79
4.11 ϵ_{coup}^{780} and generation efficiency variation with 780 nm polarization direction. 79
4.12 ϵ_{coup}^{1570} and generation efficiency variation with 1570 nm polarization direction. 80
4.13 Counts/Trigger as function of the gate width, for different dead times. 83
4.14 Spectrum of the pump power after the amplifier. The vertical scale is logarithmic. The apparent limited signal to ASE ratio is caused by the fact that the resolution of the spectrum analyzer (0.02 nm) is larger than the pump laser line width. In practice, the peak intensity at 1570 nm is several orders of magnitude higher than the ASE. . . . 84
4.15 The pump spectrum (red) is filtered by DG1 (black) and then by IF2 (blue). 85
4.16 The pump spectrum (red) is filtered by DG1 (black), then by IF1 (green) and finally by IF2 (blue). 85
4.17 Noise level as function of the pump power with (red) and without (blue) IF1, measured with the SPAD 86
4.18 Noise level as function of the pump power, with IF1 86
4.19 Factor beta for a pulse FWHM of 45 ns. 88

4.20 PD1 calibration 89
4.21 Oscilloscope screen shots. (a) The TTL signal (blue) generates the light pulse (yellow) that reaches the photodiode with a certain delay. One horizontal division corresponds to $200ns$. (b) Detail of the pulse created using $t2 = 150ns$. We can observe that $\tau_p = 35.8\,ns$. One horizontal division corresponds to $20ns$. The image is displayed on the oscilloscope with the averaging mode. 91
4.22 Temporal scheme of the synchronization. 91
4.23 Pulse shape reconstruction obtained varying the delay between the pulse generation and the detection gate. The duration of the latter has been set on 2.5 ns. 94
4.24 Comparison between measured and expected click per gate. 95
4.25 f factor in function of τ. 96
4.26 SNR in function of gate width, for different input photons per pulse . 97
4.27 Signal detected as function of input average number of photons per pulse, with 20 ns gate width. 97
4.28 SNR in function average input photons per pulse, for different values of gate width. 98
4.29 SNR in function average input photons per pulse, in a region close to SNR = 1. 98
4.30 SNR in function of gate width. 99
4.31 Theoretical behavior of the conversion efficiency in function of the pump power, considering $\eta_{norm} = 0.13$ and $L = 2.6\,cm$. 103

ABSTRACT

The goal of this Master thesis is to assess experimentally the feasibility of implementing a quantum frequency conversion of quantum memory compatible photons, using a non linear interaction in a solid state device. In particular, we implemented a wavelength conversion experiment from 780 nm to 1550 nm, of weak coherent laser pulses, with temporal and spectral characteristics compatible with quantum memories based on cold Rubidium atomic ensembles. The purpose is the realization of an efficient and low noise setup that permits the detection of the converted light, using input pulses attenuated as close as possible to the single photon level. A successful result would allow the realization of a quantum interface between an atomic memory and the fiber optical network. This will represent a crucial step for the realization of long distance quantum information networks.

We implemented the down conversion via difference frequency generation, mixing the 780 nm pulses with a strong pump at 1570 nm in a periodically poled potassium titanyl phosphide waveguide, in quasi phase matching configuration. We first built the setup from scratch and we tested it using bright light. We then used weak coherent pulses as input and characterized the conversion performances with a single photon detector. In order to operate the system close to the single photon regime, the pump beam at 1570 nm as well as any spurious light at 1550 nm should be strongly suppressed. For this purpose, we used narrow interference filters and diffraction gratings, both to purify the spectrum of the pump light before the waveguide and to isolate the 1550 nm generated light after the conversion. The extinction ratio at 1570 nm of the filtering stage after the waveguide is > 110 dB.

The best conversion efficiency we obtained is 14% (in terms of converted/input photons), that, combined with the noise suppression level we achieved and the efficiencies of our detection setup, allows us to resolve the conversion of weak coherent

pulses (45 ns FWHM) at 780 nm containing an average number of photons around 100. In addition, we identified the main source of remaining noise and propose ways to reduce it. The results of this thesis, combined with the proposed improvement, are promising for the feasibility of a quantum frequency converter device with the aforementioned characteristics.

INTRODUZIONE

L'idea di sfruttare le proprietà prettamente quantistiche delle particelle atomiche e della luce per sviluppare una tecnologia rivoluzionaria da applicare all'elaborazione e alla trasmissione dei dati è studiata teoricamente da diversi decenni. Una delle più notevoli applicazioni pensate in questo campo è l'invenzione della crittografia quantistica e, più precisamente, dei protocolli di Quantum Key Distribution (QKD): un sistema intrinsecamente sicuro, basato su tecnologia fotonica, che sfrutta le proprietà quantistiche dei fotoni. Negli ultimi anni, molti gruppi di ricerca nel mondo hanno iniziato ad occuparsi di questi argomenti anche da un punto di vita sperimentale e i progressi sono stati tali che è già possibile incontrare sul mercato dispositivi che permettono di inviare e ricevere dati tramite canali quantistici sicuri.
Alla luce delle tecnologie attuali, la trasmissione d'informazione quantistica (qubit) è affidabile solo per distanze dell'ordine di centinaia di km e ciò è dovuto al fatto che la trasmissione di un segnale ottico è soggetta a perdite e attenuazione, sia in propagazione libera che in fibra ottica. Inoltre, a causa del teorema di "no-cloning", un'amplificazione classica di un segnale quantistico ne degraderebbe completamente l'informazione che esso trasporta. La soluzione più promettente per ovviare a questo problema è rappresentata dalla costruzione di un sistema denominato "quantum repeater", il cui funzionamento sfrutta una delle caratteristiche più affascinanti offerte dalla meccanica quantistica: l'entanglement. La prima proposta di implementazione pratica di un quantum repeater è dovuta a Duan, Lukin, Cirac e Zoller, (DLCZ) nel 2001. Questo schema prevede la creazione di un'eccitazione atomica collettiva in un ensemble di atomi (usato come "quantum memory") che sia fortemente correlata con l'emissione di un fotone Stokes. Esso viene poi inviato a grande distanza dove, tramite una misura congiunta con un altro fotone Stokes proveniente da un'altro ensemble, viene creato lo stato di entanglement fra le due quantum memories. La

trasmissione dei fotoni emessi dagli atomi, tipicamente nel visibile o vicino infrarosso, avviene in fibra ottica, dove l'attenuazione per queste lunghezze d'onda è molto marcata. Per migliorare le prestazioni di un quantum repeater di questo tipo è quindi necessario un dispositivo addizionale che permetta la conversione della lunghezza d'onda dei fotoni Stokes dalle frequenze delle transizioni atomiche alla cosiddetta "C-band" delle telecomunicazioni (1530 nm ÷ 1565 nm), dove l'attenuazione in fibra è la minima possibile (0,2 dB/km).
Lo scopo di questa tesi è di sviluppare un esperimento di conversione di lunghezza d'onda da 780 nm a 1550 nm, che possa essere utilizzato per convertire singoli fotoni provenienti da una quantum memory realizzata con atomi freddi di rubidio (^{87}Rb). La conversione avviene tramite il processo non lineare di generazione di frequenza differenza (DFG), realizzato combinando luce laser coerente a 780 nm con un fascio di pompa a 1570 nm, in una guida d'onda fabbricata in periodically poled potassium-titanyl-phosphate (PP-KTP). L'esperimento è stato eseguito in diversi passi:

- scelta degli elementi ottici e costruzione dell'apparato sperimentale;
- caratterizzazione ed ottimizzazione del processo di DFG in regime classico;
- esecuzione dell'esperimento in regime quantistico "simulato", usando impulsi di luce coerente fortemente attenuati e tecniche di conteggio di singolo fotone.

Nel primo capitolo verrà presentata una breve panoramica generale sull'informazione quantistica e una descrizione dello schema DLCZ, con lo scopo di contestualizzare l'esperimento eseguito in questo scenario. Nel secondo capitolo verranno presentati alcuni risultati teorici riguardo al processo di DFG, che verranno dapprima ricavati seguendo un formalismo classico ed in seguito ne verranno evidenziate le caratteristiche quantistiche. Nel terzo capitolo presenterò l'apparato sperimentale costruito e le principali tecniche utilizzate. Nel quarto capitolo, infine, verranno esposti e discussi i risultati ottenuti nell'esperimento.

L'intero lavoro è stato condotto nei laboratori del gruppo "Quantum Photonic with Solid and Atoms" (QPSA), guidato dal prof. Hugues de Riedmatten, presso l'"Institut de Ciencies Fotoniques" (ICFO), Castelldefels (Barcelona, Spain). Quando ho preso parte a questo progetto, il gruppo QPSA era di recentissima fondazione e quindi, durante i primi mesi della mia permanenza in ICFO, ho avuto l'opportuità di contribuire direttamente nell'allestimento da zero dei laboratori.

INTRODUCTION

The idea of exploiting purely quantum properties of particles and light to develop a revolutionary technology suitable for processing and transmission of data has been studied theoretically for several decades. One of the most remarkable application in this field is the invention of quantum cryptography and, more precisely, the Quantum Key Distribution's protocols (QKD) which is an intrinsically safe system based on photonic technology that relies on the quantum properties of photons. During the last years, many research groups in the world started to study these topics also from the experimental point of view and the progress has been so fast that is already possible to find commercial devices that allow to send and receive data through a secure quantum channel.

Nowadays photonic technology permits a reliable transmission of bits of quantum information (qubits) only over few hundreds of km, because of the loss and the attenuation that affect the optical signal, both in free space and in fiber propagation. Moreover, a classical amplification of a quantum signal is impossible because, according to the so called "no-cloning" theorem, it would degrade the information that it is carrying. The main and most promising solution proposed to overcome this problem is the implementation of a "quantum repeater". It is a sophisticated method that permits to distribute qubits over long distances (thousands of km), exploiting one of the most fascinating and non-classical features of quantum mechanics: entanglement. The first practical scheme to realize a quantum repeater was proposed by Duan, Lukin, Cirac and Zoller (DLCZ) in 2001. One of the requirements of this scheme is to create single atomic excitations in an atomic ensembles (used as "quantum memory") that are strongly correlated with Stokes photons emitted during the process. These Stokes photons should be sent as far as possible to then perform a joint measurement with another Stokes photon coming from another ensemble, in

order to establish an entangled state between the two distant quantum memories. The transmission of the Stokes photons is done via optical fiber but the photons emitted by the ensembles lie in the visible and near infrared range of the electromagnetic spectrum, depending on the atomic species used (typically rubidium or cesium). To improve the scheme is thus necessary an additional setup that converts the wavelength of the Stokes photons, from atomic resonances to the typical telecommunication C-band (1530 nm $\div$ 1565 nm) for which the attenuation in fiber is the lowest (around 0,2 dB/km) and so allows long distance transmission.
The aim of this thesis work is to build and optimize an optical setup to realize a wavelength conversion experiment from 780 nm to 1550 nm that could be used to convert Stokes single photons coming from a quantum memory realized with a gas of cold atoms of rubidium (^{87}Rb isotope). The conversion takes place via a Difference Frequency Generation (DFG) process, realized mixing 780 nm coherent laser light with a strong pump at 1570 nm in a non linear periodically poled potassium titanyl phosphate (PP-KTP) waveguide. The experiment was carried out in three steps:

- the choice of the optical elements to construct from scratch the setup
- characterization and optimization of DFG in classical regime
- to run the experiment in a "simulated" quantum regime using strongly attenuated coherent pulses, after an appropriate noise suppression that allows Single Photon Count (SPC) measurements

In the first chapter I present a short overview on quantum information and a brief description of the DLCZ quantum repeater's protocol, to contextualize the purpose of my experiment. In the second chapter I analyze theoretically the DFG process according to its classical non linear optics description and I will underline its quantum features. In the third chapter I describe the experimental setup and the techniques I used and in the last chapter I show and discuss the experimental results I obtained.

The entire work has been done in the labs of "Quantum Photonic with Solid and Atoms"(QPSA) group headed by the prof. Hugues de Riedmatten at the "Institut de Ciencies Fotoniques" (ICFO), Castelldefels (Barcelona), Spain. When I joined ICFO, the group had just been founded and thus, in the beginning, I had the chance to contribute in the setting up the labs from scratch.

CHAPTER 1

QUANTUM INFORMATION

The aim of this chapter is to insert the experiment of quantum frequency conversion that has been carried out in this thesis work in the quantum information scenario.

In the beginning I present a brief introduction to this field and the basic underlying physical tools. I will then show the main goals of quantum communication, how a quantum repeater could help in realizing long distance quantum data transmission and why a single photon frequency converter represents an improvement to this architecture.

The purpose of this chapter is to explain the revolutionary features that quantum mechanics can offer to information science, more than a rigorous description of the phenomena, that is beyond the scope of this thesis. For a more detailed treatment I refer to bibliography.

1.1 Introduction to quantum information

Information is a key concept of our everyday life. Humans, since their appearance on the world surface, constantly exchange information with each other. The progresses in technology opened gradually new possibilities in storing, processing and transmitting data.
During human history, information technology progressed astonishingly. The invention of semiconductor transistors in 1948 paved the way to the solid state computation, while the mid-nineteenth century studies on electromagnetism started the so-called telecommunication era. Nowadays we are able to store in a $1\,cm \times 1\,cm$ chip an amount of information equivalent to thousands of books and we can perform in a second a number of logic operations that would require hundreds of years to a human's brain.
It is remarkable that the performances obtainable in manipulating information are strongly correlated to the physical media that we chose to codify and transmit it. Translating data in electromagnetic waves instead of written papers allowed the evolution of the rapidity of long distance communication, from the speed-of-horses to the speed of light.

The actual digital information science is fully based on the concept of bit. It is the basic brick of data coding. A bit is a physical binary system whose state can be set only on two distinct possibilities, namely 0 and 1. The only requirement is that there must be a sufficiently large energy barrier between them, to avoid spontaneous transitions of the bit from one state to the other [4]. Different systems are chosen with respect to the particular application. In the hard disk, a bit is the magnetization state of a thin magnetic layer. In optical communications it is the presence or absence of a light pulse. In the microprocessors, the information is coded as high or low voltage in a transistor and it is processed by small solid state logic gates. Let us focus the attention on the latter example. Moore's empirical law states that we can double the processing speed of a computer every 18-24 months. It seems that the only way to make them significantly faster is to make the processors smaller and smaller, multiplying the number of bits and logic gates per chip. In addition to economics and other practical considerations, it is evident that this scenario has an unavoidable limit. The scalability of the transistors cannot go below atomic or molecular dimensions [5]. Moreover, the effects of quantum mechanics at this length scale would become more and more important. In 1982, Richard Feynman proposed a solution to overcome this problem [6]. He thought that the counter-intuitive laws of quantum mechanics can be used not only to optimize the classical computation

performed with atomic devices, but, more radically, to develop a totally new and revolutionary information processing technology. This opened the door to the so-called quantum information science.
Many theoretical works demonstrated that exploiting purely quantum effects, like coherent states superposition and entanglement, it is possible to implement algorithms to obtain results that are unaccessible to classical information devices, both in computation and in data transmission [7],[8],[9].

1.1.1 The qubit

Quantum information is based on the concept of quantum bit (qubit), the quantum counterpart of the classical bit. Any quantum system with two different states, called $\mid 0\rangle$ and $\mid 1\rangle$, related to an observable quantity Q, can be used as qubit [10]. We will see in this section three different qubit features not obtainable with classical bits: coherent superposition, entanglement and the impossibility of qubit cloning.

Coherent superposition of states

A generic two level quantum system is described by a wave function $\mid \Psi\rangle$ that belongs to a bi-dimensional complex Hilbert space. It can be written as:

$$\mid \Psi\rangle = \alpha \mid 0\rangle + \beta \mid 1\rangle \tag{1.1}$$

were α and β are two complex coefficients that must obey the normalization condition:

$$|\alpha|^2 + |\beta|^2 = 1 \tag{1.2}$$

The meaning of the expression (1.1) is that the state of the system is a coherent superposition of the basis states $\mid 0\rangle$ and $\mid 1\rangle$. A measurement of the state of the qubit on this basis[1] will give the outcome $\mid 0\rangle$ with probability $|\alpha|^2$ and $\mid 1\rangle$ with probability $|\beta|^2$. Moreover, the state $\mid \Psi'\rangle$ of the qubit after the measurement collapses on the value determined by the outcome [11].
A qubit can be prepared also in a well defined state, eg. $\mid \Psi\rangle = \mid 0\rangle$, and the result of a measurement of Q is no longer probabilistic. However, we can measure the state of this qubit with respect to another basis $\{\mid A\rangle, \mid B\rangle\}$, not orthogonal to the previous[2], such that:

$$\mid 0\rangle = \gamma \mid A\rangle + \delta \mid B\rangle \tag{1.3}$$

[1] a measurement of Q.

[2] this means to measure another observable quantity Q' related to the qubit that is not compatible with Q, with possible outcomes $\mid A\rangle$ and $\mid B\rangle$.

In this case we would again get a probabilistic result and the state of the qubit will collapse either in $\mid A\rangle$ or in $\mid B\rangle$. The vice versa is also true. A qubit prepared in a coherent superposition state can be always measured with respect to some basis in which its state is well determined [10].
The classical bits don't exhibit such a feature. Their state, even if it is unknown, is always well defined. An ensemble of them can be, at most, prepared in a statistical mixtures, namely a collection of bits either in the state 0 or 1. Again, the outcome of the measurement on a bit randomly chosen in this ensemble will be probabilistic, but in the weaker sense that we are simply not able to predict a priori what it already is. There is no way to change its state just with the measurement act.

Entanglement

If we consider a system constituted of two classical bits, there are four distinct possibilities concerning its state. They can both assume the value 0, the value 1, the first can be 0 and the second 1 and vice versa. More generally, if we have a system constituted of n bits, its state is always well defined and can assume 2^n well determined possible values.
The behavior of a n qubits system is radically different. For simplicity, let us focus the attention on the case of $n = 2$. If we are able to distinguish the two qubits, in the sense that, from their history, it is possible to know the state of each of them without performing a measurement, the wave function that describes the system $\mid \Psi_{tot}\rangle$ is simply the product of the wave functions of the individual qubits:

$$\mid \Psi_{tot}\rangle = \mid \Psi_1\rangle \otimes \mid \Psi_2\rangle = \mid \Psi_1\Psi_2\rangle \tag{1.4}$$

On the other hands, there are situations in which, for example due to an interaction between the two qubits, their states are not independent, but nothing can be stated about one, without performing a measurement on the other. In this case the wave function that describes the state of the overall system will be a coherent superposition of the different possibilities [12].
Let analyze this example: consider a spin 0 particle that spontaneously decays into two spin 1/2 particles p_1 and p_2, that fly off in opposite directions[3]. Because of the conservation of the angular momentum, the projections of the spin of the two particles on a particular direction must be opposite. If p_1 were in the state $|\uparrow\rangle$, then p_2 would be in the state $|\downarrow\rangle$, and vice versa. The two scenarios are equiprobable

[3]That's the case, for example, of a pion π at rest that decays in an electron e^- and a positron e^+. This example is the simplified version, due to David Bohm, of the one that Einstein, Podolsky and Rosen proposed in 1935, known as EPR paradox [13].

and, before measuring the spin of one of the two particles, it is impossible to know which is in which state. The total wave function of the two particles, before any measurement, is thus written as:

$$\mid \Psi_{tot}\rangle = \frac{1}{\sqrt{2}} \left(|\uparrow_1\downarrow_2\rangle \pm |\downarrow_1\uparrow_2\rangle\right) \tag{1.5}$$

Such states are called entangled and they cannot be written as product states. Similarly to what happens in single qubit states superposition, is the act of the measurement on one of them that determines (probabilistically) in which state the two qubits are [14].
The possibility to have entangled states is not confined to two qubit systems. They can emerge in any system composed of many qubits.
Entanglement leads to a very intriguing consequence. Since two entangled qubits can be put arbitrarily far apart, this instantaneous effect that the measurement on one causes to the other leads to non local correlations that manifests in violation of the so-called "Bell's inequality" [15],[16],[17]. These strong correlations are a crucial tool in quantum information science. Violations of Bell's inequality are impossible to obtain with correlations between classical bits and this proves that there is no way to simulate entanglement with them.
It is important to highlight that an interaction between two qubits is not necessary to establish an entangled state between them. Let us imagine two pairs of entangled qubits; the qubit A is entangled with B and C is entangled with D. A joint measurement on the states of the qubits B and C, performed in the same basis of the entangled states, establishes entanglement between A and D. This procedure is called "entanglement swapping" and allows to entangle systems that may have never interacted. We will see that entanglement swapping is the central concept in the realization of a quantum repeater [1].

No cloning theorem

We see now the third fundamental difference between classical and quantum bits. The latter exhibit a characteristic that seems trivial at first sight: they can be copied. Given a bit in a certain state, it is always possible to prepare an arbitrary large amount of bits in the same state, even it is unknown, without perturbing the original. This possibility is no longer valid if we want to operate with qubits [18]. This concept is expressed by the so-called "no cloning theorem", introduced in 1982 by Dieks, Wootter and Zurek [19]. It states that it is impossible to build a machine that is able to prepare perfect copies of the generic and unknown state of a qubit via operations that preserve its quantum properties. The existence of such

a machine would lead to contradictions with the quantum mechanics and special relativity axioms [18]. It's important to highlight that this theorem no longer holds either if we allow the machine to prepare imperfect copies of the qubit or whether its state is not general, e.g. if we know from the beginning that it is well defined with respect of a certain basis [20]. Nevertheless, these restrictions on the qubits clonability have no classical counterpart.

1.1.2 Qubits implementation

A two level quantum system can be used in practice as a qubit if we can prepare it in some well defined initial state and if it is possible to measure it after its time evolution. The latter must be unitary, in the sense that it can transform the state of the qubit, without affecting its coherence properties [11]. The phenomenon of coherence loss is related to the interaction of the qubit with the surrounding environment. This can destroy its quantum features like superposition and entanglement and degrades the information that it is carrying [21].
Different experimental qubit implementations have been proposed and realized during recent years. We can divide them in two classes:

1. Stationary qubits: they are suitable for quantum processing and quantum storing of data.

2. Flying qubits: they are ideal for quantum transmission of information.

The former are mainly based on atomic and solid state physics systems. Stationary qubits have been realized, for instance, with trapped ions [22], single neutral atoms[23], spin of molecules nuclei [24], electrons in superconductive structures [25], quantum dots [26], etc. On the other hands, flying qubits are implemented with quantum states of light [9].

1.1.3 Quantum computation

We saw that quantum mechanics offers different features that are impossible to obtain with classical bits. Several theoretical works demonstrated that the computational performances obtainable exploiting coherent superposition and entanglements in solving a certain class of problems can be much superior compared to what a classical processor offers.
The most remarkable example concerning the difference between classical and quantum computation is how they face the problem of the integer factorization. The time required to a classical computer to perform this task, no matter its speed, grows

almost exponentially with respect to the size of the input number N to factorize. In 1994, Peter Shor discovered a quantum algorithm that would permit, with qubits and quantum logic gates, to carry out the same operation, but in a polynomial time [7]. This change in the time scaling law is a radical enhancement not achievable with classical processor improvements.

The analog counterpart of a quantum computer, the so-called "quantum simulator", could be used to emulate very efficiently the evolution of quantum mechanical systems that are too complex to be simulated with a classical computer [27]. This would have strong repercussions on fundamental research, but may also have a strong impact in applied research, e.g. to design new materials or molecules.

Although first simplified experimental implementations of the Shor's algorithm have already been implemented [28],[28], a digital quantum computer is still far from a practical realization. The main factor that limits its construction is that it would require the control on the evolution of hundreds or thousands of qubits, avoiding the phenomenon of coherence loss. Its scalability also is a non trivial problem because of the sophisticated experimental techniques involved in the qubits and quantum logic gates practical implementations. In this sense, quantum simulation is more promising in the short term, because less qubits are needed. First interesting experiments have been done recently, e.g. simulating magnetic spin structures using ultra-cold degenerate Bose atoms trapped in optical lattices [29].

In the next paragraph we will see that the results of quantum information closer to technological applications are related to the progresses made in quantum communication, more than in data processing.

1.2 Quantum communication

Quantum mechanics can be used not only to improve the computation power of the actual processors, but also gives unique contributions in data transmission. This field, called "quantum communication", developed much faster in recent years than quantum computation. The reason is that the technological challenges to achieve the main goals of quantum communication revealed to be much easier to overcome experimentally. Quantum optics and photonic techniques are widely employed in practical quantum communication realizations and the qubits are implemented with photons. Progresses have been so successful that it is already possible to buy commercial quantum communication devices [30] and small quantum communication networks are fully operational since several years [31].
The first, simpler application in this direction is the so-called "dense coding protocol", with which Alice can send to Bob[4] two bits of classical information, sending him just one member of an entangled qubit pair [32]. Another scheme, called "quantum teleportation", allows Alice to transmit a quantum state to Bob, just sending a finite amount[5] of classical bits, provided that they share an entangled pair of qubits [33]. This protocol is crucial for long distance transmission of quantum information, as we will see in § 1.2.3. Quantum teleportation could be of practical interest also for quantum computation, for example in the transfer of quantum information between different units of a quantum computer. Experiments in dense coding and teleportation have already been successfully carried out [34],[35]. However, the most remarkable contributions in data transmission provided by quantum mechanics are indeed represented by those given to cryptography [36].

1.2.1 Quantum key distribution

Let us first explain few basic concepts about classical cryptographic systems. They can be divided in two different classes:

1. the "private key" systems, in which Alice and Bob encrypt and decrypt their messages by means of a secret private key (a word or a string of numbers) that they share. The security of this systems resides in the secrecy of the key[6].

[4] In quantum communication language it is common to identify two general communicating parties as Alice and Bob.

[5] note that, since a generic quantum state is parameterized by two continuous variables α and β, its description with arbitrary accuracy would require an infinite amount of classical bits.

[6] The so-called "Vernan's cypher" or ("One time pad") private key cryptosystem is the only cryptographic scheme whose inviolability is mathematically proven [37].

Since the key must be at some time distributed between Alice and Bob, there is always the risk that it is intercepted by a third evil-minded party (Eve);

2. the "public key" systems, where Alice and Bob don't share any secret key. In this case Bob makes public a key that Alice can use to encrypt a message. But this key alone cannot be used to decrypt it. This operation can be done only using the public key together with a secret key, possessed by Bob alone. In this way everybody can encrypt a message but only Bob can decrypt it.

In public key cryptosystems, dangerous secret keys distributions are avoided and this limits enormously Eve's potential attacks. Nevertheless also this systems are far from be 100% unbreakable. Bob's secret key and the public key are not independent. The former is always used to calculate the latter by means of some algorithm f. The security of this systems resides in the complexity of computing f^{-1} to obtain the secret key starting from the public one.
The most relevant example of public key cryptosystem is the so called "RSA protocol"[7], still widely employed. To brake it it's necessary to factorize an integer number N in his two prime factors p and q. Despite this operation is impossible for actual technology if p and q are large enough, we saw in § 1.1 that the hypothetical construction of a quantum computer would permit to carry out this task efficiently. In addition, theoretical discoveries in prime numbers theory could bring to the realization of efficient classical factorization algorithms. Both this events would allow to break the RSA protocol [38].
Quantum mechanics can help in breaking public key systems, but gives a unique enhancement to the security of private key cryptography. With the quantum key distribution (QKD) protocols, Alice can send to Bob a secret key, encoded in a string of qubits, being sure that nobody eavesdropped their communication.
The concept at the heart of QKD is that Eve, in order to eavesdrop the key sharing, must measure the state of the qubits stream before Bob. This leads to unavoidable modifications of the qubits states and this can be detected by Alice and Bob. For example, in the QKD protocol called "BB84"[8], that exploits the qubit states superposition, they can detect an Eve's attack, by a statistical analysis on the error rate introduced during the communication [9]. Another example is the "E91" protocol[9], where Alice and Bob share pairs of entangled qubits. In this case, the eavesdrop can be discovered with the analysis on the correlations of the outcomes of their measurements [39].

[7]Introduced in 1977 by Rivest, Shamir and Adleman.
[8]invented by Bennet and Brassard in 1984.
[9]due to Ekert, 1991

If Eve possessed a machine able to create a copy of the qubits without perturbing their state, she could avoid to measure directly the qubits stream between Alice and Bob and thus she could intercept the key distribution without leaving a trace. In practice, due to the no cloning theorem, this is impossible and so the security of the QKD protocols must be considered intrinsically unbreakable.
Recently, some papers have reported hacking of commercial cryptosystems [40]. Nevertheless, it cannot be related to weaknesses in the protocol itself because the attack performed to this QKD system only exploited some non idealities of the experimental apparatus, in particular the limited detection efficiency of the single photon detectors. While the QKD protocols are in principle perfectly secure, their actual implementations must be carefully checked against potential imperfections that could be exploited by the eavesdropper. Improvements in existing technology would lead to perfectly secure cryptosystems.

1.2.2 Long distance quantum communication

The enhancement of the maximum distance at which a quantum state can be distributed is essential, e.g. for long distance QKD and for the construction of wide quantum networks. Photons represent the natural flying qubit carriers and, so far, they are indeed the only candidates to play this role. The maximum distance for photons transmission is limited by the loss and decoherence that affect optical fibers and the free space propagation. As first approximation, the decoherence of quantum states of light in this channels can be neglected, so, practically, the main limitation in quantum states distribution is photon loss [41]. It causes an exponential drop in the qubits transmission rate with respect to the line length. For example, typical telecommunication optical fibers have losses of 0.2 dB/km in the optimal wavelength range of 1.55 μm. Hypothesizing a photon rate source of 10 GHz (that however is very ambitious for a source of quantum states), the transmission rate after 100 km fiber would be 100 MHz. It would drop to 1 Hz after 500 km and to 10^{-10} Hz (a photon each 300 years) for a transmission of 1000 km. In classical telecommunications this problem is overcome through the use of optical amplifiers. This solution, according to the no cloning theorem, is no longer applicable to a stream of qubits, since, as we discussed, its regeneration is allowed only under strict conditions that would degrade the photon quantum states [1].

1.2.3 Quantum repeater

One possible solution for long distance quantum state distribution is given by the implementation of the so-called "quantum repeater" (QR) architecture, first proposed by Briegel in 1998 [42]. Its goal is to distribute entangled states over long distances. Let us imagine that we want to send a quantum state between two locations A and Z, separated by a great distance L, and a direct transmission is not possible because of the loss. If we had two entangled quantum systems in A and in Z, we could transmit quantum information over L with classical bits, thanks to the quantum teleportation protocols. In addition we could use such systems to perform entanglement based QKD, like the E91 scheme.
The main idea at the heart of a quantum repeater is that the entanglement over L can be established by subsequent entanglement swapping operations, starting from the elementary creation of entangled states at distances accessible to direct qubits transmission [1]. The functioning of a quantum repeater is summarized in figure 1.1. The entanglement is first established between short elementary links: A-B,

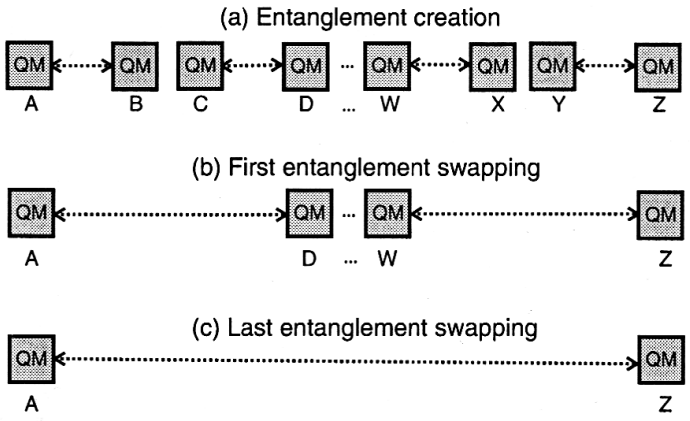

Figure 1.1: (a)Entanglement creation in the elementary links, (b) iterated swapping operations, (c) entanglement distribution at distance L. Nodes connected by dotted arrows are entangled. ([1], fig. 1)

C-D, ...,W-X, Y-Z. It is then swapped to create longer links A-D, ...,W-Z via direct photon transmission. The swapping operations between adjacent nodes are iterated until entanglement is distributed over the total distance L.
There are three essential requirements to distribute entanglement with this scheme:

1. the entanglement creation between the elementary links must be heralded by some detectable event that assure that this operation has been successfully carried out;

2. the entanglement established in the elementary links must be "stored" until it is successfully done in all the neighboring links as well, before starting with the swapping operations. For this reason, each node of the chain must behave as "quantum memory";

3. it must be possible to perform the entanglement swapping between adjacent quantum memories. Doing this deterministically is generally a difficult task. Using linear optics, it is possible to implement entanglement swapping with a success probability of up to 0.5.

Beyond this fundamental requirements, there are other improvements in the quantum repeater architecture, such as entanglement purification and error corrections, that become very important when the complexity of the system grows and the effects of decoherence are no longer negligible.
All these operations can be done in several ways and different schemes have been proposed [43].
In figure 1.2 we can see a numerical simulation of the temporal performances of different quantum repeaters protocols compared with direct lossy transmission channels presented in a recent review on the topic [2]. In particular, we can see how the

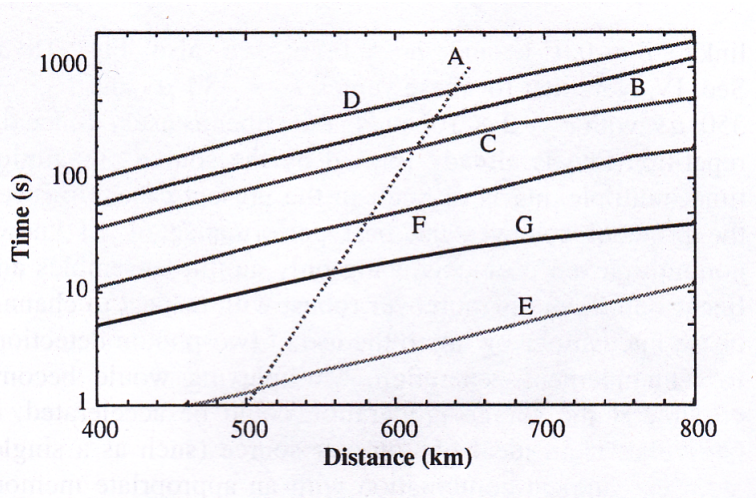

Figure 1.2: Comparison between time performances of direct transmission (A) and several QR protocols B-G. The line B correspond to the DLCZ protocol. ([2], fig. 18)

time required for a single entangled state distribution grows with respect to the total distance L. It is remarkable that, for a total length greater than 500-600 km, the quantum repeater outperform direct transmission and, thanks to the different scaling, the former is definitely much faster.
Despite several technological challenges still have to be overcome for a practical re-

alization of a quantum repeater, this research field is very active and the first results are very promising.

1.2.4 DLCZ protocol

We now analyze in detail one of the first quantum repeater implementation scheme, proposed by Duan, Lukin, Cirac and Zoller in 2001 (the DLCZ protocol), that highly influenced all the subsequent QR proposals [44].
The DLCZ protocol makes use of atomic ensembles as quantum memories and linear optics combined with single photon counting techniques to perform the operations of entanglement swapping and elementary entanglement creation.

Quantum memory

Let us analyze how an atomic ensemble can be used as quantum memory in the DLCZ scheme[3].
Let us consider that an ensemble of N atoms of a specific element is confined in a small region. The basic requirement for the atomic specie used is that it behaves as a three level lambda system, with two ground states $\mid g_1\rangle$ and $\mid g_2\rangle$ and one excited state $\mid e\rangle$. The two ground states are connected to an excited state with allowed optical transitions. Let us suppose also that all the N atoms are initially in the ground level $\mid g_1\rangle$ and this corresponds to the state $\mid 0\rangle$ of the memory, that can be written as:

$$\mid 0\rangle = \prod_{i=1}^{N} \mid g_1\rangle_j \tag{1.6}$$

where the subscript denotes the j_{th} atom of the ensemble.
A red detuned laser pulse (called write pulse) on the $g_1 \rightarrow e$ transition leads, with a small probability p, to the spontaneous emission of a Raman photon on the $e \rightarrow g_2$ transition, together with the promotion of one of the atoms to the $\mid g_2\rangle$ state. The detection of this photon (called Stokes photon according with the usual Raman scattering terminology) in the far field erases any information about which atom it comes from, and thus the single excitation is delocalized over the whole ensemble. This corresponds to the state $\mid 1\rangle$ of the memory and can be written as:

$$\mid 1\rangle = \frac{1}{\sqrt{N}} \sum_{j=1}^{N} e^{i(\vec{k}_w - \vec{k}_s)\cdot\vec{x}_j} \mid g_1\rangle_1 \mid g_1\rangle_2 ... \mid g_2\rangle_j ... \mid g_1\rangle_N \tag{1.7}$$

where $\vec{k}_w$ and $\vec{k}_s$ denotes the wave vectors of the write pulse and the Stokes photon respectively and $\vec{x}_j$ is the position of the j_{th} atom. The (1.7) expresses the coherent superposition of states in which each atom is in the level g_1 except the j_{th} that is in

the level g_2.

It is important to underline that the probability p of the stokes photon emission[10] in

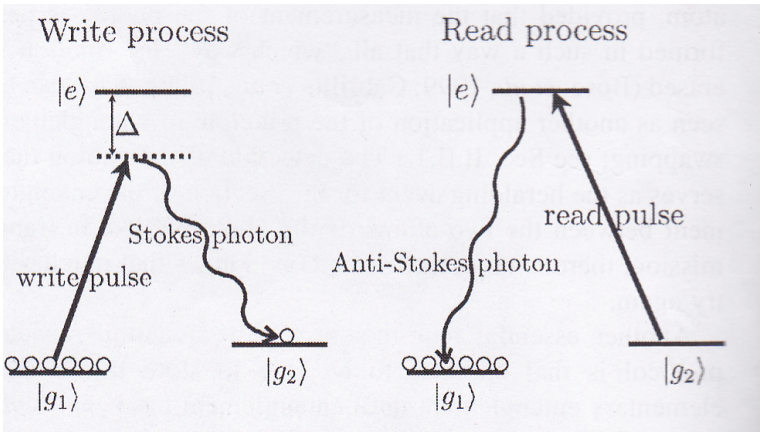

Figure 1.3: Schematic of the write and read process. ([3], fig. 2)

the detected mode must be small enough, in order to avoid the processes of multiple n-photons emission, that take place with probability p^n.

Another requirement is that the lifetime of the level $\mid g_2\rangle$ is as long as possible to avoid spontaneous relaxation of the state of the memory from $\mid 1\rangle$ to $\mid 0\rangle$.

Let us consider now that a strong laser pulse (called read pulse), resonant with the transition $g_2 \rightarrow e$ hits the ensemble region while it is in the state $\mid 1\rangle$. The read pulse leads to the emission of an anti-Stokes photon, resonant with the $e \rightarrow g_1$ transmission, and set again the total state to $\mid 0\rangle$. This process can be carried out very efficiently, due to a collective interference emission process, if the following phase matching condition is satisfied:

$$\vec{k}_S + \vec{k}_w = \vec{k}_{AS} + \vec{k}_r \tag{1.8}$$

where $\vec{k}_r$ and $\vec{k}_{AS}$ denotes the wave vectors of the read pulse and the Stokes photon respectively. The write and read process are depicted in figure 1.3.

The most important feature of the quantum memory is that the Stokes photon emission is strongly correlated with the creation of the collective atomic excitation. The detection of such a photon heralds that the memory is the state $\mid 1\rangle$.

The fundamental requirements for such a memory to work efficiently in a quantum repeater architecture are high storage time, high excitation retrieval efficiency and high quantum correlation between Stokes and anti-Stokes photons emitted. Different performances are achievable depending on the experimental realization.

The main systems studied to implement a quantum memory are solid state host

[10] p depends to the write pulse intensity, its detuning Δ, N, and the strength of the $g_1 \rightarrow e$ and $e \rightarrow g_2$ transitions.

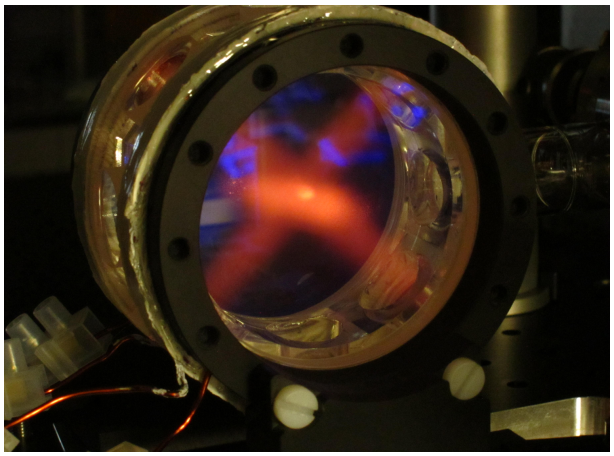

Figure 1.4: Laser cooled gas of rubidium atoms in a magneto optical trap (MOT) realized in QPSA group at ICFO (Barcelona). Ensembles of cold rubidium atoms are good candidates to operate as quantum memory. The atomic cloud (at approx. 40 μK) is the small bright dot in the middle of the laser cooling beams at 780 nm.

crystals doped with rare earth ions and atomic gases (cold and hot). [45],[46]. So far only the latter have been used as DLCZ type quantum memory while both have been exploited in other schemes, e.g. to absorb, store and reemit single photon qubits.

Elementary entanglement creation

We will se now how a memory based on a atomic ensemble can be used to establish the elementary entanglement necessary for the realization of a quantum repeater [3].
Imagine that we have two quantum memories A and B at a distance L_0 such that the attenuation over $L_0/2$ is low enough to allow efficient direct fiber transmission. In addition, the possible stokes photons emitted by the two ensembles are fiber coupled and sent to a intermediate station between them, where they are combined via a 50/50 beam splitter and detected by two single photon counters. This situation is depicted in figure 1.5. At the beginning both the memories are prepared in their $\mid 0\rangle$ state. The total wave function of the system is thus:

$$\Psi_{AB} = \mid 0_A 0_B\rangle \tag{1.9}$$

Two write pulses are simultaneously sent to the ensembles such that a single Stokes photon is emitted with the small probability p by one of the two. This photon has the same probability to be detected by d or $\widetilde{d}$, either if it comes from the memory A or the memory B. In addition we saw that the emission of such a photon by one ensemble is strongly correlated to the creation of en atomic excitation in it. Thus,

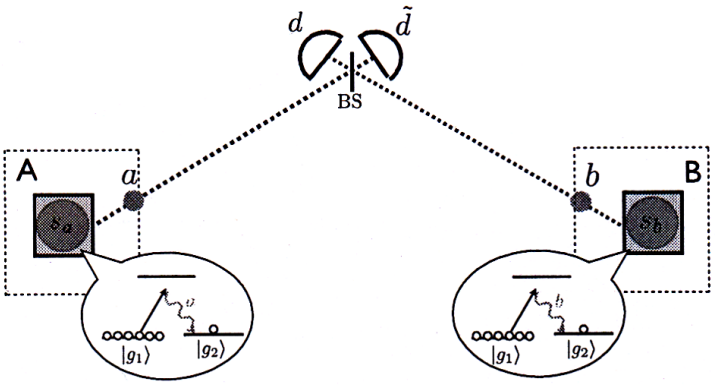

Figure 1.5: Scheme for entanglement creation in elementary links. ([3], fig. 3)

the single photon detection event in d or $\widetilde{d}$ project the two qubits system in the state:

$$\Psi^*_{AB} = \frac{1}{\sqrt{2}} \left(\mid 1_A 0_B \rangle \; + \; e^{i\theta_{AB}} \mid 0_A 1_B \rangle \right) \tag{1.10}$$

where θ_{AB} is a phase factor that depends on the phases of the write pulses and the phase acquired by the Stokes photon during is path to the detectors.
The state (1.10) is entangled. It expresses the fact that, since we detected a Stokes photon, we are sure that one atomic excitation has been created, but it can be either in A or in B. Since there is no way to predict without further measurements which is the excited memory, the system is in a coherent superposition of the two possibilities. In this way the elementary entangled links is created. Its important to highlight that the establishment of such entangled state is heralded, as required for a quantum repeater, by the detection of the stokes photon itself.

Entanglement swapping

Let now consider two adjacent elementary links AB and CD (refer to figure 1.6)= in the entangled states Ψ_{AB} and Ψ_{CD}. The overall function that describes the two link system will be:

$$\Psi_{AB,CD} = \mid \Psi^*_{AB} \Psi^*_{CD} \rangle \tag{1.11}$$

If we now send two read pulses to the memory in B and in C we can retrieve the excitations probabilistically stored in the two ensembles, converting them into two possible anti-Stokes photons. Again, the two photon modes b' and c' are combined on a beam splitter and the measurement of a single photon will project the state of the memories A and D in a entangled state Ψ^*_{AD} [3].
By iterating successive entanglement swapping operations, it is possible to establish entanglement between more and more distant ensembles, up to the distribution of

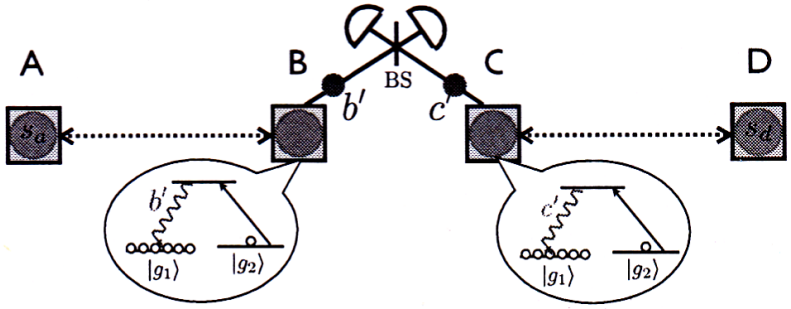

Figure 1.6: Scheme for entanglement swapping. ([3], fig. 4)

the entanglement from A to Z. In order to achieve this goal it is important that the memories are capable to store the excitations for a time at least equal to the total time to perform all the swapping operations.

1.2.5 Quantum frequency conversion

We saw how, with the DLCZ protocol, it is possible to realize a long distance quantum communication architectures based on atomic ensembles and linear optics. In this scheme is necessary to send Stokes and anti-Stokes photons emitted by the atoms, via direct fiber transmission, to the measurement stations to create and swap the entangled states. We already discussed that the optimum wavelength range for fiber transmission is around 1,55 μm, the so-called "telecom C-band", where the light attenuation reaches its minimum at 0.2 dB/km. However, most systems able to serve as quantum memory have atomic transitions in the visible or near infrared range[11]. Here the fiber attenuation is much stronger e.g. 4 dB/km at 780 nm[12]. This optical frequency mismatch can be filled by a quantum frequency down converter device, that shift the frequencies of Stokes and anti-Stokes photons from the visible atomic resonances to the telecom C-band. Note that the need for having an interface from quantum memories to telecom photons is not only needed for the DLCZ scheme, but also for other more efficient quantum repeater protocols [43].
The interest in quantum frequency conversion is not only related to quantum repeaters, but covers a wider range of quantum optics applications. For example an efficient conversion of photons from 1,5 μm and 1,3 μm to 650 nm would enhance

[11] with one exception being Erbium atoms doped into crystals, which absorb light around 1530 nm. A quantum memory has been recently demonstrated in erbium doped solids, albeit with low efficiency [47]

[12] This is the wavelength of Stokes and anti-Stokes photons emitted by an ensemble of rubidium atoms.

significantly the single telecom photon detection, since the silicon based detectors, show a high efficiency peak at this wavelength [48],[49].
Quantum frequency conversion can also be used to interconnect different types of quantum memories or solid state qubits. It is hence a required step towards hybrid quantum networks that combine different kind of atomic systems.
The main requirement for a quantum frequency conversion device is that it preserves the quantum state of the photons. The fidelity of the conversion should be as high as possible. This result is achieved when the quantum coherence of the photons is preserved and when the noise introduced in the conversion is as low as possible.
Several quantum converter schemes have been proposed for different purposes and the majority of them is based on non linear optics effects via three wave mixing in non linear periodically poled waveguides. Up conversion experiments, usually performed via sum frequency generation (SFG), have been done to convert single photons from telecom to visible wavelengths[50],[51]. The vice versa is achieved via difference frequency generation (DFG) and in the next paragraph I will enter in the details of the state of the arte in this field. Finally, techniques based on four wave mixing have also been used, both in photonic crystal [52] fibers and and in cold atomic gases [**?**].

1.3 State of the art on quantum frequency down conversion

Few experiments of quantum frequency down conversion have been carried out so far.

The first successful results have been obtained in two independent works published in 2010 [53],[54],[55]. The experimental setups and the performances are similar for the two. They demonstrated a phase preserving down conversion of weak coherent light, attenuated at the single photon level, from 710 nm to 1310 nm. In these experiments the down conversion of weak coherent pulses (duration of 100 ps FWHM) is realized via difference frequency generation in a periodically poled waveguide fabricated in lithium niobate (PPLN). The authors estimated the conversion efficiencies achieved (in terms of fraction of 710 nm photons that leave the waveguide as 1310 nm) of 2% and 0.35% respectively. A more general total efficiency value, that takes into account all the losses from the waveguide input to the detector, is estimated to be around 0.13 % in the first paper. The limiting factors to this value are more technical then fundamental, e.g. good mode overlap in the waveguide or limited pump power. The coherence preservation of the light during the process is demonstrated via interferometric measurements. The authors identify the main noise source in their setups in the dark counts [54] and in the residual pump light that survives from the filtering at the output of the waveguide and reaches the detection modules [55]. This allows them to reach $SNR \geqslant 1$ in the detection of 1310 nm signal with input average number of photon per pulse < 1 (the exact value is not specified). A third, more recent paper, published in June 2011 [56], showed the down conversion of weak coherent pulses (9 ns FWHM) from 738 nm to 1557 nm, again in a PPLN waveguide, with a conversion efficiency of 73% and total efficiency around 20%. This huge improvement is due to the high efficiency of the waveguide itself and the better mode overlap between pump and signal they could achieve in it. In this experiment the main noise source, as the authors demonstrate with an accurate spectral noise characterization, is the Raman scattering in the waveguide that is caused by the conversion of visible photons toward the telecom C-band via DFG. This difference in the noise source with the previous work is related to the different wavelength range explored. To limit it they used narrow band pass filters (BW = 1 ns). Again, a good SNR is achieved with average input photons per pulse < 1. This experiment is a clear improvement with respect to the previous of 2010, despite no coherence preservation has been demonstrated.

Another successful quantum frequency down conversion experiment has been re-

ported in 2011 [57] (submitted on 9 June and not yet published), again via DFG in a PPLN waveguide. They converted photons from 780 nm to 1522 nm with an efficiency of 62%, measured using with coherent pulses (FWHM 1 ps). The most relevant improvement in this work is the fact that it is the first (and so far unique) down conversion in non-linear crystal performed also in a fully quantum regime, using Fock states (generated via spontaneous down conversion). They started demonstrating that the down conversion preserves the sub-Poissonian photon statistics of number states. Then they used their setup on one half of visible entangled photon pairs and demonstrated that entanglement is not degraded during the process (fidelity measured of 95%)

Finally, an efficient down conversion experiment from 795 nm to 1530 nm with Fock states was reported in September 2010, but using a four wave mixing process in a dense cold atomic cloud [58].

It is important to highlight that, so far, no experiments has been done (with crystals) with light compatible with quantum memories, where you need precise spectral properties and usually much narrower (and hence longer) photons.

The experiment carried out in this thesis is the construction of a quantum frequency down converter for the improvement of a quantum memory realized with cold rubidium atoms (fig. 1.4), actually under development in the QPSA group at ICFO. We also opted for the implementation of the setup via DFG in a PP waveguide.

The main novelty of our work is the compatibility with quantum memories. For that, you need much longer photons and hence we have much more stringent noise requirements than previous experiments. We also investigate the possibility to implement the DFG at the single photon level using a different crystal, the periodically poled potassium titanyl phosphide (PP-KTP) that is in principle more flexible than PPLN in terms of feasible poling period.

All the result we obtained will be presented and discussed in chapter 4.

CHAPTER 2

DIFFERENCE FREQUENCY GENERATION

Non linear optics is the study of the light-matter interaction phenomena whose strength depends non linearly from the intensity of the applied optical field. In this class we include a great variety of effects, e.g. the second and higher order harmonic generation, Raman amplification, self phase modulation etc. Usually, these phenomena are second (or higher) order effects. Their observation requires high optical intensities, of the order of the atomic fields. For this reason, to produce such effects with classical thermal light is almost impossible. Only after the discovery of the laser, non linear optics started to be intensely studied and it became fundamental in optics technology.

Some non linear effects play a key role in quantum information science. We cite, as an example, the generation of entangled photons pairs via Spontaneous Parametric Down Conversion (SPDC).

Our goal is to build a setup to implement the quantum frequency conversion (QFC) of photons from 780 nm to 1550 nm. Ideal QFC should enable wavelength translation of a quantum state of light while preserving its essential quantum characteristics, mainly photon statistics and coherence. It has been demonstrated that this result can be achieved exploiting non linear optics. In particular, we will obtain the conversion via difference frequency generation.

In this chapter I will present briefly the origin of non linear optics phenomena and I will focus the attention on the difference frequency generation. I will derive classically some useful results that we will demonstrate experimentally in chapter 4. Then I will present the quantum features of this process.

2.1 Classical theory of the difference frequency generation

Optics phenomena are based on the light and matter interaction, that is mainly mediated by the effects that the optical electric field $\vec{E}(t)$ induces on the motion of the material electrons. In particular, the displacement from their equilibrium positions causes the creation of electric dipole moments, whose density in the medium is described by the quantity called "dielectric polarization" $\vec{P}(t)$. In linear materials, the relation between $\vec{E}(t)$ and $\vec{P}(t)$ can be expressed as follows[1]:

$$P(t) = \chi^{(1)} \cdot E(t) \tag{2.1}$$

where $\chi^{(1)}$ is called linear dielectric susceptibility and is function of the radiation frequency and several physical parameters of the material. This time-varying polarization acts as source electromagnetic field with the same frequency of the incident light, and it is the responsible of all the linear optics phenomena like, reflection, refraction, linear absorption etc.
Eq. 2.1 can be generalized for the so-called "non linear" materials, expanding the relation as a power series:

$$P(t) = \chi^{(1)} \cdot E(t) + \chi^{(2)} \cdot E^2(t) + \chi^{(3)} \cdot E^3(t) + ... = P^{(1)}(t) + P^{(2)}(t) + P^{(3)}(t) + ... \tag{2.2}$$

where $\chi^{(n)}$, $n > 2$ is the n-th order nonlinear susceptibility and $P^{(n)}$, $n > 2$ is the correspondent n-th order nonlinear polarization induced. From the latter, a great variety of electromagnetic effects can emerge and these are called "non linear optics" phenomena.

2.1.1 Difference frequency generation

Let us consider a non linear material that interacts at the same time with two independent laser beams, with different amplitudes and frequencies. The correspondent incident electric field consists of two distinct components, which we represent in the complex form as:

$$E(t) = E_1 e^{-i\omega_1 t} + E_2 e^{-i\omega_2 t} + c.c. \tag{2.3}$$

[1]We treat from now on $\vec{P}$ and $\vec{E}$ as scalar quantities. Moreover, eq. 2.1 holds only if we suppose an instantaneous and local response of the medium to the electric fields. This ideal situation is that of lossless and dispersionless materials. For our purpose, this approximation level is enough to understand the basic physical principles underlying the non linear optics phenomena.

where $c.c.$ denotes the complex conjugate. We consider now that the material exhibits a second order non linear response characterized by $\chi^{(2)}$. We can calculate $P^{(2)}$ as:

$$P^{(2)}(t) = \chi^{(2)} \cdot E^2(t) = \chi^{(2)} \cdot \left(E_1 e^{-i\omega_1 t} + E_2 e^{-i\omega_2 t} + c.c.\right)^2 \tag{2.4}$$

Developing the parenthesis, we obtain that $P^{(2)}(t)$ consists of a sum of 5 distinct terms: one is constant in time and the others oscillate at $2\omega_1$, $2\omega_2$, $\omega_1+\omega_2$ and $\omega_1-\omega_2$ respectively. Each of these terms is responsible for the generation of electromagnetic radiation at the corespondent frequency. This leads to the non linear phenomena called optical rectification (OR), second harmonic generation (SHG), sum frequency generation (SFG) and difference frequency generation (DFG).
We focus our attention on the DFG.
Let us consider the situation depicted in figure 2.1: Two collinear beams at ω_1 and

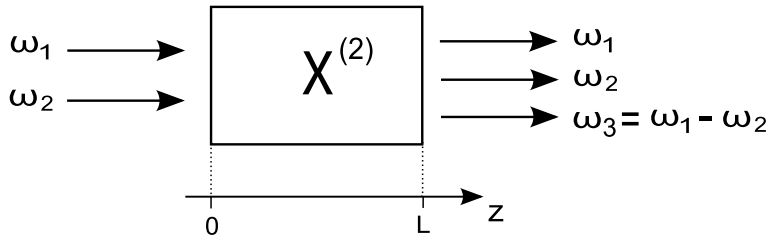

Figure 2.1: Difference frequency generation

ω_2 propagates into a non linear crystal of length L. We want to study the conditions under which the generation of radiation at $\omega_3 = \omega_1 - \omega_2$ is efficient.
The presence of the fields at ω_1 and ω_2 induces in the material the non linear DFG polarization. From the expansion of eq. (2.4) it can be expressed as:

$$P_{\omega_1-\omega_2}(z,t) = 2\chi^{(2)} E_1(z,t) E_2^*(z,t) \; + \; c.c. \tag{2.5}$$

According to the classical electromagnetism theory, we know that the wave equation to study the propagation of the field at ω_3 in the medium is:

$$\frac{\partial^2 E_3(z,t)}{\partial z^2} \; + \; \frac{\epsilon_3}{c^2} \cdot \frac{\partial^2 E_3(z,t)}{\partial t^2} = -\frac{4\pi}{c^2} \cdot \frac{\partial^2 P_{\omega_1-\omega_2}(z,t)}{\partial t^2} \tag{2.6}$$

where ϵ_3 is the dielectric constant of the material at ω_3. We notice that the inhomogeneous polarization term plays the role of the field source.
We are interested in oscillatory solutions of the form:

$$E_3(z,t) = A_3(z) \cdot e^{i(k_3 z - \omega_3 t)} + cc \tag{2.7}$$

$k_3 = \frac{n_3 \omega_3}{c}$ is the modulus of the wave vector and $n_3 = \sqrt{\epsilon_3}$ is the refractive index of the material experienced by the field at ω_3.

A solution of the form (2.7) represents an electromagnetic wave that propagates in the z direction and whose amplitude depends on this coordinate. In the following sections we will show how to calculate $A_3(z)$ under different assumptions.

2.1.2 Weak interaction approximation

We start with the calculation of $A_3(z)$ in the approximation of weak interaction. It is based on two assumptions:

1. We consider that the fields of the incident waves at ω_1 and ω_2 have the same form of eq. (2.7). We also suppose that the generated ω_3 field is weak. In this way we can neglect the non linear polarization that its presence in the medium induces. It could generate other nonlinear effects ie. the SFG between $\omega_2 + \omega_3 = \omega_1$ or the DFG between $\omega_1 - \omega_3 = \omega_2$. In this case the propagation of the three beams would be strongly coupled with each others. According with this approximation, we can treat the amplitudes A_1 and A_2 as constants.

2. We work in the so called "slow varying amplitude approximation" for the $E_3(z,t)$ field. It is given by in the mathematical condition:

$$\left|\frac{d^2A_3}{dz^2}\right| << \left|k_3\frac{dA_3}{dz}\right| \tag{2.8}$$

   Its physical meaning is that A_3 varies very few over one optical wavelength.

We substitute (2.5) in (2.6) and we use the (2.7) for the electric fields. After some algebra and under the aforementioned approximations, we obtain a differential equation for the amplitude $A_3(z)$:

$$\frac{dA_3(z)}{dz} = i\frac{4\pi\chi^{(2)}k_3}{c^2}A_1A_2^*e^{i(k_1-k_2-k_3)z} \tag{2.9}$$

For simplicity, we call G the quantity $\frac{4\pi\chi^{(2)}k_3}{c^2}$ and we define the wave vector mismatch as:

$$\Delta k = k_1 - k_2 - k_3. \tag{2.10}$$

Equation (2.9) then becomes:

$$\frac{dA_3(z)}{dz} = iGA_1A_2^*e^{i(\Delta k)z} \tag{2.11}$$

The solution $A_3(z)$ can be immediately calculated integrating the right-hand side of eq. 2.11 from 0 to L. Remembering the initial condition $A_3(0) = 0$, we can write:

$$A_3(L) = iGA_1A_2^*\int_0^L e^{i\Delta kz}dz = iGA_1A_2^*\left(\frac{e^{i\Delta kL}-1}{i\Delta k}\right) \tag{2.12}$$

We remind that the intensity of an electromagnetic wave of amplitude A is defied as:

$$I(x,t) = \frac{nc}{2\pi} |A(x,t)|^2 \tag{2.13}$$

We can therefore calculate the intensity of the generated light at the output of the crystal as:

$$I_3(L) = G^2 \left(\frac{c}{2\pi}\right)^2 (n_1 n_2) I_1 I_2 \left|\frac{e^{i\Delta kL} - 1}{i\Delta k}\right|^2 \tag{2.14}$$

The squared modulus in eq. (2.14) can be rearranged in a more convenient way as follows:

$$\left|\frac{e^{i\Delta kL} - 1}{i\Delta k}\right|^2 = L^2 sinc^2\left(\frac{\Delta kL}{2}\right) \tag{2.15}$$

Finally we obtain the result for the generated intensity radiation at ω_3 at the crystal output:

$$I_3(L) = \gamma I_1 I_2 L^2 sinc^2\left(\frac{\Delta kL}{2}\right) \tag{2.16}$$

where all the physical and numerical constants are included in the proportionality factor γ:

$$\gamma = \frac{265\pi^5 \chi^2_{(2)}}{n_1 n_2 n_3 \lambda_3^2 c} \tag{2.17}$$

We can observe that the intensity of the generated light is directly proportional to the intensities of the incident beams.

2.1.3 Phase matching

Let us consider now the special situation in which:

$$\Delta k = 0 \tag{2.18}$$

In this case we can see that the intensity of the generated light simply increase quadratically with the length of the crystal. The condition 2.18 is known as perfect phase matching. When it is satisfied, the generated radiation at ω_3 maintains a precise fixed phase relation with $P_{\omega_1-\omega_2}(t)$. In this way, the field emitted by each atomic dipole adds coherently in the forward direction. As consequence of this, the intensity I_3 constantly during the propagation in the crystal.
On the other hand, the generated intensity fasten decreases when Δk grows. This is entirely caused by the $sinc^2$ factor, whose shape is visible in fig. 2.2. Moreover, we can rearrange the (2.16) to study the case of $\Delta k \neq 0$. Expanding the $sinc^2$ and simplifying the L^2 factor, we find the intensity behavior with respect to L:

$$I_3(L) = \frac{\gamma I_1 I_2}{\Delta k} \sin^2\left(\frac{\Delta kL}{2}\right) \tag{2.19}$$

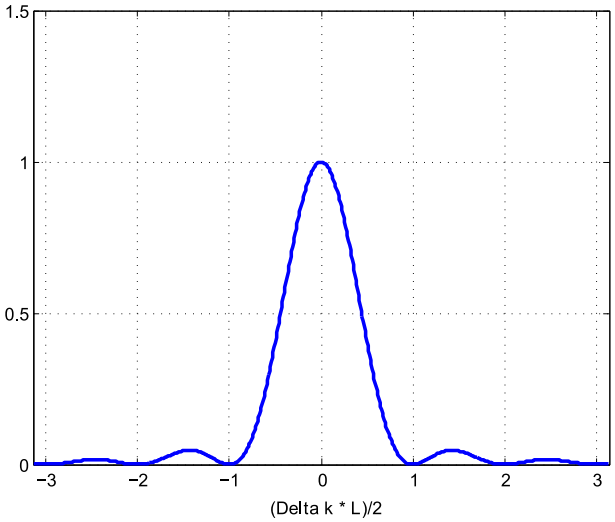

Figure 2.2: Fractional variation of the generated intensity intensity as function of the wave vector mismatch

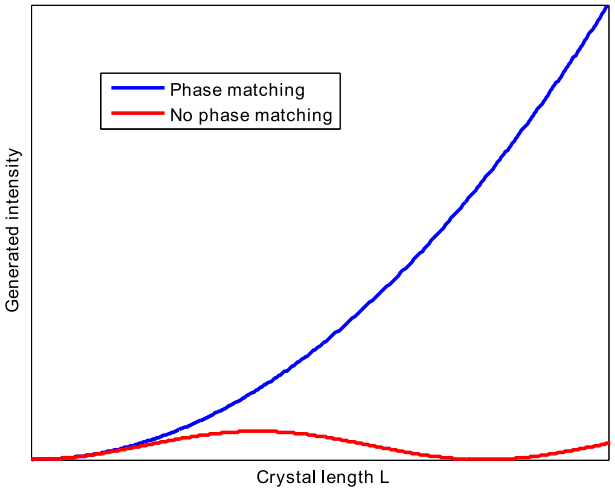

Figure 2.3: Comparison between the phase matched and non phase matched situations

that is sinusoidal in L. Its maximum is inversely proportional to Δk. In figure 2.3 we compare the phase matched and the non phase matched situations. It is evident that when the phase matching condition is fulfilled, the DFG process is much more efficient.

The phase matching condition (2.18) for collinear beams is equivalent to:

$$n_1\omega_1 = n_2\omega_2 + n_3\omega_3 \tag{2.20}$$

Let us remind that:

$$\omega_1 = \omega_2 + \omega_3 \tag{2.21}$$

The refractive index is usually a growing function of frequency (normal dispersion) for lossless materials. We suppose that $\omega_1 > \omega_2 > \omega_3$ and so $n_1 > n_2 > n_3$. The equation (2.20), using the (2.21), can be manipulated and rearranged in the equivalent form:

$$n_1 - n_2 = (n_3 - n_2)\frac{\omega_1}{\omega_3} \tag{2.22}$$

Since the left hand side of eq. 2.22 is positive and the right hand side is negative, this equality is impossible. The eq. 2.20 and 2.21 are not compatible and the phase matching cannot be achieved with collinear beams and normal dispersion.
A possible solution to overcome this problems could be to exploit the anomalous dispersion of some materials. In this case the refractive index drops at higher ω. This occurs eg. in a frequency range close to the resonant absorption of the materials. However, the most common method to phase match a non linear process is to make use of the birefringence. This phenomenon consists in the dependence of n experienced by a wave in a medium with respect to its polarization direction. The (2.20) can be achieved in birefringent crystals fixing very precisely the geometry of the experiment.

2.1.4 Quasi phase matching

There are several experimental conditions in which the phase matching cannot be achieved via birefringence. This can happen because some non linear materials don't exhibit this feature or their birefringence is not sufficient for the wavelength range needed. In other cases, to exploit the non linearity of the medium, it is necessary that the input beams have their polarizations oriented along the same direction. In all these situations the optimization of the non linear process must be implemented with other strategies.
There is a technique known as quasi phase matching that can be used when the normal phase matching cannot be realized. The basic idea is to use a non linear material fabricated in such a way that its ferroelectric domains are periodically alternated, with period Λ (2.4). This leads to a periodical inversion of the sign of $\chi^{(2)}$. Such a material is said to be periodically poled (PP) with poling length Λ.
Let us imagine that Λ is chosen such that it covers exactly one period of the oscillations of $I_3(z)$. From the (2.19) we can calculate

$$\Lambda = \frac{2\pi}{\Delta k} \tag{2.23}$$

The variation of the sign of $\chi^{(2)}$ occurs every $\Lambda/2$. As consequence, each time that the field intensity of the generated wave is about to decrease, we have a domain inversion. This inverts the sign of the interaction and I_3 begins to increase again. In this way, I_3

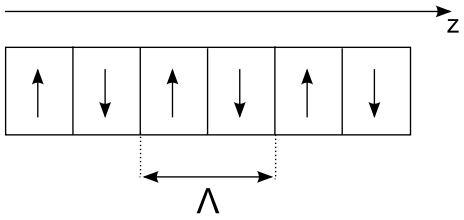

Figure 2.4: Periodically poled material. The ferroelectric domains are periodically alternated.

grows monotonically all over the crystal length. Although the quadratical growth of the phase matched condition is much faster, it represents a good solution to have an efficient DFG process. This effect is represented in figure 2.5. This phenomenological

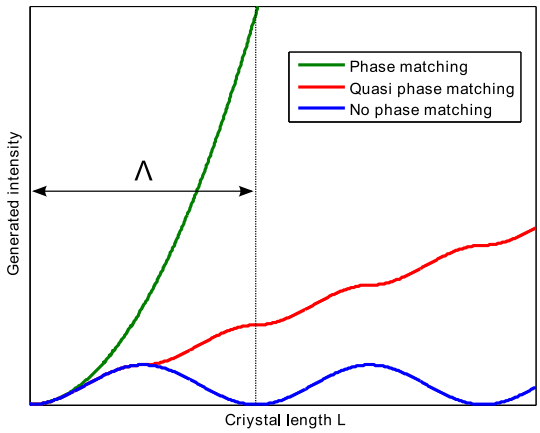

Figure 2.5: Quasi phase matching DFG generation.

description can also be derived mathematically, substituting

$$\chi^{(2)}(z) = \chi^{(2)} \cdot sign\left[cos\left(\frac{2\pi z}{\Lambda}\right)\right] \tag{2.24}$$

in the non linear polarization term of the equation (2.6). An equation formally equivalent to 2.11 can be derived for the amplitude field variation in the z direction. Under the assumption that the main contribution of (2.24) is provided by its fundamental Fourier component

$$\chi^{(2)}(z) = \chi^{(2)} \cdot \frac{2}{\pi} \cdot e^{ik_m z} \tag{2.25}$$

and substituting it in the (2.6), we obtain the intensity of the ω_3 radiation:

$$I_3(L) = \gamma_q I_1 I_2 L^2 sinc^2\left(\frac{\Delta k_q L}{2}\right) \tag{2.26}$$

Here γ_q contains the same constants of (2.17), except the replacement of $\chi^{(2)}$ with $\chi_q^{(2)} = \chi^{(2)} \cdot \frac{2}{\pi}$. The definition of the wave vector mismatch in quasi phase matching configuration is:

$$\Delta k_q = k_1 - k_2 - k_3 - k_m \tag{2.27}$$

where

$$k_m = \frac{2\pi}{\Lambda} \tag{2.28}$$

All the considerations we did for the phase matching regime continue to hold for the quasi-phase matching. Hence, the best efficiency condition is still achieved when:

$$\Delta k_q = 0 \tag{2.29}$$

that implies

$$\Lambda = \frac{2\pi}{\Delta k} \tag{2.30}$$

that is the quasi phase matching condition we derived in (2.23) with phenomenological arguments.

With the quasi phase matching configuration we don't need anymore to work with the refractive indexes because we introduced a new degree of freedom: the poling length Λ. We can achieve the maximum efficiency simply adjusting this parameter. The poling lengths commonly required for this kind of experiments are in the order of few tens of µm. The best technique to tune Λ in this length scale is to exploit the dependence of the geometric dimensions of the crystal from the temperature. We can act on this parameter to change Δk_q and to reach the quasi phase matching configuration.

2.1.5 Three wave mixing

We will analyze now the more general case, relaxing the weak interaction approximation introduced in § 2.1.2. We continue to operate in the slow varying regime (expressed by the eq. 2.8) but we will take into account the effects that the field at ω_3 induces in the polarization of the non linear medium.

Let us consider the total electric field inside the material as:

$$E(z,t) = A_1(z) \cdot e^{i(k_1 z - \omega_1 t)} + A_2(z) \cdot e^{i(k_2 z - \omega_2 t)} + A_3(z) \cdot e^{i(k_3 z - \omega_3 t)} + c.\,c. \tag{2.31}$$

and remember that the angular frequencies satisfy the condition:

$$\omega_3 = \omega_1 - \omega_2 \tag{2.32}$$

According to what we discussed in the beginning of § 2.1.1, the non linear time varying polarization induced in the material will contain the following terms:

$$\begin{aligned} P_{\omega_1}(z,t) &= 2\chi^{(2)} E_2(z,t) E_3(z,t) \; + \; c.c. \\ P_{\omega_2}(z,t) &= 2\chi^{(2)} E_1(z,t) E_3^*(z,t) \; + \; c.c. \\ P_{\omega_3}(z,t) &= 2\chi^{(2)} E_1(z,t) E_2^*(z,t) \; + \; c.c. \end{aligned} \tag{2.33}$$

Each of them will behave as source of electromagnetic field at the correspondent frequency and so, the propagation of each component will be mutually influenced by the others. This phenomenon is known as "three wave mixing".
Following the same strategy used to describe the propagation of the single field $E_3(z,t)$, we can write a set of three coupled equations that describe the variation of A_1, A_2 and A_3:

$$\begin{aligned}\frac{dA_1(z)}{dz} &= iG_1A_2A_3e^{-i(\Delta k)z}\\ \frac{dA_2(z)}{dz} &= iG_2A_1A_3^*e^{i(\Delta k)z}\\ \frac{dA_3(z)}{dz} &= iG_3A_1A_2^*e^{i(\Delta k)z}\end{aligned} \tag{2.34}$$

where:

$$G_i = \frac{4\pi\chi^{(2)}k_i}{c^2} \tag{2.35}$$

and again the wave vector mismatch is:

$$\Delta k = k_1 - k_2 - k_3. \tag{2.36}$$

Despite the system (2.34) can be solved analytically, it is more interesting to study it under certain approximations.

2.1.6 Strong pump approximation

Let us assume that one of the three fields is much stronger than the others. In this way it will be slightly influenced by the interaction and so we can consider constant its amplitude. This allows to simplify the system notably.
In our experiment we want to convert light from 780 nm to 1550 nm via DFG according to the relation $\omega_{1550} = \omega_{780} - \omega_{1570}$. The pump will be at 1570 nm and so in this treatment we consider constant the amplitude A_2.
Let consider also that we operate in phase matching condition, so $\Delta k = 0$.
Under these approximations the system 2.34 becomes:

$$\frac{dA_1(z)}{dz} = iG_1A_2 \cdot A_3 \tag{2.37}$$

$$\frac{dA_3(z)}{dz} = iG_3A_2^* \cdot A_1 \tag{2.38}$$

and gives the solution that we are interested in for the initial conditions $A_3(0) = 0$ and $A_1(0) = \widetilde{A}_1$.
Once the amplitudes $A_1(z)$ and $A_3(z)$ are known, it is possible to obtain the behavior of the field intensities and relate them to the number of photons per unit time that

enter and leave the material. The analytical solution of these coupled-mode equation allows to obtain the dependence for $A_3(z)$:

$$A_3(z) = i\sqrt{\frac{n_1\omega_3}{n_3\omega_1}}\frac{|A_2|}{A_2^*}\widetilde{A}_1 \sin(\Gamma z) \tag{2.39}$$

where $\Gamma = \sqrt{G_1 G_3}$.
Remember that, according with the relation (2.13), the squared modulus of $A_3(z)$ is proportional to the beam intensity. The latter is proportional to the number N of photons per unit time and unit area[2]:

$$I = N\hbar\omega \tag{2.40}$$

If we consider that the generation takes place only in the beams overlap section, we can express the number of photons per unit time (photon rate) at the crystal output as:

$$R_3(L) = R_1(0)\sin^2(\sqrt{\eta_{norm}P_p}L) \tag{2.41}$$

where η_{norm} is a constant that contains all the physical parameter of the process.
We see that even in the phase matching condition, the dependence from L for the generation is sinusoidal and not parabolic, as we obtained in the weak interaction regime. We can understand this behavior considering that, when the generated light reaches its maximum, the predominant interaction in the material will be the generation of light at ω_1 via SFG between the pump and the light at ω_3. This leads to a depletion of the generated beam, until the DFG process will be dominant again, and so on.
We define the conversion efficiency η_{conv} as:

$$\eta_{conv} = \frac{R_3(L)}{R_1(0)} = \sin^2(\sqrt{\eta_{norm}P_p}L) \tag{2.42}$$

and in figure 2.6 we can se its behavior with respect to the pump power P_p, for a fixed value of L. We can se that for low values of P_p the growth is linear. This is consistent with the weak interaction approximation, because with low values of the pump, also the generated light is very weak and the variation of R_1 is negligible.
We can obtain the expression for the linear region with a first order approximation:

$$\eta_{conv\,P_p\to 0} \approx \left.\frac{\partial\eta_{conv}}{\partial P_p}\right|_{P_p=0} P_p = \eta_{norm}L^2P_p \tag{2.43}$$

When the pump grows, the conversion efficiency starts to saturate up to the value P_{max}, when a total conversion of the beam at ω_1 is achieved. We can calculate P_{max}

[2]This expression will explained more in detail in § 2.2.

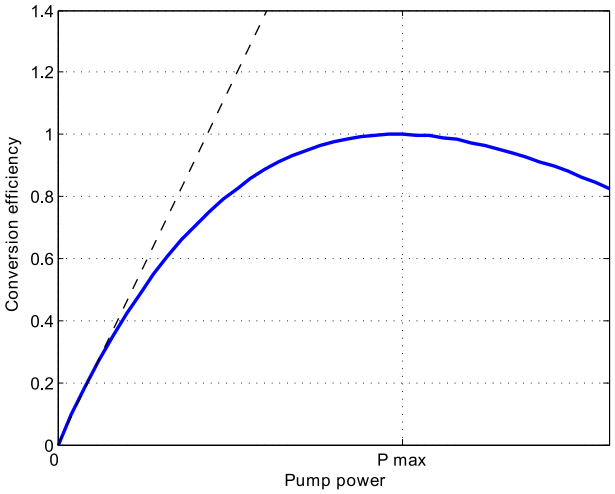

Figure 2.6: Conversion efficiency as function of pump power.

considering that η_{conv} reaches its first maximum when the argument of the sinus is equal to $\pi/2$. From this we obtain:

$$P_{max} = \frac{\pi^2}{4\eta_{norm}L^2} \tag{2.44}$$

As we observed in the case of weak interaction regime, no substantial differences arise when considering a quasi-phase matching configuration instead of a perfectly phase matching. Again the optimum efficiency condition is represented by the 2.29, achievable tuning the poling length Λ. If the wave vector mismatch were not zero, the intensity of the generated beam would drop according to the $sinc^2$ factor depicted in figure 2.2.

2.2 Quantum properties of the DFG

The first evidences of the quantum nature of light are dated back to Plank's and Einstein's studies in the early years of 1900. They discovered that some well known physical phenomena, like the spectral energy distribution radiated by a black body and the photoelectric effect, could be explained only accepting the hypothesis that an electromagnetic wave exchanges energy with other systems by integer multiples of a fundamental quantity, whose value is proportional to the frequency of the wave itself. This suggested that an electromagnetic wave can be seen as a stream of quanta, called photons, whose creation and destruction is responsible of changes in the field energy. Each of them carries an amount of energy equals to $h\nu$, where ν is the wave frequency, and h is called "Plank's constant". It is remarkable that this quantity is indeed very small compared to the energy scale that involves macroscopic phenomena[3], but is comparable to that of atomic world.
The concept of photon is rigorously formalized by the "quantum optics theory", essentially born with the quantum description of optical coherence and of the states of the radiation field, developed by Glauber in 1963. The quantum properties of light that emerge from this description are extensively exploited in experiments of quantum information, as discussed in § 1.2.
In this paragraph I will show that the classical theory of DFG presented so far is consistent with a corpuscular description of the phenomenon. I will then introduce briefly some basic quantum optics tools that are useful to understand the features of a quantum frequency conversion and what the simulated quantum regime is.

2.2.1 Particle picture of classical DFG

Let us consider a monochromatic electromagnetic wave of angular frequency ω. Its intensity I expresses the quantity of energy that flows per unit time and area with the wave. From the above mentioned definition of photon, we can determine the number of photons per unit time and area N associated, simply as:

$$N = \frac{I}{\hbar\omega} \tag{2.45}$$

We can calculate the intensity spatial variation as:

$$\frac{dI_i}{dz} = \frac{n_i c}{2\pi}\left(\frac{d|A_i|^2}{dz}\right) = \frac{n_i c}{2\pi}\left(A_i^*\frac{dA_i}{dz} + A_i\frac{dA_i^*}{dz}\right) \tag{2.46}$$

[3]for example, for visible light (e.g. $\lambda = 780\,nm$), this energy quantum corresponds to $1.6\,eV = 2.5\times10^{-19}J$.

Through the use of this result and the equations set 2.34, we find that the spatial variation of the intensity of the beams involved in the three wave mixing is:

$$\frac{dI_1}{dz} = 4\chi^{(2)}\omega_1 Im\left(A_1 A_2^* A_3^* e^{-i\Delta kz}\right) \tag{2.47}$$

$$\frac{dI_2}{dz} = -4\chi^{(2)}\omega_2 Im\left(A_1 A_2^* A_3^* e^{-i\Delta kz}\right) \tag{2.48}$$

$$\frac{dI_3}{dz} = -4\chi^{(2)}\omega_3 Im\left(A_1 A_2^* A_3^* e^{-i\Delta kz}\right) \tag{2.49}$$

Although these equations should be solved to find the explicit dependence of the intensities from z, they can be used to obtain the following equalities chain, know also as Manley Rowe relations:

$$\frac{d}{dz}\left(\frac{I_1}{\omega_1}\right) = -\frac{d}{dz}\left(\frac{I_2}{\omega_2}\right) = -\frac{d}{dz}\left(\frac{I_3}{\omega_3}\right) \tag{2.50}$$

Using the formula 2.45 we can finally write:

$$\frac{dN_1}{dz} = -\frac{dN_2}{dz} = -\frac{dN_3}{dz} \tag{2.51}$$

The equalities 2.51 express that the rate of change in the photons number for the beam at ω_1 is opposite to that of the beams at ω_2 and ω_3[4]. Equivalently we can state that, per each photon at ω_1 that is annihilated during the process, one photon at ω_2 and one at ω_3 are created, and vice versa.

This result can be understood intuitively by means of the virtual energy level scheme of a three wave mixing process, visible in figure 2.7. We thus see that the classical

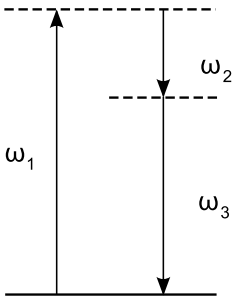

Figure 2.7: Virtual energy level scheme of the three wave mixing process.

wave description of the DFG is consistent with a particle one. During the process, the presence of ω_2 photons in the material stimulates the annihilation of a photon at ω_1 in favor of the creation of a photon at $\omega_3 = \omega_1 - \omega_2$ and of another photon at ω_2.

[4]Note that the direction of the energy flow depends on the relative phases of the three interacting fields.

2.2.2 Introduction to quantum optics

We will see now in a simple and intuitive way some basic concepts of quantum optics that are useful to understand the description of the DFG process in the context of this theory.

We underlined in the introduction of this paragraph that the first evidence of the quantum nature of optical phenomena is related to the quantization of the light energy. The study of the latter is thus the most natural starting point to derive the quantum optics theory.

Let us analyze the simplest case of a single mode electromagnetic wave of given frequency and fixed polarization direction that propagates in vacuum along the z axis. According to the classical theory, the electromagnetic energy associated to such a wave in a region of volume V is calculated as:

$$U_{EM} = \frac{V}{2}\left(\epsilon_0|\vec{E}|^2 + \frac{1}{\mu_0}|\vec{B}|^2\right) \tag{2.52}$$

where ϵ_0 and μ_0 are the electric and magnetic permittivity of vacuum respectively. It is well known that an electromagnetic field can be equivalently described either by the fields $\vec{E}$ and $\vec{B}$ or by $\vec{A}$ and ϕ, called vector and scalar potentials of the electromagnetic field[5]. Using the so-called "Coulomb gauge" ($\nabla \cdot \vec{A} = 0$), the wave vector that describes our problem is:

$$\vec{A}(z,t) = \left(Ae^{i(kz-\omega t)} + A^* e^{-i(kz-\omega t)}\right)\vec{e} \tag{2.53}$$

where $\vec{e}$ is the unit vector that contains the polarization direction of the wave. In absence of free charges and currents, the vector potential $\vec{A}$ is related to the electric and magnetic fields according to the relations:

$$\vec{E} = -\frac{\partial \vec{A}}{\partial t} \quad \vec{B} = \nabla \times \vec{A} \tag{2.54}$$

We can thus express these quantities as follows:

$$\vec{E}(z,t) = i\omega\left(Ae^{i(kz-\omega t)} + A^* e^{-i(kz-\omega t)}\right)\vec{e} \tag{2.55}$$

$$\vec{B}(z,t) = ik\left(Ae^{i(kz-\omega t)} + A^* e^{-i(kz-\omega t)}\right)\vec{z} \times \vec{e} \tag{2.56}$$

where $\vec{z}$ is the unit vector related to the z axis.

Substituting the 2.55 and 2.56 in the 2.52, we can express the electromagnetic energy as function of the vector potential amplitude:

$$U_{EM} = \epsilon_0 V\omega^2\left(AA^* + A^*A\right) \tag{2.57}$$

[5]Here we introduce a change in the notation. From now on the capital letter "A" will denote the amplitude of the the vector potential and we will refer to the amplitude of the electric field with "E".

The expression 2.57 is very interesting because it is formally identical to that of the Hamiltonian operator of the quantum harmonic oscillator:

$$\hat{H}_{HO} = \frac{1}{2}\hbar\omega(\hat{a}\hat{a}^\dagger + \hat{a}^\dagger\hat{a}) \tag{2.58}$$

It is possible to write the equivalent quantum Hamiltonian associated to the electromagnetic mode in the given volume that we are considering, with the usual method that consists in substituting the classical quantities with operators:

$$\hat{H}_{EM} = \epsilon_0 V\omega^2 \left(\hat{A}\hat{A}^* + \hat{A}^*\hat{A}\right) \tag{2.59}$$

and replace the operators associated to the amplitude of the vector potential $\hat{A}$ and $\hat{A}^*$ with the annihilation $\hat{a}$ and creation $\hat{a}^\dagger$ operators as follows:

$$\hat{A} \to \sqrt{\frac{\hbar}{2\epsilon_0 V\omega}}\hat{a} \tag{2.60}$$

$$\hat{A}^* \to \sqrt{\frac{\hbar}{2\epsilon_0 V\omega}}\hat{a}^\dagger \tag{2.61}$$

to obtain;

$$\hat{H}_{EM} = \frac{1}{2}\hbar\omega(\hat{a}\hat{a}^\dagger + \hat{a}^\dagger\hat{a}) \tag{2.62}$$

We can thus extend to our electromagnetic wave all the results that arise from the theory of the quantum mechanical harmonic oscillator. We will focus the attention on this aspect in § 2.2.3

From the substitution of eq. 2.60 and eq. 2.61 in the expressions 2.55 and 2.56, we can obtain the quantum mechanical operators associated to the electric and magnetic fields of a single mode electromagnetic wave of fixed frequency and polarization direction, confined in a volume V:

$$\hat{\vec{E}} = \sqrt{\frac{\hbar\omega}{2\epsilon_0 V}}\left(\hat{a}e^{-i\Gamma} + \hat{a}^\dagger e^{i\Gamma}\right)\vec{e} \tag{2.63}$$

$$\hat{\vec{B}} = \sqrt{\frac{\hbar}{2\epsilon_0\omega V}}\left(\hat{a}e^{-i\Gamma} + \hat{a}^\dagger e^{i\Gamma}\right)\vec{z}\times\vec{e} \tag{2.64}$$

where Γ is a phase angle defined as $\Gamma = \omega t - kz - \pi/2$.

It is possible to demonstrate that these two operators are Hermitian, despite $\hat{a}$ and $\hat{a}^\dagger$ are not, and in fact they correspond to physical observable quantities.

2.2.3 Fock and coherent states

So far we saw how it is possible to apply the formalism of quantum mechanics to obtain an expression for the operators associated to the electric and magnetic field of a single mode electromagnetic wave. We will see now some properties of two particular quantum states of light: the so-called “Fock” and “coherent” states.

Fock states

Let us consider the Hamiltonian operator $\hat{H}_{EM}$ expressed by the 2.59. Using the commutation relation between the creation and annihilation operators[6], it is possible to rewrite it in a simpler form:

$$\hat{H}_{EM} = \hbar\omega \left(\hat{a}^\dagger \hat{a} + \frac{1}{2}\right) \tag{2.65}$$

The Fock states are defined as the eigenstates of this Hamiltonian. From the theory of the quantum harmonic oscillator, we know that such states are described by a quantum number n that can assume only integer non negative values. We denote them with the symbol $\mid n\rangle$, and they satisfy the equation:

$$\hat{H}_{EM} \mid n\rangle = \varepsilon_n \mid n\rangle \tag{2.66}$$

A remarkable property of this states is that they form a complete set and any other state can be expressed as linear combination of them.
The energy eigenvalues are:

$$\varepsilon_n = \hbar\omega \left(n + \frac{1}{2}\right) \quad n = 0, 1, 2, ... \tag{2.67}$$

We can observe that the energy levels of the Fock states are equally spaced of a quantity equals to $\hbar\omega$. For this reason, the number n can be regarded either as the level of the single mode electromagnetic excitation or, equivalently, as the number of photons contained in it.
The ground state $\mid 0\rangle$ is also called "vacuum" state and it is remarkable that it corresponds to a non zero energy value.
Comparing the eq. 2.67 with the eq. 2.65, we can define the number operator:

$$\hat{n} = \hat{a}^\dagger \hat{a} \tag{2.68}$$

that commutes with $\hat{H}_{EM}$. The Fock states $\mid n\rangle$ are also eigenstates of $\hat{n}$ with correspondent eigenvalues n. This means that there is no uncertainty in the number of photons of such a state and for this reason they are also called "number states". On the other hands, it is possible to demonstrate that the phase associated to the these states is totally undetermined. As consequence, the Fock states represent an electromagnetic field that oscillates with a well defined amplitude and frequency but a completely random phase and this differs significantly from a classical electromagnetic wave. The Fock states must be regarded as pure quantum states, with no classical counterpart.

[6] According with the usual definition of these operators used in the quantum harmonic oscillator theory, $[\hat{a}, \hat{a}^\dagger] = \hat{a}\hat{a}^\dagger - \hat{a}^\dagger\hat{a} = 1$.

Coherent states

We will consider now some properties of the single mode states that most approach the behavior of a classical single mode electromagnetic wave. They are called "coherent" states, are denoted as $\mid \alpha\rangle$, and they can be expressed as a linear combination of the Fock states as follows:

$$\mid \alpha\rangle = e^{-\frac{1}{2}|\alpha|^2} \sum_{n=0}^{+\infty} \frac{\alpha^n}{(n!)^{1/2}} \mid n\rangle \tag{2.69}$$

where α is a generic complex parameter associated to a particular state.
If we evaluate the expectation value of the number operator n defined with the 2.68 for these states we obtain:

$$\langle n\rangle = \langle \alpha \mid \hat{n} \mid \alpha\rangle = |\alpha|^2 \tag{2.70}$$

This quantity expresses the average number of photons that are contained in the particular coherent state. However it is not an eigenstate of $\hat{n}$ and thus uncertainty associated to the number of photons related to the state $\mid \alpha\rangle$ is different from zero and it can be calculated as follows:

$$\Delta n = \sqrt{\langle n^2\rangle - \langle n\rangle^2} = |\alpha| = \sqrt{\langle n\rangle} \tag{2.71}$$

The probability to find exactly n photons in a coherent state characterized by an average number of photon $\bar{n}$ can be calculated as follows:

$$P(\bar{n}, n) = |\langle n \mid \alpha\rangle|^2 e^{-\bar{n}} \frac{\bar{n}^n}{n!} \tag{2.72}$$

and thus it follows a Poissonian distribution.
For these states it is possible to demonstrate that the uncertainties related to the phase and amplitude of the electric field associated are equal, and their product is always the minimum possible. In addition, the fractional uncertainty related to this quantities diminishes with increasing the value of $|\alpha|$. Thus, as the average photon number grows, the coherent state becomes more and more similar to an electromagnetic wave of stable amplitude frequency and phase and, in the classical limit of very high $\bar{n}$, it tends to a classical solution of maxwell's equations. For this reason, a monochromatic light pulse generated by a laser operating well above threshold can be described with a good approximation by a coherent state.

2.2.4 Quantum description of DFG

Let us consider now the non linear three waves mixing process that we described classically in § 2.1.5. We will study now the problem from a quantum point of view,

considering that the state of the light before and after the non linear interaction is a superposition of three different single mode states, each of them at the correspondent angular frequency, such that:

$$\omega_3 = \omega_1 - \omega_2 \tag{2.73}$$

The amplitude of the electric fields of the waves involved are represented by the operators:

$$\hat{E}_j = \sqrt{\frac{\hbar\omega_j}{2\epsilon_0 V}} \left(\hat{a}_j e^{-i\Gamma_j} + \hat{a}_j^\dagger e^{i\Gamma_j}\right) \tag{2.74}$$

Each of them is characterized by the correspondent annihilation and creation operators $\hat{a}_j$ and $\hat{a}_j^\dagger$.

If we consider that the light at ω_2 is much stronger than the others, and so again we work in the strong pump approximation, the interaction inside the non linear medium is described by the following Hamiltonian:

$$\hat{H} = i\hbar(\xi^* \hat{a}_3^\dagger \hat{a}_1 + \xi \hat{a}_3 \hat{a}_1^\dagger) \tag{2.75}$$

where ξ is a coupling constant that contains the non linearity of the material and it is proportional to the complex amplitude of the pump light.

This allows to calculate the time evolution of the operators related to the interacting waves. In particular, the results for the destruction operators of the beam at ω_3 and ω_1 at the output of the crystal are:

$$\hat{a}_{1,out}(t) = \hat{a}_1(\tau) = \cos(|\xi|\tau)\hat{a}_1 - e^{i\phi}\sin(|\xi|\tau)\hat{a}_3 \tag{2.76}$$

$$\hat{a}_{3,out}(t) = \hat{a}_3(\tau) = e^{i\phi}\sin(|\xi|\tau)\hat{a}_1 + \cos(|\xi|\tau)\hat{a}_3 \tag{2.77}$$

where τ is the traveling time of the light through the non linear medium and ϕ is the phase of the pump light. The product $|\xi|\tau$ can be adjusted acting on the pump power and the crystal length. In the special case where:

$$|\xi|\tau = \frac{\pi}{2} \tag{2.78}$$

we obtain that $\hat{a}_3(\tau) = e^{i\phi}\hat{a}_1$ and $\hat{a}_1(\tau) = -e^{i\phi}\hat{a}_3$. It is possible to demonstrate that this transformation corresponds to the phase preserving conversion of the state in the mode at ω_1 to the state of ω_3 and vice versa, with 100%. The eq. 2.78 is equivalent to the classical total conversion condition expressed by the eq. 2.44. This process thus proves to be very interesting to perform our quantum frequency conversion experiment.

2.2.5 Simulated quantum regime

As we explained in chapter 1, the aim of our experiment is to build a setup that could be used to convert the quantum states of Stokes and anti-Stokes photons emitted by the cold rubidium atomic ensemble. The conversion is said to be in the "fully" quantum regime and it should maintain unchanged the quantum state of the input light, in terms of coherence properties and photon statistics. The quantity that describes the quantum state preservation is the so-called "fidelity" F of the process which describes the overlap between input and output states:

$$F = Tr\sqrt{\sqrt{\rho}\,\rho'\sqrt{\rho}} \tag{2.79}$$

where ρ and ρ' are the density matrices that describe the input and the output states of the device. A perfect conversion, in which the input and the output states perfectly coincide, has $F = 1$.

In order to obtain a high fidelity quantum frequency conversion, the process should preserve the quantum coherence of the input state and be noise free. However, some level of noise can be tolerated to stay in the quantum regime. It has been demonstrated that for 1 qubit input and unit efficiency process, the threshold fidelity to still be in the quantum regime is F=2/3. To operate with single photons is thus necessary to suppress enough the noise and this operation can be carried out by the characterization of the setup in the "simulated" quantum regime. Here, the single photon input states are replaced by monochromatic coherent laser pulses strongly attenuated, that are well described by coherent states $\mid \alpha\rangle$ containing an average number of photons $\bar{n}$. The setup reaches the fidelity threshold to work as quantum device when the signal to noise ratio (SNR) in the detection of the converted pulses is above 1, using input states with $\bar{n} < 1$. In this regime it is possibile to act on the noise suppression until this threshold is reached.

In general, the process may also induce some phase noise that would destroy the quantum coherence. This can be tested in the simulated quantum regime, checking, with interference experiments, the preservation of the phase of the pulses before and after the conversion. However in our experiment we focused the attention more on the noise suppression than this last aspect. However results present in literature [54],[55], showed that the DFG process should preserve the light phase.

CHAPTER 3

EXPERIMENTAL SETUP AND TECHNIQUES

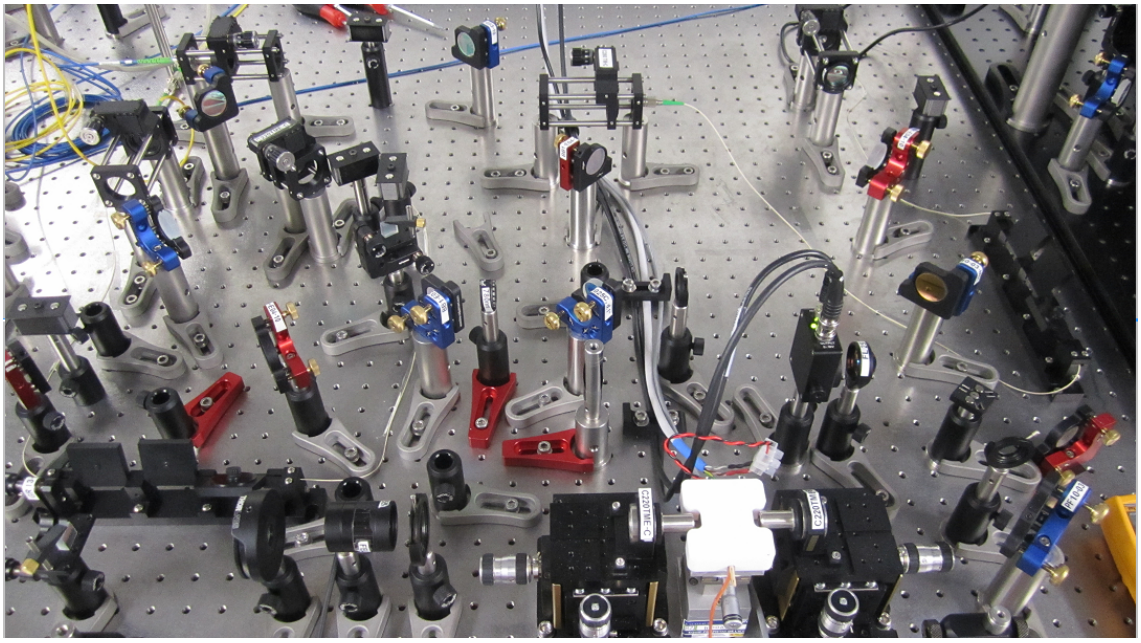

Figure 3.1: Overview of the experimental setup

The aim of this chapter is to present the setup that has been built to realize the experiment. The accurate description of the optical setup will be followed by the presentation of the main lab techniques used. In particular, the attention will be focused on the light pulses generation via acousto-optic modulation and on the single photon counting, both essential to run the experiment in the simulated quantum regime.

3.1 Experiment and setup description

The experiment carried out in this thesis work concerns the realization of an optical setup to perform wavelength conversion at the single photon level, for quantum communication applications. In particular it is designed to contribute to the implementation of a quantum repeater, based on ensembles of cold rubidium atoms, under development in QPSA group.
The goal is to build a very efficient setup that could be used to convert via difference frequency generation (DFG) the stream of single Stokes photons at 780 nm, coming from the atomic clouds, to 1550 nm, for optical fiber transmission.

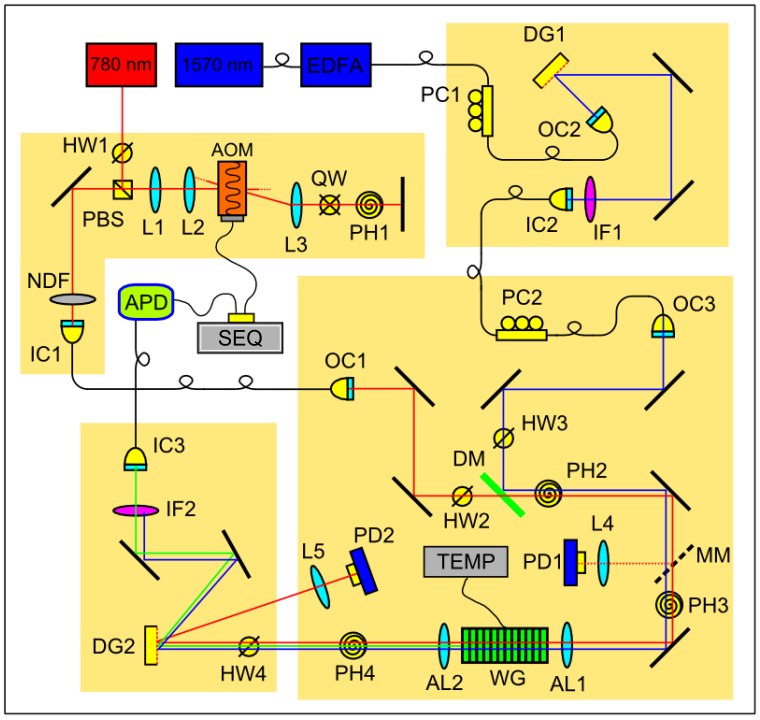

Figure 3.2: Experimental setup scheme. Legend: wave guide (WG), acousto-optic modulator (AOM), avalanche photodiode (APD), half wave plate (HW), quart wave plate (QW), polarization beam splitter (PBS), lens (L), aspheric lens (AL), fiber in/out coupler (IC/OC), diffraction grating (DG), dichroic mirror (DC), neutral density filter (NDF), interference filter (IF), photodiode (PD), polarization controller (PC), movable mirror (MM), pinhole (PH), temperature controller (TEMP), electronic sequencer (SEQ)

The schematic of the overall setup is shown in figure 3.2 and, in the following, each component will be indicated by its reference label according to its caption. The signal to convert (red) is provided by an amplified external cavity diode laser at 780 nm, giving 1.3 W of power and with a line width < 400 kHz (commercial, model TA-pro, from Toptica). Since the diode emits linearly polarized light, its power can

be set by means of a half wave plate (HW1) used together with a polarization beam splitter (PBS). Then the beam passes through an Acousto-Optics Modulator (AOM) in double passage configuration, that allows us to modulate its intensity. This permits to operate both in continuous and pulsed regime. The details of this part of the setup will be described in § 3.2.2. After the AOM the beam is strongly attenuated by a set of neutral density filters (NDF, figure 3.3), whose transmission at 780 nm has been accurately characterized. This allows us to reduce significantly and in a precisely controlled way the power of the laser beam. In this way we can operate in the so-called "simulated" quantum regime, where weak coherent light plays the role of the real single photons. In this regime we can test the efficiency and the signal to noise ratio (SNR) expected at the single photon level. The light is then coupled

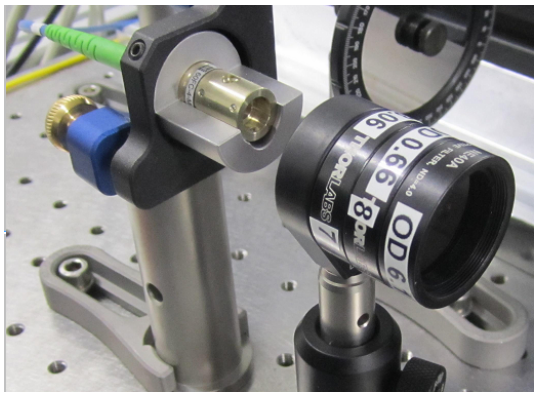

Figure 3.3: Neutral density filters

in a polarization maintaining optical fiber and re-collimated in the main part of the setup. A second half wave plate (HW2) is used to control the signal polarization, before the beam is overlapped to the pump by means of a dichroic mirror (see figure 3.4). The pump light is generated by another commercial external cavity diode laser at 1570 nm (model DL100, Toptica) followed by an EDFA amplifier, 33 dBm output power, (company Keopsys). Its spectrum is narrowed around 1570 nm by means of a filtering stage that is composed by the diffraction grating DG1, used together with a narrow band pass interference filter (IF1), with a bandwidth of 10 nm FWHM, centered at 1570 nm, peak transmission $> 90\%$, attenuation out of BW $= 10^6$ (Model NIR01-1570/3-25, from Semrock).

The two beams are overlapped with the help of the pinholes PH2 and PH3 and then are focused together by an aspheric lens (AL1, f = 11 mm) and coupled inside the PP-KTP waveguide. Both the coupling and the DFG are polarization dependent. For this reason the polarization of the pump light has to be controlled. This is achieved by means of a polarization controller combined with a half wave plate (HW3). Before the waveguide we installed a movable mirror (MM) that, when

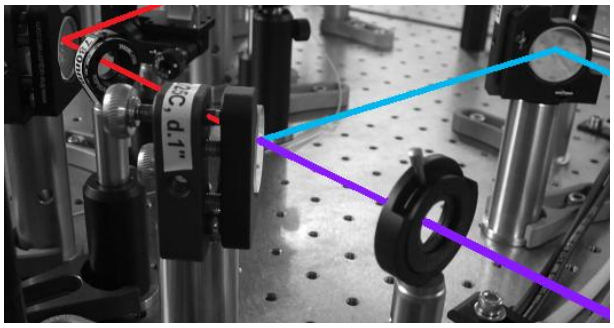

Figure 3.4: Signal (red) and pump (blue) light mixed through a dichroic mirror.

present, deviates the light to a fast photodiode, sensitive to 780 nm radiation. This allow us to monitor accurately the temporal power profile of the signal just before the conversion (figure 3.5).

As seen in § 2.1.4, the efficiency of the DFG process in a periodically poled crystal is very sensitive to temperature. The wave guide temperature is stabilized by a Peltier element controlled by an appropriate home made feedback electronic circuit.

At the waveguide output, the signal, pump and the generated 1550nm light are

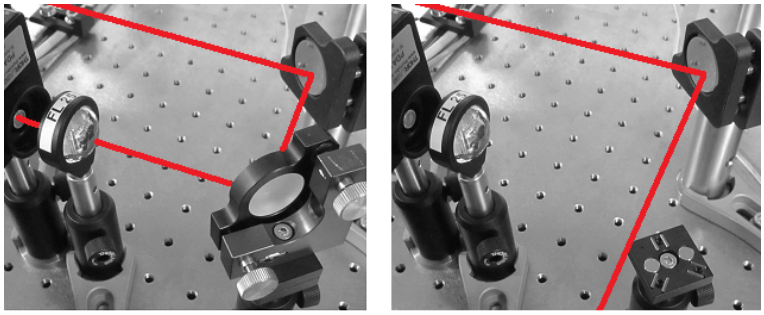

Figure 3.5: Effect on 780 nm beam when the movable mirror is present (a) or not (b)

collimated by an aspheric lens (AL2, f = 11 mm) and the spurious scattered light is filter by means of a pinhole. The three beams then pass through a filtering stage used to isolate the 1550nm component (figure 3.6). First they are separated by means of the diffraction grating DG2. A half wave plate, placed before it, permits to adjust the polarization direction and thus to optimize the diffraction efficiency. The 780 nm diffracted light is sent to another photodiode that, after a precise calibration, permits to monitor the depletion of the signal beam during the conversion process. The diffraction is not enough to provide an appropriate suppression of the pump light with respect to the converted signal, due to their spectral proximity. For this reason, another narrow band pass interference filter centered at 1550 nm (IF2)[1]

[1](Model NIR01-1550/3-25, from Semrock, with identical specifications of IF1.

is used to further attenuate the residual pump light. In addition to this, we used also a high pass filter (Mod. FEL1450, cutting wavelength = 1450 nm, Thorlabs) to eliminate also the second diffraction order of the light at 780 nm.

After this, the generated light is fiber coupled and sent to the single photon detector

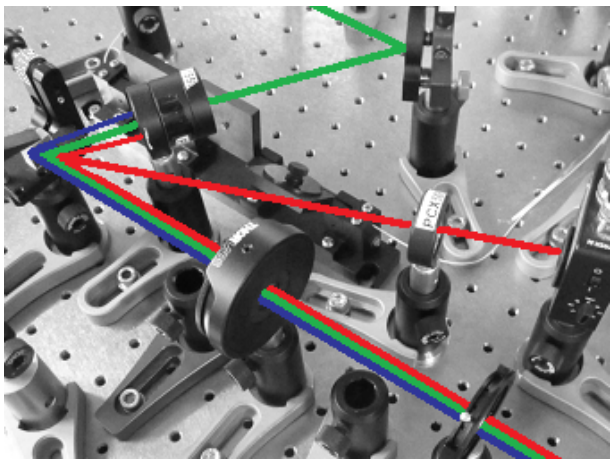

Figure 3.6: Filtering stage to isolate the 1550 nm light.

(APD). Since the latter operates in temporal gated regime, an electronic sequencer (SEQ) takes care about its synchronization with the arrival of 1550 nm signal.

3.1.1 PP-KTP crystal

As non linear medium to implement the DFG process, we chose the potassium titanyl phosphate ($KTiOPO_4$), shorten as KTP. Its maximum non linear coefficient[2] is $d_{33} = 17.4\,pm/V$. KTP is transparent in the range 400 nm - 4 µm and thus is suitable for our application.

We decided to adopt the configuration of collinear beams propagation in waveguide, in condition of quasi-phase matching. In this way is possible to fully exploit the maximum non linear coefficient because we can avoid the geometric constrains that arise from the phase matching condition. In addition, in guided propagation, contrary to the free space propagation, the beams can be tightly confined over long distances. This leads to higher optical intensities in the material and thus higher conversion efficiencies. For this purpose, we used a commercial periodically poled bulk crystal (poling period $\Lambda = 19.9\,\mu m$) with 22 wave guides (divided in 7 groups) fabricated on its top (company Advr Inc).

Most of the existing single photon conversion experiments are usually performed

[2]Instead of $\chi^{(2)}$, the non linear coefficient is often expressed as $d_{ijk} = \chi^{(2)_{ijk}}/2$ and the numerical subscripts refer to the crystallographic direction considered

in lithium niobate (PP-LN, $d_{33} = 27\,pm/V$). We choose PP-KTP in order to investigate the feasibility of performing quantum frequency down conversion in this material. A potential advantage of PP-KTP over PP-LN is that the poling process is better controlled, and that for example much shorter poling periods can be fabricated, which may be interesting for some wavelengths combinations. Therefore we chose PP-KTP also to test the noise performances of a different material.
We can see the crystal in figure 3.7. It is mounted on a copper crystal holder, specif-

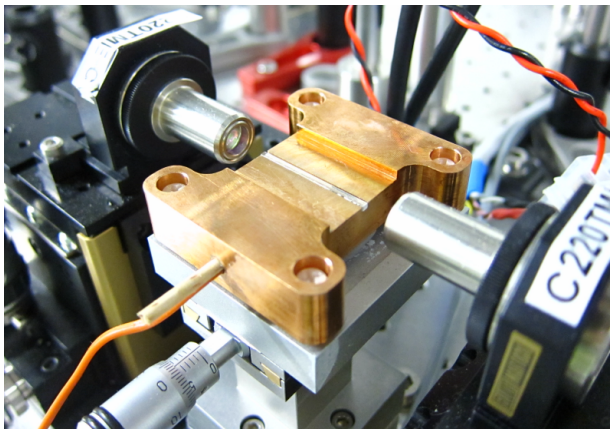

Figure 3.7: PP-KTP crystal

ically designed for this experiment and machined in the ICFO mechanical workshop. The temperature controller feedback circuit is connected both to a Peltier element (below the holder, in thermal contact with it) and to a temperature sensor in thermal contact with the copper. The crystal is glued on the holder with a silver paste, in order to improve the thermal conductivity between the two elements. This assures a more uniform temperature in the system when it is at the thermal equilibrium. To avoid heat dispersions, the holder is thermally isolated from the environment via a teflon[3] cap (not visible in figure 3.7). In addition, it is fixed to its aluminium support by means of 4 teflon screws that, together with the Peltier element, avoid any thermal contact between the two.
The holder is mounted on a translation stage, with sub-micrometric resolution, that easily allows, once a good coupling is established, to change the operating waveguide.

[3]a good thermal insulator material

3.2 Acousto-optic modulation

The typical temporal profile of the photons emitted by the atomic ensemble is gaussian, with FWHM between 30 and 100 ns. This duration is related to the excited state life time that is used in the memory experiment. In order to simulate these photons we need to be able to modulate the cw 780 nm signal at this time scale.
Acousto-optic technology, based on the interaction between electromagnetic and acoustic waves, is very versatile and suitable for a wide range of photonic applications. In particular, it can be employed to implement both frequency and amplitude modulation of a laser beam. An acousto-optic modulator (AOM) can be used as optical switch, with rise time performances in the nanoseconds range. We thus adopted this technology to shape our pulses.
In this paragraph I will explain the main physical principles of the acousto-optic modulation and how we used it in the experiment.

3.2.1 Physical principles

An AOM is a device in which a traveling longitudinal acoustic wave propagates in a block of optical transparent medium. This perturbation is usually induced by means of a piezoelectric transducer driven by a sinusoidal electric signal. The acoustic wave produces in the material a sinusoidal variation in the density, in the direction of the wave propagation. This leads to a modulation of the index of refraction (elasto-optical effect). The light that propagates in such medium experiences a sort of moving phase grating, and it can be partially or totally diffracted in one or more directions. Its functioning can be assimilated to that of x-ray diffraction in crystals. The first diffracted order can be ideally optimized to 100% efficiency. In practice, this can never be achieved, due to the finite extension of the acoustic wave. The intensity of the diffracted light depends on the acoustic power, in addition to the geometrical factors of the incident light beam and of the acoustic wave. For this reason, the intensity modulation of the light can be achieved acting on the acoustic power provided to the AOM. It can be thus used as switch for the diffracted beam, simply turning on and off the electric signal directed to the piezo. The rise time of such a switch depends directly on the speed to carry out this operation and it is ultimately limited by the time that the acoustic wavefront takes to cross the laser beam section.
The phase matching condition determines the direction of the diffracted beam. This

condition can be expressed as:

$$\vec{k_d} = \vec{k_i} \pm \vec{k_a} \tag{3.1}$$

where the subscripts d, i and a denotes respectively the diffracted, incident, and acoustic wave vectors, whose modulus is proportional to the different angular frequencies ω_d, ω_i and ω_a.

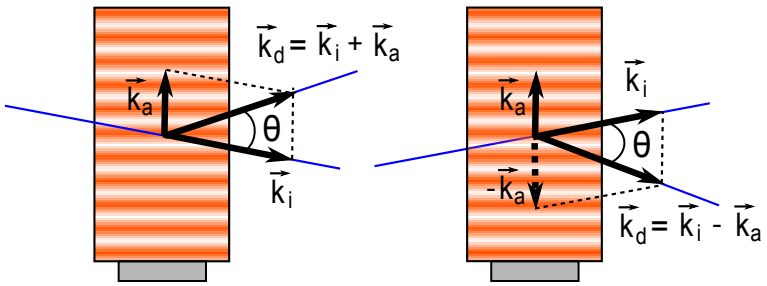

Figure 3.8: Aom phase matching condition.

If we consider a fixed geometry for $\vec{k_i}$ and $\vec{k_a}$, and (1) must always hold, it is evident that a variation of ω_a produces a change of the modulus and direction of $\vec{k_d}$. This leads to a shift in ω_d, expressed by the relation:

$$\omega_d = \omega_i \pm \omega_a \tag{3.2}$$

It is also possible to demonstrate that the angular position of the first diffracted order, with respect to the incident direction, is equal to:

$$\theta = \frac{\lambda_0 \omega_a}{2\pi v_a} \tag{3.3}$$

where v_a is the speed of sound in the medium.
The AOM can thus be used to modulate the direction the frequency and the phase of the light, acting on the frequency of the electric signal that drives the piezo.
The relations (3.1) and (3.2) can be easily understood phenomenologically, if we take into account the particle-like picture of the phenomenon. The optical beam and the acoustic wave can be thought as a stream of photons and phonons (quanta of mechanical waves) with a well defined momentum $\hbar\vec{k}$ and energy $\hbar\omega$. If we regard at the diffraction of the light as the elastic scattering of the photons against the phonons, the conditions (1) and (2) simply represent the momentum and energy conservation in the collision process.

3.2.2 Setup use and double passage configuration

As already mentioned (§ 3.1), we use the AOM in our setup as switch to create pulses. We chose the commercial device in figure 3.9, model MT110, from AA

optoelectronics. The maximum input power allowed to drive the piezo is $2W$. The speed of sound in its medium is $4200m/s$ and this leads to a rise time of $160\,nm$ per $1\,mm$ of incident beam diameter. However the rise time cannot be shorter than 15 ns (from specifications) due to the frequency of the RF signal and the finite response time of the piezo transducer. We drive the AOM with a fixed 110 Mhz frequency RF source, model MODAXX 1/2W, from AA optoelectronics. We can set the output power ($P_{max} = 2W$) with a input voltage signal from 0 to $5V$. The rise time of the RF source is $< 8ns$

To turn on and off the RF source, we employed the electronic sequencer from the company Signadyne, that will be described more accurately in § 3.3.4.

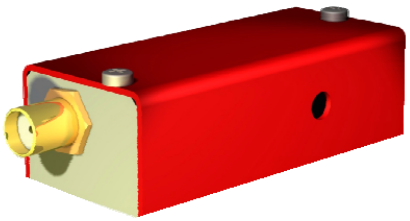

Figure 3.9: Commercial AOM device, model MT110, from AA Optoelectronic

Double passage configuration

In our setup we aligned the AOM as follows: right after the laser output, the linearly polarized 780 nm beam is reflected by a polarizing beam splitter (PBS). Its diameter is then reduced by the telescope built with L1 and L2 (focal distances equal to 75 and 25 mm respectively) and then it passes through the AOM. The diameter reduction is chosen to optimize the diffraction efficiency and the rise time performances. After that, the diffracted light is focused by a 150 mm focal lens (L3) on the surface of a mirror and is perpendicularly back-reflected. So it propagates backward, until the PBS. In this path, it passes twice across a quarter wave plate positioned between L3 and the mirror and so, when it arrives at the PBS, its polarization is 90° rotated and it is now totally transmitted. After this, the beam passes through the NDF and is fiber coupled.

This configuration is called double passage. Its advantage is that the position of the beam after the transmission through the PBS is no longer sensitive to variations of the acoustic frequency and so the subsequent alignment is much more stable. L3 transforms the angular dependence of the diffracted direction in a linear translation. In this way, it assures that the back and the forward propagating beams remain always overlapped.

3.3 Single photon counting

To measure the efficiency of the setup in the simulated quantum regime we need to count the events of photon conversion and this requires the detection of very low power optical signal (in the order of fW).
In this paragraph I will present the physical principles underlying the functioning of a "single photon avalanche diode" (SPAD) and why we chose this technology for our experiment. The aim is to show which are the crucial parameters of a SPAD and which are the criteria to set them. I will also briefly describe the photon counter we used and how.

3.3.1 Introduction

There are several kinds of photodetectors that reach single-photon sensitivity, like photomultiplier tubes, superconductivity based devices and avalanche photodiodes (APDs). Although the first exist for the wavelength range of interest, their quantum efficiency (counted/incident photons) is very poor, in the order of a fractions of percent. More efficient detectors, based on superconductive nano wires or Josephson junctions, have been recently proposed and tested, even at telecom wavelength, but their study is still in progress and their practical application is strongly limited by the extremely low temperature operating condition that they require to work properly (few K or even fractions of K).
Nowadays, the most practical technology in single photon detection is indeed represented by avalanche photodiodes, namely semiconductor devices in which an electric current (called photocurrent) is generated and auto amplified, after the absorption of light in the constitutive medium. These devices can be engineered to become sensitive even if the incident radiation is as week as at the single photon level and are called "single photon avalanche diodes" (SPADs).
Silicon based SPADs exhibit really great performances in detecting single photons in the 600 nm - 900 nm wavelength window, in terms of high quantum efficiency (up to 70 %), low noise (dark count rate <100 Hz) and sub-nanosecond time resolution. Unfortunately, silicon band structure (Eg = 1,12 eV) doesn't allow absorption of light with wavelength greater than 1,1 μm and thus another material is required to detect photon at 1550 nm.

As we can see in figure 3.10, germanium (Ge) and indium-gallium arsenide (InGaAs) seem to be good candidates to work in the telecom window. Ge-based devices, however, are affected by a high noise level and they have to be cooled below 150 K to work properly. This cooling, that is a practical limitation itself, causes also

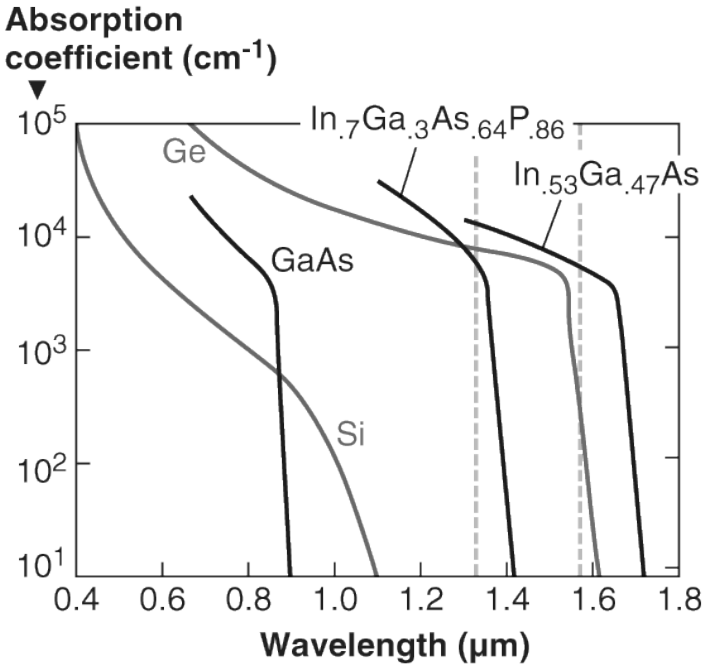

Figure 3.10: Variation of the absorption coefficient as function of the incident light wavelength for some semiconductor materials, commonly used in photodetectors fabrication. The telecom window lies in between the gray dashed vertical lines.// (Source: http://www.laserfocusworld.com/)

a shift in the band edge of the material such that the cutoff wavelength at these temperature is around 1450 nm. Consequently, the detection efficiency at 1550 nm drops drastically and this makes germanium unsuitable for our purpose. For all these reasons, the leading device for single photon counting in telecom c-band is the InGaAs-based SPAD.

3.3.2 Pin photodiodes, APDs and SPADs functioning

Pin photodiodes

A photodiode is basically a semiconductor pn junction. When the incident radiation hits the depletion region, it can be absorbed and promotes an electron from the valence to the conduction band. The generated electron-hole pair is then divided by the junction electric field and the two charges are accelerated in opposite directions. If these absorption events are enough and the charge trapping mechanisms inside the junction are negligible compared to the pair creation rate, a macroscopic photocurrent, proportional to the intensity of incident light, flows through the diode. When it is opportunely biased and inserted in an electronic circuit, this current, and so the light intensity, can be measured. In this devices, a layer of intrinsic (not doped) material is interposed between the p and n doped layers, in order to increase

the thickness of the depletion region (where absorption takes place) and to improve the sensitivity. Such devices are called p-i-n photodiodes.

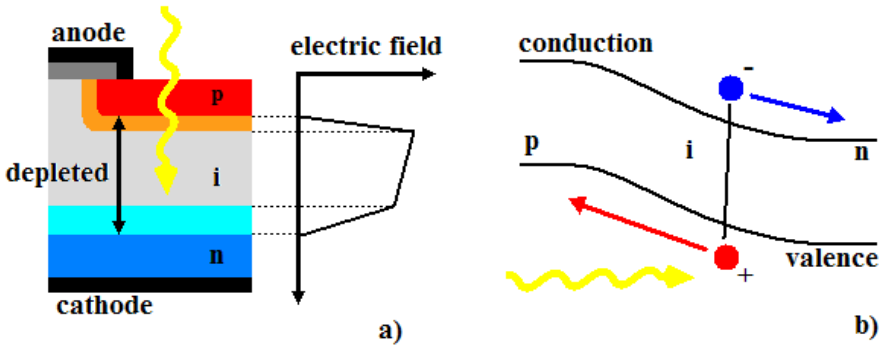

Figure 3.11: a) Schematic of the pin photodiode structure and junction electric field intensity. b) Band curvature of the material in the junction and pair separation mechanism.

For sensitive detections, the pin photodiode is often connected to an electrical amplifier. This solution is not the good way to perform single photon detection due to the noise introduced by the external amplification.

APDs

The problem described in the previous section can be overcome with the use of an avalanche photodiode (APD). This device can in fact provide an internal multiplication to the photocurrent. An APD is a pin photodiode, reversely biased with a strong voltage. The charges photo-created in the junction can gain energy during the acceleration process due to the high electric field across the structure. They can create secondary electron-hole pairs by impact ionization. These secondary charges are still strongly accelerated and can create other pairs and so on. This internal positive gain mechanism is called avalanche. It permits to obtain a relevant photocurrent, again linear with the intensity of the incident light, even if the latter is very weak.

To work in this regime, a below-breakdown biasing voltage (V_{BR}) is required. The breakdown is the threshold above which the electric field is so strong that a self sustaining avalanche can be eventually triggered by thermally generated pairs or by charge tunneling across the bands. In this case the gain provided by the avalanche is infinite and the electric current grows indefinitely, until the damage of the device itself.

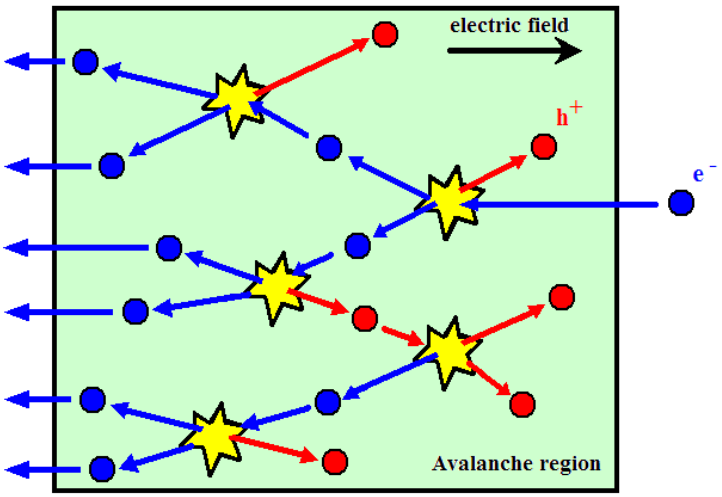

Figure 3.12: Pictorial representation of the avalanche.

SPADs

One way to perform single photon counting with an APD is to operate in the so-called Gaiger (or SPAD) mode, whose functioning is depicted in figure 3.13. The photodiode is biased beyond the breakdown threshold (point A). In this state, even a single event of pair creation due to the absorption of a photon can spark off an avalanche and trigger a macroscopic photocurrent that can be easily detected and counted by a proper electronic circuit (point B). After this, the voltage across the diode is reduced below threshold and the avalanche is limited and blocked, not to destroy the diode (point C). This process is called "avalanche quenching" and can be performed in several ways. Active and passive circuits are available for this purpose and the most suitable quenching method depends on the particular application. When the SPAD is completely reset, the voltage is restored again above threshold ad the device is ready to detect another photon.

The noise in a SPAD is represented by extra counts that don't correspond to any photon incidence. They can be divided in two different kinds: the dark counts and the afterpulses. The first are related to avalanches triggered by thermal excitations or by charge tunneling effects, when the device is in the A state. To limit this effect is important to keep the temperature of the junction low enough and not exceeding too much in the over-threshold biasing .On the other hand, the higher is the voltage, the higher is the probability that a photon trigs an avalanche. Moreover, a stronger voltage leads to a faster charge movement and so improves the time resolution of the SPAD. The biasing voltage is thus a crucial parameter and has to be accurately

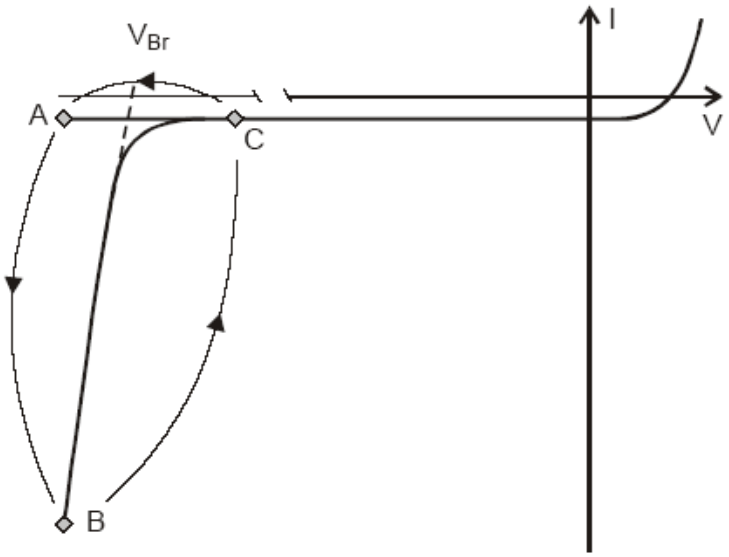

Figure 3.13: Current-voltage characteristics of a diode. First, SPAD is biased above breakdown (state A). When the single photon detection event takes place it goes in the state B and the current pulse is generated. The quenching circuit bring the SPAD to the state C and finally the system is restored to the initial state A, ready to another detection. (source: id201 Single-Photon Detector, application note "Single-photon detection with InGaAs/InP avalanche photodiodes")

chosen. An additional strategy to reduce the dark counts is to bring the system above V_{BR} only for a short interval of time, when the photon is expected to hit the detector. For the rest of the time, the voltage is kept well below V_{BR}. This operating method is called “gated mode” (in opposition to the “free running mode”) and is particularly useful when the signal to detect is periodic or, more in general, when it is possible to have an external signal which heralds the photon arrival. Of course, the longer is the gate, the higher is the noise.

The other noise contribution arises from the fact that, during an avalanche, some charges can get stuck in trapping energy levels in the multiplication region. If they are released after the restoring of the state A, they can initialize spurious avalanches and generate the so called afterpulses. High temperatures help to limit this phenomenon because the trap lifetime (in the order of μs) becomes shorter. There is thus a temperature trade off between low dark counts and low after pulsing probability. The operating temperature is another SPAD parameter that has to be accurately optimized to minimize its contribution to the noise. The main way to eliminate the afterpulses is to keep the junction below threshold (state C) for a long period, called dead time, after the avalanche quenching. If the dead time is long enough (more than the trapping lifetime), all the trapped charges are released when the device is still inhibited and no afterpulses are produced.

3.3.3 ID Quantique Id201 SPAD

To count our converted telecom photons we used the commercial id201 photon counter module, from the company ID Quantique. In this plug-and-play device, a fiber coupled InGaAs photodiode is integrated with all the electronics required and it is designed to work in the gated mode.

Figure 3.14: Id201 photon counter module.

The photodiode

The structure of the photodiode is a bit more complicate than what is shown in fig 3.11 because different materials are employed in its design. The photons are absorbed in the $In_{0,53}Ga_{0,47}$As layer and then the generated charges (the holes in particular) are injected in a indium phosphide (InP) pn junction where the avalanches are triggered. InP has a wider bandgap ($Eg^{InP} = 1,3eV$) than InGaAs ($Eg^{In_{0,53}Ga_{0,47}As} = 0,73eV$) and so less dark counts are produced in this region. A grading InGaAsP layer is inserted between the two materials to have a gradual transition and to smooth the energy discontinuities that usually characterize the band alignment of eterojunctions. In this way it is possible to reduce the charge trapping effects at the interface and to improve the temporal performances of the device.

Parameters setting

In Id201 SPAD different parameters can be set by the user.
First of all, is possible to choose the detection efficiency. The available values are 10%, 15%, 20% and 25%. The different possibilities correspond to different biasing voltages above V_{BR}, that for $In_{0,53}Ga_{0,47}As$ is around 50 V. Higher efficiencies produce also higher dark counts rate.
The dead time duration can also be set to reduce the afterpulsing. The choice is

between 0, 1, 2, 5, 10, 20, 40, 60, 80 and 100 μs.
Since Id201 SPAD works in the gated mode, different options are available to trigger the detection gates. If the internal trigger is chosen, the rate can be set to 1, 10, 100 kHz or 1 MHz. The detection gating can be also driven with an external signal (TTL, or other standards are recognized) and in this case the maximum accepted frequency is 19 MHz. A delay between the triggering event and the effective gate activation can be eventually add and set in the range 0-25 ns.
The gate width can be adjusted to optimize the detection of the photons. For this parameter, the possible values are 2.5, 5, 20, 50 and 100 ns.
The temperature of Id201 SPAD is internally controlled and kept at the fixed optimum value of 220 K.

3.3.4 SPAD use in the experimental setup

As already mentioned (3.1), the experiment is run in the simulated quantum regime, both with continuous and pulsed signal. In the former case the SPAD is easily used with its internal trigger, but in the latter is necessary to synchronize the triggering events with the arrival of the weak 1550 nm pulses on the detector. This duty is carried out by a flexible electronic control unit (Programmable Arbitrary Mixed-signal Controller PAMC from Signadyne company).

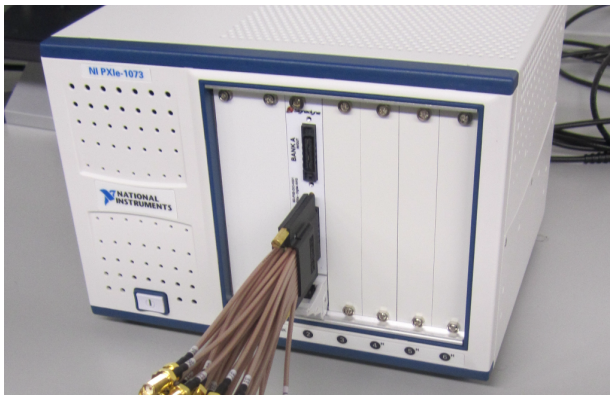

Figure 3.15: Signadyne control unit.

It supports a programmable electronic sequencer that can drive independently up to 64 digital output channels, in TTL mode. The output n.1 is connected to the amplitude controller input of the RF source that drives the AOM. The output n.2 is connected to the external trigger input of the SPAD. The simple cyclic program shown in figure 3.16 is loaded in the sequencer processor. It is an infinite loop in which, the output n.1 and n.2 are alternately turned on and off. Adjusting opportunely the time intervals (t1-t6) between each block and the internal delay

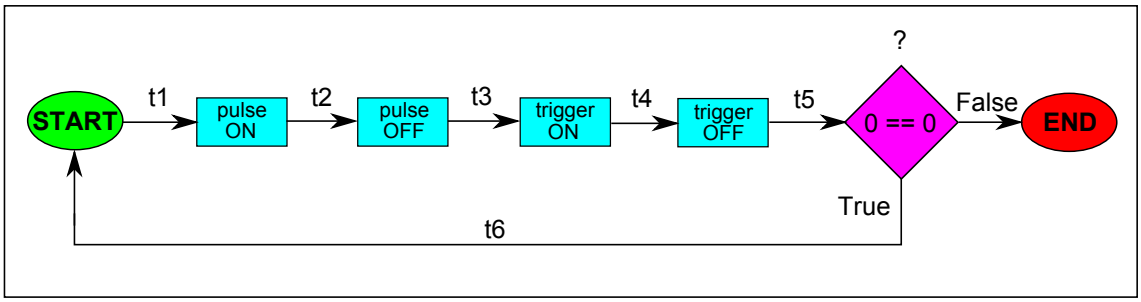

Figure 3.16: Bloch scheme of the synchronizing program. Pulse ON/OFF set to high/low voltage the output n.1 while Trigger ON/OFF set to high/low voltage the output n.2

generator of the SPAD, it is possible to change both the duration of the pulses and to synchronize the system.

It is very important to underline that and APD should be used in the SPAD mode, in the simulated quantum regime, only when the incident coherent light is so weak that, at most, just a single photon hits the detector. This means that the average number of photons carried by the beam (continuous or pulsed) per gating length has to be equal to some fractions of unity. In this way, this number (that is very important for the efficiency characterization of our setup) can be truly estimated as the ratio between the frequency of photon counts and the frequency of gate triggering. This is called “linear regime”. Otherwise, if the light is not weak enough, the measurement becomes meaningless, because the SPAD will tend to count a photon per each gate and that ratio will just saturate to 1. Too high powers may damage the detector.

CHAPTER 4

EXPERIMENTAL RESULTS

The aim of this chapter is to show the results obtained in the wavelength conversion experiment.
In the first part of the chapter I will present the DFG characterization of our setup in the classical regime. Then I will show in detail how we turn to the simulated quantum regime and the conversion performances that we can obtain. All the names of the setup elements are referred to the convention established in figure 3.2

4.1 DFG characterization in classical regime

I present in this paragraph the dependence of the DFG on several experimental parameters, such temperature, light polarization and powers. During these measurements, all the parameters but the one under test are already optimized. I will then define the total efficiency of the setup and I will show the best performances we can obtain.
We tested the DFG in all the wave guides fabricated on the top of our crystal and the following measurements were carried out in the one which showed the best conversion efficiency.

4.1.1 Light coupling into the WG

The coupling is done focusing the 780 nm and 1570 nm beams on the input facet of the waveguide (n. 3.3[1], rectangular, $4\,\mu m \times 4\,\mu m$).

- OC1: Aspheric lens, f=8 mm, model Thorlabs A240-TM, B[2]
- OC3: Aspheric lens, f=18 mm, model Thorlabs C280-TME, C coated
- AL1: Aspheric lens, f=11 mm, model Thorlabs C220-TME, B coated

AL1 is mounted on a x-y-z translation stage whose movements can be controlled accurately in the µm scale.
The coupling efficiencies for the 780 nm and 1570 nm beams will be indicated ϵ_{coup}^{780} and ϵ_{coup}^{1570} respectively. They are defined as the ratio between the powers transmitted by the WG (measured after the pinhole PH4) and the power before AL1.
We measured $\epsilon_{coup}^{780} = 28(3)\%$ and $\epsilon_{coup}^{1570} = 32(3)\%$. The main limitation that affect these values arise from the difficulty in focusing two beams with very different wavelength with the same lens on a relatively small area. AL1 doesn't compensate the chromatic aberrations, with repercussions on ϵ_{coup}^{780} and ϵ_{coup}^{1570}. A telescope opportunely designed and placed in one of the two arms could help to partially improve the coupling efficiencies. It's important also to highlight that the reported values include also the propagation loss in the WG. While the propagation loss are small for telecom light (< 0.2 dB per cm), they can be as high as 1 dB per cm, according to the supplier. However, we haven't measured the loss for our particular device.
We didn't observe a very significant variation in this value varying the input powers. The small influence of the pump input power visible in fig. 4.1 can be related to

[1]The waveguides are numbered in the crystal manual

[2]The antireflection B coating is for the wavelength range 650-1050 nm. The C coating is for 1050-1520 nm.

a local thermally-induced mechanical stress in the WG. This can be compensated with small adjustments in the alinement and the temperature.

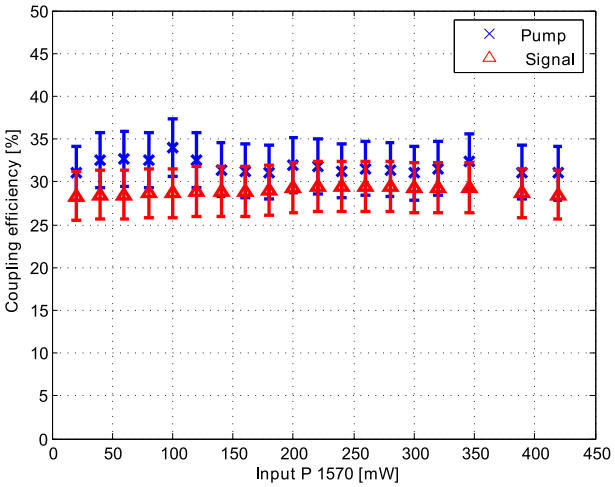

Figure 4.1: Coupling efficiency of the signal (triangle) and pump (x), measured with respect to the input pump power.

4.1.2 Generation efficiency

We studied the behavior of the generated light with respect to the pump and the signal input powers. The two measurements are shown in figure 4.2 and 4.3. We

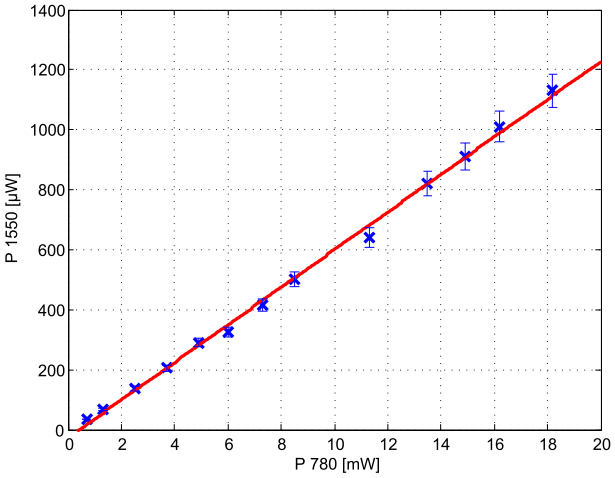

Figure 4.2: 1550 nm power generation vs 780 nm power coupled in the waveguide. In this measurement $P_{coup}^{1570} = 135mW$.

see that the dependence for both beams is linear and thus we are operating in the weak interaction regime, deeply discussed in chapter 2. In this case the normalized

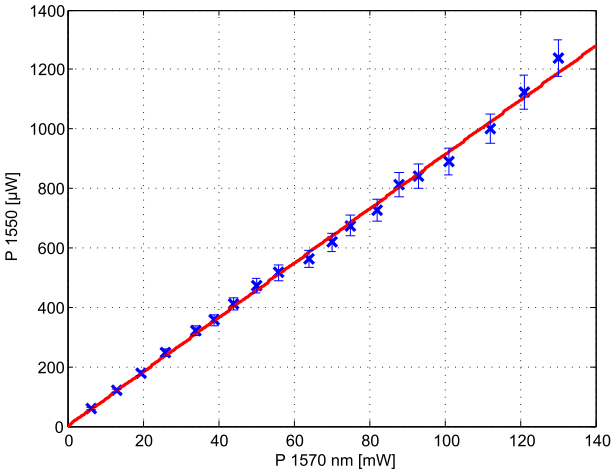

Figure 4.3: 1550 nm power generation vs 1570 nm power coupled in the waveguide. In this measurement $P_{coup}^{780} = 21mW$

generation efficiency η_{gen} can be defined as:

$$\eta_{gen} = \frac{P_{gen}^{1550}}{P_{coup}^{780} P_{coup}^{1570}} \quad [W^{-1}] \tag{4.1}$$

where P_{gen}^{1550} is the generated 1550 nm light measured after the pinhole PH4 located after the waveguide., and P_{coup}^{780} and P_{coup}^{1570} are the signal and pump coupled power into the waveguide. In the approximation of strong pump, i.e. when the power variation of the 1570 nm beam can be neglected, it represents the fraction of the signal beam that is converted per 1 W pump power. If the pump power is too high, the generation starts to saturate and (4.1) is no longer valid.
As we saw in § 2.1.4, the generation efficiency is directly related to the achievement of the quasi-phase matching condition and its maximum value depends on the degree of nonlinearity of the material. For our waveguide, the specified maximum η_{gen} obtainable is $60\%/W$. The best we measured is $\eta_{gen} \approx 45(4)\%/W$. The discrepancy between the two values may be related to the non perfect spatial mode overlapping of signal and pump inside the waveguide.
We also verified that this value remains constant (within the experimental errors) varying the input powers, as we can see in figures 4.4 and 4.5.

4.1.3 Temperature

We also studied how temperature influences the DFG process. Variations of the waveguide temperature induce a change of the crystal length, which in turn affects the poling period. Therefore, the quasi-phase matching condition can be achieved by tuning the crystal temperature.

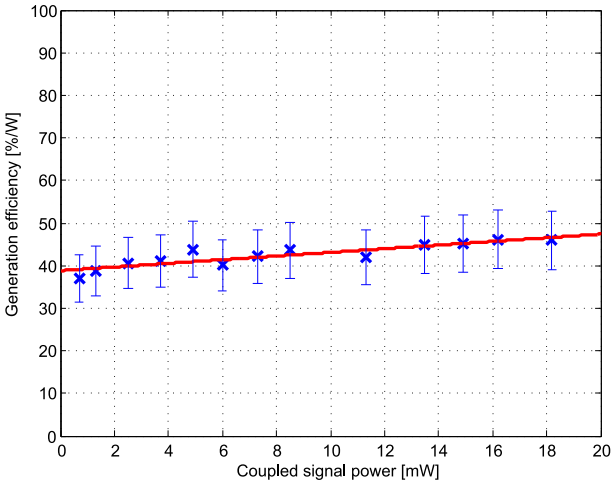

Figure 4.4: Generation efficiency variations with 1570 nm coupled power.

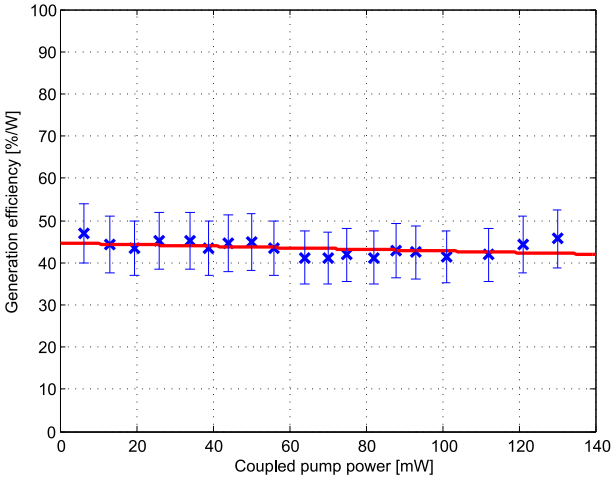

Figure 4.5: Generation efficiency variations with 1570 nm coupled power.

We did a temperature scan and the result is shown in figure 4.6. We see that this measurement doesn't reproduce the $sinc^2$ curve predicted by the theory (see § 2.1.3, fig 2.2). One possible reason could be that the alignment should be constantly adjusted during the scan, to compensate the mechanical effects induced by the temperature variation. Another possible explanation is that the wavelength of the signal was not stable during the measurements, which may have affected the result. However, this measurement can be used to determine that the best temperature range to operate is approximately around 50 °C. The precise value has to be searched day by day, due to the small signal wavelength variation. However it is never oustisde the range 48°C-52°C.

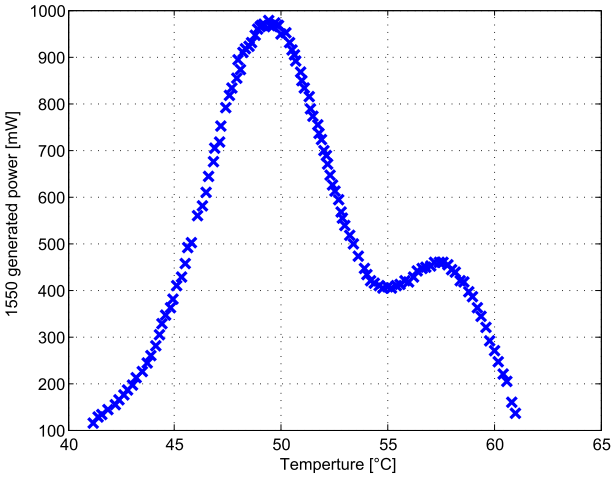

Figure 4.6: Temperature scan.

4.1.4 Conversion efficiency

If we look the DFG process from the photon perspective, we are interested to describe the efficiency of the conversion in terms of:

$$\eta_{conv} = \frac{R_{gen}^{1550}}{R_{inj}^{780}} \tag{4.2}$$

where R_{gen}^{1550} and R_{inj}^{780} denote the photon creation/injection rate respectively. This definition of η_{conv} is equivalent to the one we introduced in § 2.1.6. In quantum optics, the energy conservation for the DFG is written as:

$$\hbar\omega_{1550} = \hbar\omega_{780} - \hbar\omega_{1570} \tag{4.3}$$

This means that, in the conversion, there is a one-to-one correspondence between the rate of 1550 nm photons creation and 780 nm photons annihilation. We can thus manipulate the (4.2) as follows:

$$\eta_{conv} = \frac{R_{gen}^{1550}}{R_{inj}^{780}} = \frac{R_{ann}^{780}}{R_{inj}^{780}} = \frac{\frac{P_{dep}^{780}}{\hbar\omega_{780}}}{\frac{P_{out}^{780}}{\hbar\omega_{780}}} = \frac{P_{out}^{780} - \widetilde{P}_{out}^{780}}{P_{out}^{780}} \tag{4.4}$$

R_{ann}^{780} denotes the 780 nm photon annihilation rate. P_{dep}^{780} is the 780 nm depleted power, calculated as the difference of the 780 nm power at the output of the guide with the pump off (P_{out}^{780}) and on ($\widetilde{P}_{out}^{780}$).
Equivalently, we can rearrange the (4.2) in this other way:

$$\eta_{conv} = \frac{R_{gen}^{1550}}{R_{inj}^{780}} = \frac{\frac{P_{gen}^{1550}}{\hbar\omega_{1550}}}{\frac{P_{out}^{780}}{\hbar\omega_{780}}} = \frac{P_{gen}^{1550}}{P_{out}^{780}}\frac{\lambda_{1550}}{\lambda_{780}}$$

Multiplying and dividing this expression by P_{coup}^{1570} and using the (4.1), we finally obtain:

$$\eta_{conv} = \eta_{gen} P_{coup}^{1570} \frac{\lambda_{1550}}{\lambda_{780}} \tag{4.5}$$

Equation (4.4) shows that the conversion efficiency in terms of photon numbers can be obtained measuring, in the classical regime, the relative variation with and without the pump of the 780 nm power coupled in the waveguide. We measured it and, by means of eq. (4.5), we compared it with the measurement of η_{gen}, to check if the two are consistent.

Measuring $\widetilde{P}_{out}^{780}$ is not straightforward since all the beams leave the waveguide overlapped. We must measure P_{out}^{780} in a indirect way. After the diffraction grating (DG2), the 780 nm first diffracted order is well isolated and it is sent to the photodiode PD2. We calibrated the voltage signal given by the photodiode with the 780 nm power after the WG in the absence of the pump and we observed a liner relation between the two. The result is shown in fig 4.7. Inverting the relation given by the

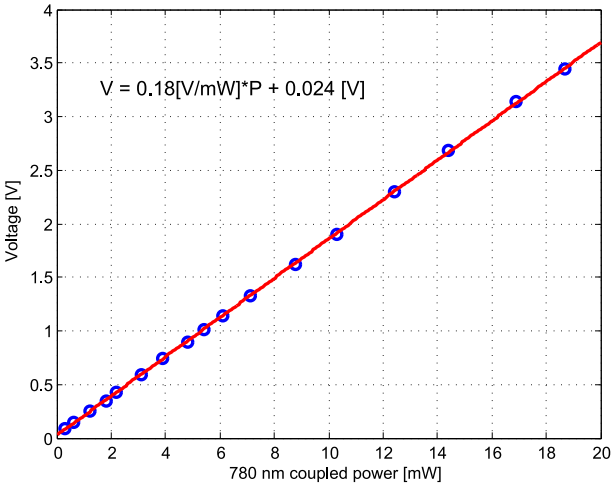

Figure 4.7: PD2 calibration fitting.

Matlab fitting we obtain the following calibration equation:

$$P_{out}^{780} = 5,5\frac{mW}{V}V_{ph} - 0,13mW \tag{4.6}$$

With eq. (4.6) we can measure $\widetilde{P}_{out}^{780}$. In fig 4.8 we can see the depletion of the signal beam as function of the coupled pump power. Again we observe a linear behavior. In fig 4.9, we compare graphically the quantities η_{conv} and $P_{coup}^{1570} \cdot \eta_{gen}$. Making numerically the ratio of the two fitted lines between $x = 20$ and $x = 140$, we find a more or less constant value very close to the factor $\lambda_{1550}/\lambda_{780}$. This proves the consistency between our measurements of η_{gen} and η_{conv} with the relation (4.5).

Using the formula (4.5) we can calculate the best value of η_{conv} that we can obtain. Considering that the maximum pump power that we can couple into the waveguide is $P_{coup}^{1570} = 155(7)\,mW$ and using a $\eta_{gen} = 0.45(4)\,W^{-1}$, we obtain the

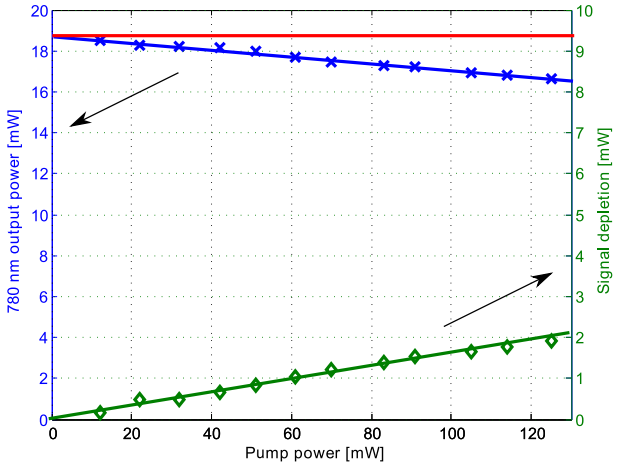

Figure 4.8: Measure of the depletion of the signal beam. (continue line): coupled 780 nm light. (x): 780 nm power at the output of the waveguide. (diamonds): signal beam depletion.

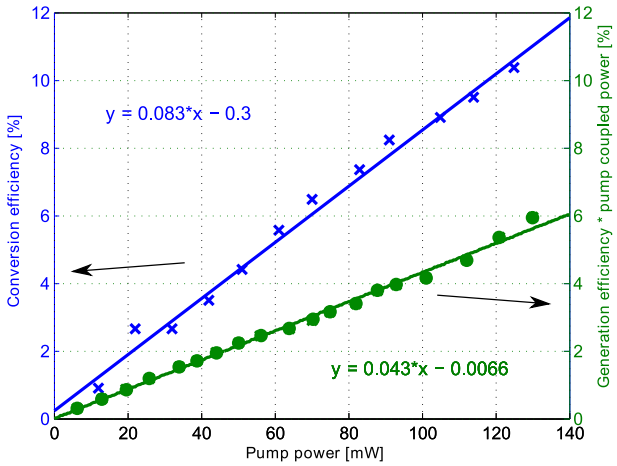

Figure 4.9: Comparison between η_{coup}(x) and η_{gen} (dots) as function of the pump power. We can observe that, according to their definitions, they differ almost of a factor 2.

result:

$$\eta_{conv} = 14(1)\,\% \tag{4.7}$$

4.1.5 Dependence on the polarizations

We also analyzed the behavior of the setup with respect to changes in the polarization direction of the signal and the pump. We measured how these two parameters influence the generation of the light and how they affect the coupling in the waveguide. We can rotate the polarization directions acting on HW2 and HW3, for the signal and the pump respectively.

First we did a crossed scan between the two polarizations, recording P_{gen}^{1550}. During this measurement, the power of the input beams were fixed at $P_{coup}^{780} = 21mW$ and

$P_{coup}^{1570} = 420mW$. The result is shown in figure 4.10. We can see that the DFG is

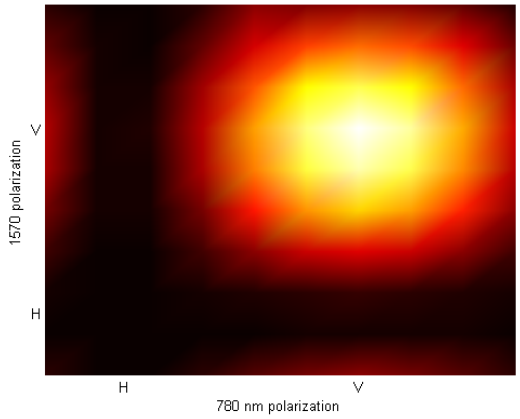

Figure 4.10: Crossed polarization measurement. The brighter is the color, the higher is the 1550 nm power recorded. The range is from 2µ to 1300 µW.

extremely sensitive to the polarization. Vertical polarization is required for both the beams to achieve the best generation efficiency. If one or both are horizontal, η_{eff} is reduced significantly, from $1300\mu W$ to $2\mu W$.

We wanted to check if this behavior is influenced by other polarization dependent effects, not directly related to the non linear process, that can have repercussions on the 1550 nm light generation. We thus studied whether the polarization affects the coupling efficiencies. We did two independent scans for the signal and the pump. During this measurement, the polarization of the beam not under test was kept vertical. We show in figure 4.11 and 4.12 the results, compared with the correspondent behavior of η_{gen}. We see that the influence on $\epsilon_{coup}^{780,1570}$ is much weaker than on

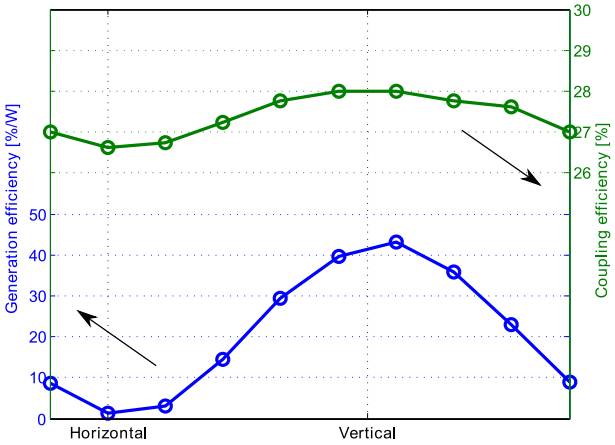

Figure 4.11: ϵ_{coup}^{780} and generation efficiency variation with 780 nm polarization direction.

η_{gen}. It can be explained by the difference in the transverse spatial modes that are

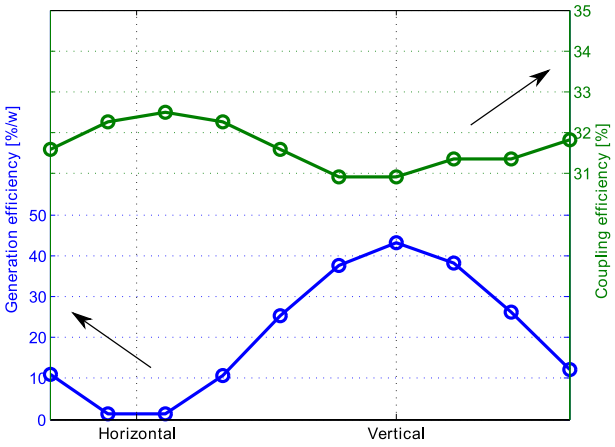

Figure 4.12: ϵ_{coup}^{1570} and generation efficiency variation with 1570 nm polarization direction.

excited in the waveguide, when the polarization direction changes. For the ϵ_{coup}^{780}, the vertical polarization is still the optimum direction. On the other hand, the pump beam reach its best coupling when the polarization is horizontal. From these measurements we can see that the dependence of the couplings from the polarization is weak enough not to influence the generation efficiency.

4.1.6 Total efficiency

The main goal at this stage is to optimize the total efficiency η_{tot}, defined as follows:

$$\eta_{tot} = \frac{R_{SPAD}^{1550}}{R_{inj}^{780}} \tag{4.8}$$

where R_{SPAD}^{1550} is the converted photons rate that hit the SPAD.
The meaning of this parameter can be understood considering that, if N photons at 780 nm enter in the setup, only $\eta_{tot} \cdot N$ will arrive at the SPAD input. It takes into account the possible losses of the light, from the waveguide input until the photodiode. It can be expressed as follows:

$$\eta_{tot} = \epsilon_{coupl}^{780} \cdot \eta_{conv} \cdot \eta_{filt} \tag{4.9}$$

We already discussed about ϵ_{coupl}^{780} and η_{conv} in sections 4.1.1 and 4.1.4. η_{filt} is the transmission efficiency of the filtering stage after the waveguide and it is defined as follows:

$$\eta_{filt} = \eta_{diff} \cdot \eta_{coup} \cdot \eta_{conn} \tag{4.10}$$

where

- η_{diff} is the diffraction efficiency of DG2. Is defined as the ratio between the 1550 nm power in the first diffracted order and after the waveguide. Its value

depends by the incident angle on the grating and by the polarization direction that is controlled with HW4. The best value we measured is around 60(4)%.

- η_{coup} is the coupling efficiency of the 1550 nm light into the fiber after IC3. We tried several lenses to optimize it and the best value we obtained is around 40(3)% with the Thorlab aspheric lens, model 560-TME C coated, focal length = 13,86 mm. This coupling is limited by the beam profile distortion caused by the diffraction from DG2.

- η_{conn} is caused by the losses introduced by a FC/APC-FC/PC connector used to bring the 1550 nm light until the input FC-PC SPAD connector. Its values is around 60(4)%.

The value of η_{filt} that follows from this values is equal to 14(2)%.
All the optical losses are summarized in the following table:

ϵ_{coup}^{780}	0.28(3)
η_{diff}	0.6(4)
η_{coup}	0.4(3)
η_{conn}	0.6(4)
η_{filt}	0.14(2)

Expanding (4.9) with the definitions of the intermediate efficiencies we obtain:

$$\eta_{tot} = \frac{P_{before\,SPAD}^{1550\,nm}}{P_{before\,WG}^{780\,nm}} \frac{\lambda_{1550}}{\lambda_{780}} \tag{4.11}$$

We measured a maximum value of $\eta_{tot} = 0.62(4)\%$ with $P_{coup}^{1570} = 155(7)mW$.
The uncertainties are fully related to the measurement of the light power with the Thorlabs powermeter, whose uncertainty is round 5%.

4.2 Conversion in the simulated quantum regime

The purpose of this step is to test to what extent the classical coherent light at 780 nm can be attenuated, maintaining a signal-to-noise ratio (SNR) above 1 in the detection of the converted 1550 nm light. In order for the device to work as quantum frequency converter, it should convert a single photon with good enough fidelity (as discussed in § 2.2.5). The ideal goal would be to have a high SNR with the 780 nm light attenuated at the single photon level before the waveguide. This would permit to convert with high fidelity the photons coming from the cloud.
In this paragraph I will first present the noise characterization that we have at the single photon level. During these measurements, the 780 nm light was always off and no DFG takes place. Then I will show the SNR results that we can obtain with our setup, operating in the pulsed regime. In the end I will discuss about how the photon length influences the experiment on the basis of some measurement taken in the continuous wave regime.

4.2.1 Noise characterization

In our experiment we consider as noise all the photon counts that are not induced by the 1550 nm converted light. We see in this section which are the main noise sources and how we limit them.

Dark counts and afterpulses

As already discussed, there are intrinsic noise factors in the SPAD functioning, namely dark counts and afterpulses. They can be limited choosing properly the SPAD parameters. The dark count probability is fixed by the SPAD temperature and the biasing voltage. The first is not adjustable and is fixed at -50(2)°C (from id201 SPAD operating manual). We can set the second choosing the detection probability. We decided to keep this value fixed at 10% (the minimum available) to limit the dark counts as more as possible. With internal trigger at 1 MHz, dead time = 20 µs, and the SPAD optical input closed, we observed a dark count probability of $7 \times 10^{-6}\,(ns)^{-1}$.

In order to reduce the afterpulses, it is important to insert a suitable dead time in the APD. To choose it, we did the following experiment. We fixed the value of the pump power in the waveguide to $P_{pump} = 144mW$ and the trigger rate to 1 Mhz. We measured the noise counts, varying both the dead time and the gate

width. When the dead time is not fixed to 0, some detection gate may be lost. The significant data in this case is the ratio R between the counts and the triggering rate. The results are visible in figures 4.13: We expect a linear dependence of the noise

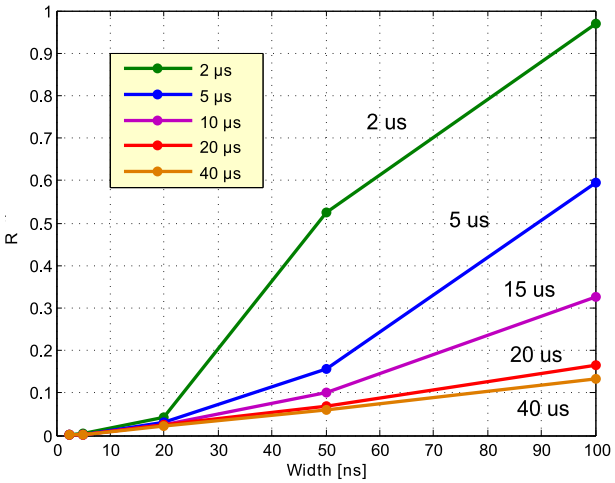

Figure 4.13: Counts/Trigger as function of the gate width, for different dead times.

level with respect to variation of the detection gate width. However, we can see in fig 4.13 that this dependence is quite irregular if the dead time set is smaller than 20 µs. In addition, if the gate length is fixed, the noise detection should not depend from the duration of the dead time. Again we see that this is true only for dead times higher than 20 µs. We thus relate the noise behavior with dead time $< 20\,\mu s$ as the consequence of the afterpulses. From these results we infer that a dead time of $20\mu s$ is sufficient to suppress the contribution of the afterpulses. From now on, unless otherwise specified, all measurement are made with a 20 us dead time.

Spurious light

The main noise source of our setup is indeed represented by the spurious light that hits the detector. This contribution is "external", in the sense that it comes from the experimental setup and is not intrinsic to the SPAD functioning. We can identify two kinds:

- the 1550 nm light that arrives at the SPAD but is not generated by DFG. This arises from two independent sources:

    1. Amplified spontaneous emission (ASE) in the EDFA causes a pump spectrum broadening with non-zero contribution at 1550 nm.
    2. The strong pump produces 1550 nm lights inside the nonlinear crystal and the optical fibers via Raman scattering.

Both this two contributions remain overlapped to the converted signal and reach the SPAD[3].

- the residual 1570 nm light transmitted by the filter after the WG. It can be detected because 1570 nm is still well absorbed by InGaAs (see figure 3.10) and the SPAD is not able to discriminate it from the 1550 nm light.

To characterize the external noise we first measured the broadened spectrum of the pump light with a spectrum analyzer (model OSA: AQ6370 from Yokogawa, 0.02 nm resolution in the analyzed band). The result is visible in figure 4.14. We can

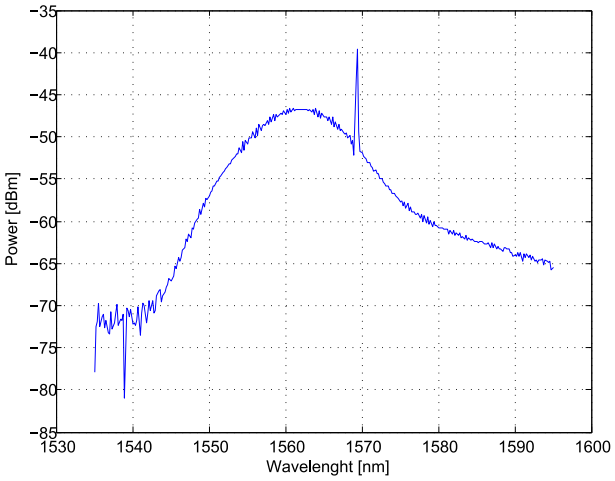

Figure 4.14: Spectrum of the pump power after the amplifier. The vertical scale is logarithmic. The apparent limited signal to ASE ratio is caused by the fact that the resolution of the spectrum analyzer (0.02 nm) is larger than the pump laser line width. In practice, the peak intensity at 1570 nm is several orders of magnitude higher than the ASE.

observe that the sharp peak at 1570 nm is surrounded by a strong background, with components at 1550 nm. We then measured the pump spectrum after fiber coupler OC3 and without the band 1570 nm band pass filter (IF1), to evaluate the effects of the diffraction grating DG1 on the background noise. We later multiplied the measured spectrum by the spectral transmission function (taken from the technical specifications) of the band pass filter at 1550 nm (IF2) alone (fig. 4.15) and with both IF1 and IF2 in cascade (fig. 4.16). The blue curves represent an estimation of the noise spectrum that reaches the APD in the absence of 780 nm light. They don't take into account the Raman scattering in the crystal and the filtering effect of the diffraction grating after the waveguide (DG2).

[3]There is a third possible source of noise at 1550 nm: the spurious parametric down conversion due to the non perfect poling period of the crystal. In practise we don't have this noise because, for energy conservation, this effect cannot happen if the pump has a higher wavelength than the converted signal.

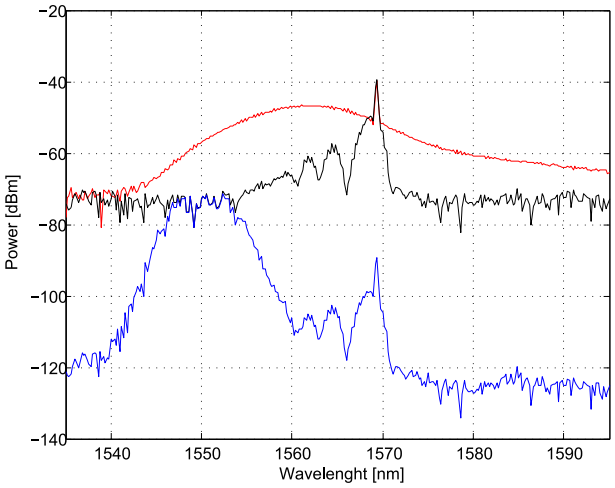

Figure 4.15: The pump spectrum (red) is filtered by DG1 (black) and then by IF2 (blue).

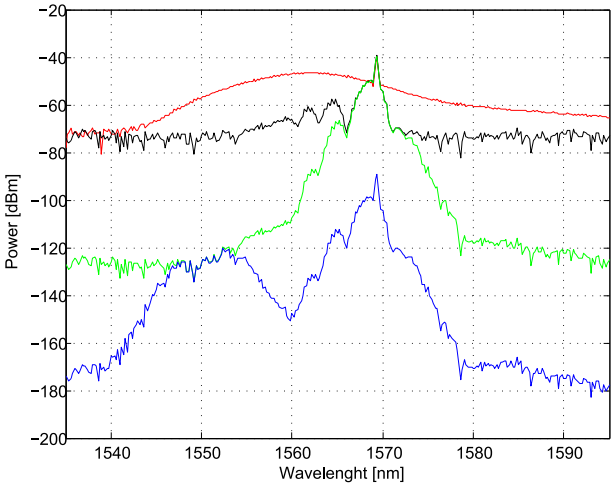

Figure 4.16: The pump spectrum (red) is filtered by DG1 (black), then by IF1 (green) and finally by IF2 (blue).

We then try to validate this estimation observing the noise detected with the SPAD. We fixed the settings as follows: Internal trigger at 1 MHz, no dead time[4], gate width = 5 ns. We then measured how the count rate varies, changing the power of the pump. We did the measure without IF1 and we observed a very high noise signal, close to the saturation of the SPAD, i.e. when the counts rate tends to be equal to the trigger rate. We did the measure again, now with IF1, and the noise level dropped of a factor 500. The results are shown in figure 4.17. We can also observe (fig 4.18) that the noise count rate is proportional to the pump power.

The reduction factor agrees with the difference of the integrals (made numerically) of the blue curves in figure 4.15 and 4.16. This means that the high noise level detected without IF1 must be related to the background at 1550 nm in the pump

[4]Chronologically, we did this measurements before the dead time optimization.

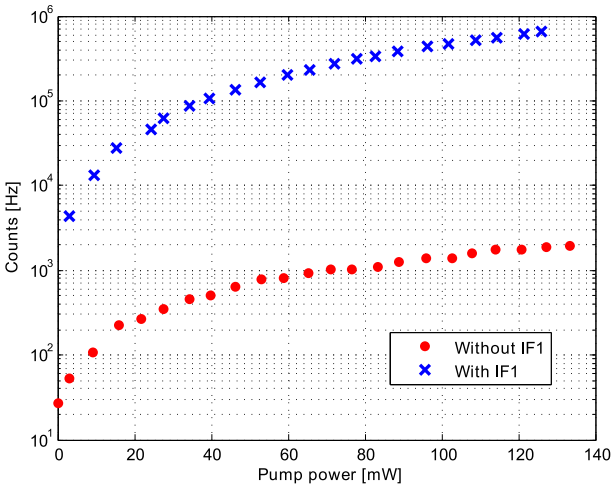

Figure 4.17: Noise level as function of the pump power with (red) and without (blue) IF1, measured with the SPAD

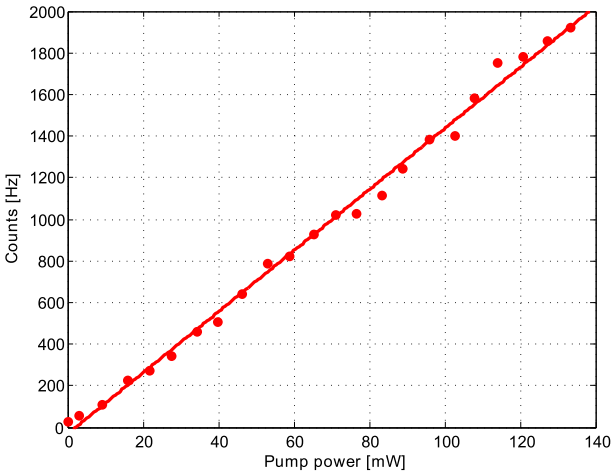

Figure 4.18: Noise level as function of the pump power, with IF1

spectrum.

From the figure 4.18 we can estimate that the rate of noise, in terms of click per ns and per 1 mw of pump power as $3 \times 10^{-6}\, cliks/(ns \cdot mW)$. Taking into account the limited detection efficiency of the SPAD and the transmission of the filtering stage η_{filt}, this correspond to a noise rate produced at the output of the waveguide:

$$\widetilde{R}_{noise} \approx 1 \times 10^{-3} \frac{ph}{ns \cdot mW} \tag{4.12}$$

After this noise estimation and characterization, we started to perform conversion experiments. We will see how this noise affects the SNR in the detection of the converted photons.

4.2.2 Global efficiency

We saw in § 4.1.6 the definition of η_{tot}, that tells us how many 1550 nm photons reach the SPAD with respect to the 780 nm photons that enter the setup. We want now to extend this concept taking into account that not all the photons that reach the SPAD will produce a click[5]. For this purpose, we introduce the global efficiency:

$$\eta_{glob} = \frac{p^{click}}{N_{input}^{780}} \tag{4.13}$$

where p^{click} is the probability to have a click in a gate and N_{input}^{780} is the average number of photons contained in one input 780 nm pulse. I will explain how to measure this quantity in § 4.2.3. We define:

- N_{SPAD}^{1550} the average number of 1550 nm photons per converted pulse that hit the SPAD.
- N_{gate}^{1550} the average number of 1550 nm photons per detection gate that hit the SPAD.
- N_{gate}^{click} the number of photons per gate that can be potentially detected in a gate. It is important to better specify the meaning of this quantity. During one gate the SPAD can only count at most ONE photon. If N_{gate}^{click} is a value well below 1, it represents the probability that we will get a click during the gate. This number is what we measure with the SPAD, evaluating the ratio counts/trigger (excluding the noise). If N_{gate}^{click} is close to 1 or higher, the SPAD will simply saturate, as discussed in the end of § 3.3.4.

We start assuming that N_{input}^{780} is known. Using the (4.9) we can easily calculate:

$$N_{SPAD}^{1550} = \eta_{tot} \cdot N_{input}^{780} \tag{4.14}$$

Then, to calculate N_{gate}^{1550} we have to evaluate the portion β of the pulse that is covered by the gate. We assume that the pulse shape is gaussian with a peak power P_0^{780} and FWHM $= \tau_p$. We consider the gate as a rectangle of length τ, perfectly synchronized (centered) with respect to the pulse. We can calculate β as follows:

$$\beta = \frac{\int_{-\frac{\tau}{2}}^{\frac{\tau}{2}} P_{input}^{780}(t)dt}{\int_{-\infty}^{+\infty} P_{input}^{780}(t)dt} = erf\left(\sqrt{ln2} \cdot \frac{\tau}{\tau_p}\right) \tag{4.15}$$

and so

$$N_{gate}^{1550} = \beta \cdot N_{SPAD}^{1550} \tag{4.16}$$

In figure 4.19 we can see the behavior of β for $\tau_p = 45\,ns$. Then we take into account

[5]The single detection event is commonly called "click" in the SPC language.

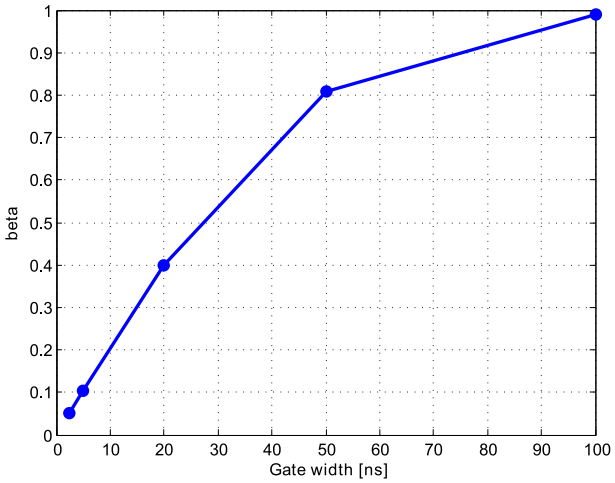

Figure 4.19: Factor beta for a pulse FWHM of 45 ns.

the limited detection efficiency of the SPAD:

$$N_{gate}^{click} = N_{gate}^{1550} \cdot \eta_{det} \tag{4.17}$$

Using these relations, we can now introduce the global efficiency of the setup as follows:

$$N_{gate}^{click} = \eta_{glob} \cdot N_{input}^{780} \tag{4.18}$$

$$\eta_{glob} = \eta_{tot} \cdot \eta_{det} \cdot \beta \tag{4.19}$$

4.2.3 Estimation of the average number of 780 nm photons per input pulse

We can evaluate the average number of 780 nm photons per input pulse as follows:

$$N_{input}^{780} = \frac{E_{wg\,input}^{780}}{h\nu_{780}} \tag{4.20}$$

where $E_{wg\,input}^{780}$ is the energy carried by the pulse. It can be calculated integrating the pulse power profile $P_{input}^{780}(t)$ in time. Again assuming a gaussian profile with height P_0^{780} and FWHM τ_p, the result of the integral can be expressed as:

$$E_{wg\,input}^{780} = P_0 \cdot \tau_p \cdot \sqrt{\frac{\pi}{4 \cdot \ln 2}} \approx P_0^{780} \cdot \tau_p \cdot 1,064 \tag{4.21}$$

and so

$$N_{input}^{780} = 1,064 \cdot \frac{P_0^{780} \cdot \tau_p \cdot \lambda_{780}}{h \cdot c} \tag{4.22}$$

Input power measurement

Evaluating N_{input}^{780} requires the accurate measure of P_0^{780}. We mounted a fast photodiode (PD1) just before the waveguide. With PD1 we can visualize the temporal profile of the light pulse on the oscilloscope ($2,5\,Gsample/sec$, $BW = 1GHz$) and, with the opportune calibration (fig. 4.20), we can measure the peak power without attenuation $\widetilde{P}_0^{780}$. After the attenuation of the 780 nm light with the NDF, a direct

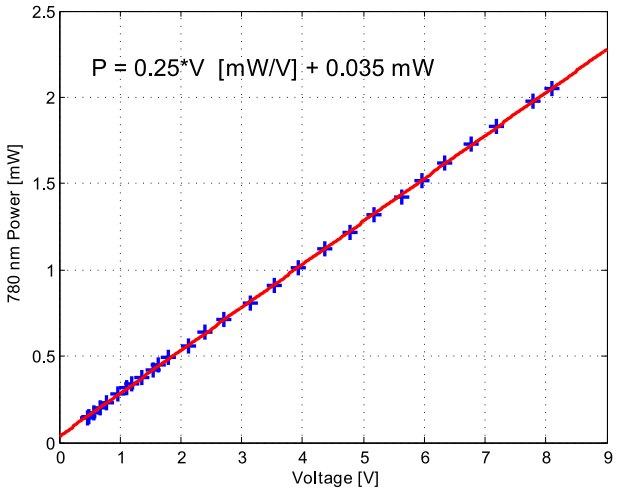

Figure 4.20: PD1 calibration

measure of its power is no longer possible. The way to proceed is to measure the voltage V_{ph} from the photodiode without the NDF, convert it in power, and multiply the result by the transmission of the filters. This is expressed by the formula:

$$P_0^{780} = \widetilde{P}_0^{780} T \tag{4.23}$$

This transmission at 780 nm must be precisely characterized. This characterization is visible in the following table:

Filter name	$\mathbf{P_{bef}^{780}}$	$\mathbf{P_{aft}^{780}}$	**T**	**ΔT/T**	**OD**
A	$34,3\,mW$	$83\,\mu W$	$2,4(2)\cdot 10^{-3}$	7%	6,0
B	$34,3\,mW$	$1,72\,mW$	$5,0(4)\cdot 10^{-2}$	7%	2,9
C	$34,3\,mW$	$1,83\,mW$	$5,3(4)\cdot 10^{-2}$	7%	2,9
$A+B(^*)$	-	-	$1,2(1)\cdot 10^{-4}$	9%	9,0
$A+B+C(^*)$	-	-	$6,4(8)\cdot 10^{-6}$	12%	11,9

I remind the relation $T = e^{-OD}$, where OD (Optical Depth) represent the filter attenuation in logarithmic scale.
When we use a combination of different filters together (*), a direct characterization is impossible due to the resolution of the powermeter. Their transmission is

obtained multiplying the transmissions of the single filters, but of course, the related uncertainty is larger.

Once η_{glob} is known, we can tune $\widetilde{P}^{780}_{input}$ and the NDF transmission to set the expected click probability $N^{clik\,exp}_{gate}$.
Using the formulas 4.18, 4.19 and 4.22, we can write:

$$N^{click\,exp}_{gate} = 1.064\frac{T\widetilde{P}^{780}_0\lambda^{780}\tau_p\eta_{tot}\eta_{det}\beta}{hc} \tag{4.24}$$

We see that its uncertainty is fully related to the uncertainties of η_{tot} and $\widetilde{P}^{780}_0$ and T. We can calculate it as follows:

$$\left(\frac{\Delta N^{click\,exp}_{gate}}{N^{click\,exp}_{gate}}\right)^2 = \left(\frac{\Delta\eta_{eff}}{\eta_{eff}}\right)^2 + \left(\frac{\Delta\widetilde{P}^{780}_0}{\widetilde{P}^{780}_0}\right)^2 + \left(\frac{\Delta T}{T}\right)^2 \tag{4.25}$$

We can quantify the first and the second contributions as 7% and 5% respectively. The third depends from the filter used, according to the table presented in § 4.2.3.

4.2.4 Pulse creation

As we saw in § 3.2.2, we create the 780 nm pulses modulating the intensity of the 780 nm beam by means of the AOM. In particular, with a programmable electronic sequencer, we send a TTL voltage pulse to the amplitude controller input of the RF source connected to the AOM (for the details, see § 3.2.2). The 780 nn light pulse shape is determined by the duration of the TTL pulse. We can choose it setting properly the time interval $t2$ between the instruction "Pulse ON" and "Pulse OFF" in the sequencer program (see fig. 3.16).
Due to the finite rise time of the RF source and of the AOM, for small enough values of t2, the light amplitude will not follow the sharp TTL rectangular signal. This allow to obtain a smoother, almost gaussian light pulse shape. On the other hand, too short values of t2 will not produce any light signal. With t2 = 150 ns we observe a gaussian pulse of $\tau_p = 35,8ns$ (see figure 4.21).

4.2.5 SPAD synchronization

The SPAD detection must be synchronized (i.e. well centered) with the arrival of the 1550 nm converted pulses on the detector. To achieve this, we have to adjust the delay between the pulse generation and the detection gate creation. We can tune this delay choosing two different parameters:

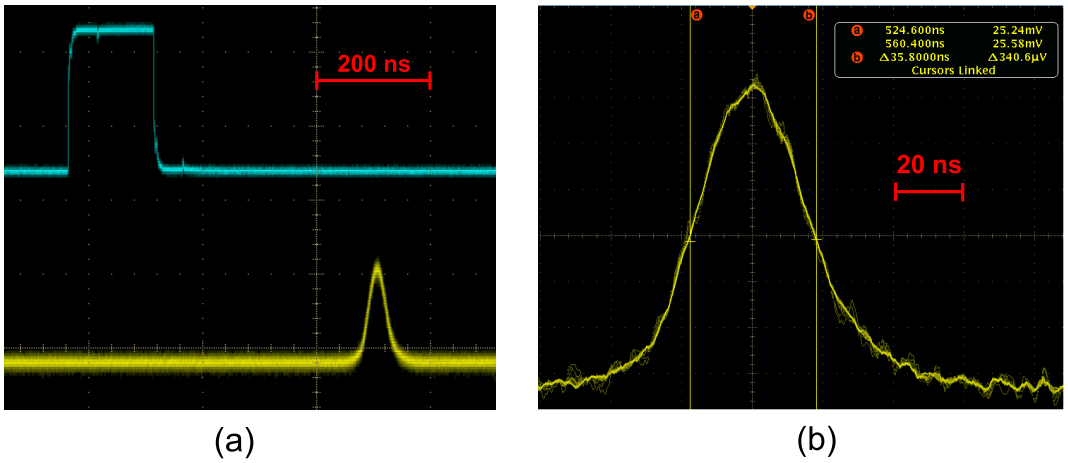

Figure 4.21: Oscilloscope screen shots. (a) The TTL signal (blue) generates the light pulse (yellow) that reaches the photodiode with a certain delay. One horizontal division corresponds to $200ns$. (b) Detail of the pulse created using $t2 = 150ns$. We can observe that $\tau_p = 35.8\,ns$. One horizontal division corresponds to $20ns$. The image is displayed on the oscilloscope with the averaging mode.

- external delay: it is the time interval $t3$ of the sequencer program, between the TTL signal to create the pulse and the trigger. It can be adjusted with a resolution of $10\,ns$;
- internal delay: it is the delay between the arrival of the triggering signal at the external trigger SPD input and the effective creation of the detection gate. This delay is a SPAD parameter and can be adjusted with a resolution of $0.1\,ns$

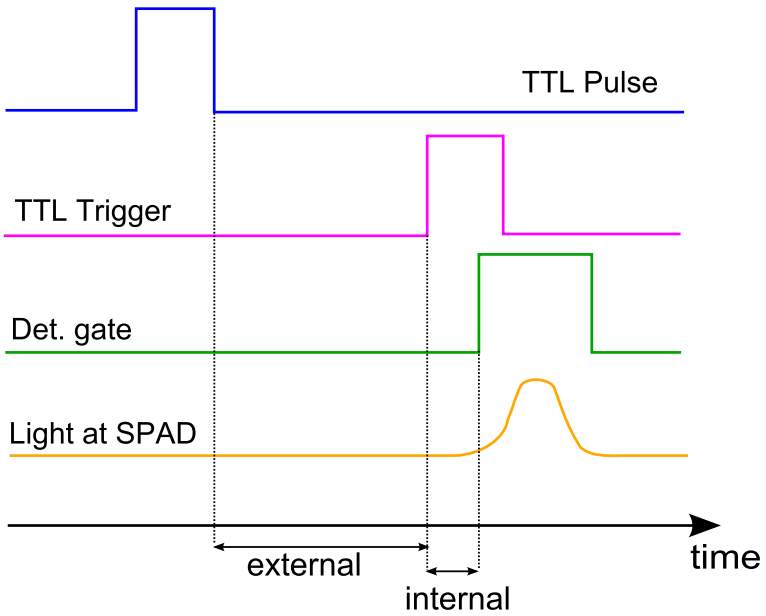

Figure 4.22: Temporal scheme of the synchronization.

In the following table I report the delay settings to obtain a good synchronization, for the different gate width options:

Gate width τ [ns]	**External delay [ns]**	**Internal delay [ns]**
2,5	370	5
5	370	3,7
20	360	5
50	350	1,2
100	320	6,3

The values for $\tau = 2.5ns$ have been determined empirically, measuring the total delay for which the detected signal was maximum. The others have been calculated starting from this.
We then set all the others time intervals of the sequencer program in order to have a trigger rate equal to $500\,kHz$.

4.2.6 SPAD measurement

Before starting to show the experiments carried out with the signal in the simulated quantum regime, it is useful to summarize briefly how a measurement with the SPAD works and to fix few points that will be considered implicit from now on. During a measurement, the SPAD always displays both the value of the triggering rate and the counts rate. Although the triggering rate is fixed, when the dead time is not zero, some gates are lost. So the effective trigger value displayed varies in relation to the count rate registered.
The ratio R between the counts rate and the triggering rate expresses the probability to detect a photon during a gate. This is true only in the linear regime, where this value is well below 1.
When we refer to the measured NOISE, we mean the ratio $R_n$between the counts rate and the triggering rate with the pump ON and the 780 nm light OFF.
When we refer to the measured SIGNAL R_s, we mean the difference between the ratio R_c of counts and trigger with all the laser ON and the noise (as defined above). We will call it also $N_{gate}^{click\,meas}$. This signal value is proportional to the area of the pulse covered during a detection gate.
When we refer to signal to noise ratio (SNR), we mean the ratio between signal and noise, according to the previous definitions.
When we refer to $N_{gate}^{click\,exp}$, we mean the value of the signal that we expect by choosing the input 780 nm power and the NDF attenuation.

When not explicitly specified, the following SPAD parameters have been set as follows:

- $\eta_{det} = 10\%$;
- dead time $= 20\mu s$;
- external trigger at 500 kHz.

4.2.7 Spad uncertainty

We analyze now the uncertainty related to the quantities measured with the SPAD.
Let us suppose we are operating with a dead time τ_d, and a set trigger rate T_0 that are known with negligible uncertainty. C and T are the counts and trigger displayed by the SPAD and R is their ratio. For given C we can estimate T as follows:

- $1/T_0 = \tau_m$ is the mean time before two gates, without dead time;
- $\tau_d/\tau_m = \tau_d T_0$ is the number of gates lost during one dead time;
- $T_L = C\tau_d T_0$ is total number of gates lost, because the SPAD fixes the dead time after each click;
- $T = T_0 - T_L = T_0 - C\tau_d T_0$ is an estimation of the trigger rate displayed.

As discussed in § 2.2.3, the variance associated to the photon count events C is related to the Poissonian distribution of photons in coherent light.

$$\Delta C = \sqrt{C} \tag{4.26}$$

From the previous discussion arises that:

$$\Delta T = \tau_d T_0 \Delta C = \tau_d T_0 \sqrt{C} \tag{4.27}$$

Now let consider R. Due to the correlation between T and C, it can be rewritten as follows:

$$R = \frac{C}{T} = \frac{C}{T_0 - C\tau_d T_0} \tag{4.28}$$

We see that the only quantity that contribute in its uncertainty is C. We can calculate it:

$$\begin{aligned} \Delta R \ &= \sqrt{\left(\tfrac{\partial R}{\partial C}\right)^2 (\Delta C)^2} = \tfrac{T_0}{(T_0 - T_0\tau_d C)^2}\Delta C = \tfrac{T_0}{(T_0 - T_0\tau_d C)^2}\Delta C = \tfrac{T_0}{T^2}\Delta C \\ &= \sqrt{C}\tfrac{T_0}{T^2} \end{aligned} \tag{4.29}$$

Let us now consider the signal, defined in the previous paragraph as $S = R - R_n$. It follows that:

$$\Delta S = \sqrt{(\Delta R)^2 + (\Delta R_{noise})^2} \tag{4.30}$$

Finally, we can evaluate the uncertainty on the SNR:

$$\begin{aligned} \Delta SNR &= \Delta\left(\frac{S}{N}\right) = \frac{R-R_n}{R_n} = \sqrt{\left(\frac{\partial SNR}{\partial R}\right)^2 (\Delta R)^2 + \left(\frac{\partial SNR}{\partial R_n}\right)^2 (\Delta R_n)^2} \\ &= \frac{\sqrt{(\Delta R)^2 + R^2(\Delta R_n)^2}}{R_n} \end{aligned} \tag{4.31}$$

In the followings, all the uncertainties related to measurements performed with the SPAD will be calculated using these formulas.

4.2.8 Pulse reconstruction

The first measurement we did with the pulsed signal was to try to reconstruct the shape of the attenuated pulses. To do this we set the input peak power $\widetilde{P}_0^{780} = 22.5\mu W$ and the attenuation to OD=6. This configuration corresponds to $N_{input}^{780} \approx 9 \times 10^3 photons/pulse$ for pulses of $\tau_p = 35,8\, ns$. Then we chose the shortest detection gate available ($\tau = 2,5ns$) and we observed the behavior of the ratio counts/trigger varying the synchronization delay over a wide range (150 ns), centered where we expect to observe the maximum signal, with steps of 2.5 ns. For every delay value, we recorded both signal and noise and the results are visible in figure 4.23. First of all we observe that the noise level, as expected, is uniform in

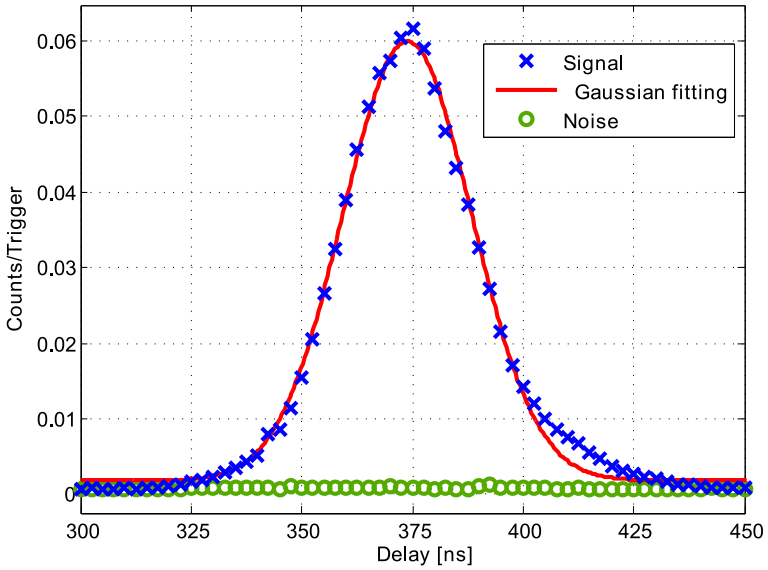

Figure 4.23: Pulse shape reconstruction obtained varying the delay between the pulse generation and the detection gate. The duration of the latter has been set on 2.5 ns.

time. Second, we can see that, for the N_{input}^{780} we chose, we have a SNR well above 1,

and, in the meantime, the max $N_{gate}^{click\,meas}$ registered is low enough to consider that we worked in the linear regime. Then we confirmed that the maximum of the signal is observed for a total delay of 375 ns, in agreement with the table of § 4.2.5.
Since the gate and the step durations chosen for the measurement are smaller compared to the width of the pulse, we can assume that the signal behavior is a good reconstruction of the temporal shape of the pulse[6]. This is confirmed by the gaussian fitting whose FWHM is close to the τ_p of the pulse set.

4.2.9 Comparison between expected and measured count rates

The second measurement we did in the pulsed regime was to check if the characterization of η_{tot} in the classical regime agrees with the results we obtain for the simulated quantum regime. To do this, we measured $N_{gate}^{click\,meas}$ with different τ, keeping fixed $N_{gate}^{click\,exp} = 0.25(3)$.
$N_{gate}^{click\,exp}$ depends from τ itself via the β factor (see eq. 4.18 and 4.19). So, in order to maintain it fixed during the measurement, we had to adjust $\widetilde{P}_0^{780}$ and T consequently. In particular we varied the former, keeping $T = 9.02\,OD$. In figure we can see the results: We immediately notice that there is a discrepancy between

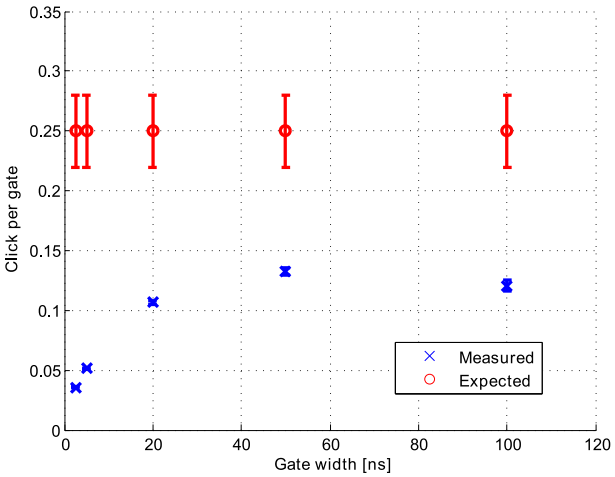

Figure 4.24: Comparison between measured and expected click per gate.

$N_{gate}^{click\,exp}$ and $N_{gate}^{click\,meas}$. We define the factor f as the ratio of the two values. In figure 4.25 we can see how this varies with τ. We relate this difference to others unknown losses in the setup, eg. the coupling of the light from the SPAD input

[6]Since the signal is proportional to the gated area of the pulse, the measured shape is the temporal convolution between the pulse and the gate. In the limit of short gate, the result tends to the pulse shape.

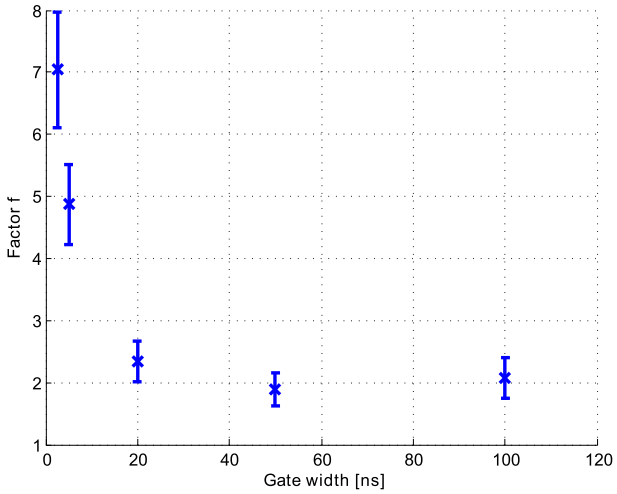

Figure 4.25: f factor in function of τ.

connector to the absorption area of the photodiode. We see that this discrepancy is much more accentuated when the gate is shorter. We suppose that this effect is due to the non ideal rectangular shape of the SPAD gate. It becomes less regular when it is shorter, due to the electronics limits of the device.

4.2.10 SNR and gate width

We then wanted to study the dependence of the SNR from the gate width choice. So we fixed N_{input}^{780} and we observed the variation of SNR for the different τ. Again we kept fixed the attenuation to OD 9,02 and repeated the experiment for three different values of N_{input}^{780}: 452(59) ph/pulse, 650(84) ph/pulse and 250(32) ph/pulse. In this measurement, the pulse FWHM was 45 ns and the $\eta_{tot} = 0.51(4)\%$. We can see the result in the picture. We can observe, as we expected, that SNR decreases for larger values of τ. The drop is more accentuated after $\tau = 20\,ns$. This fact is easily explainable by the fact that, for wider gates, the noise increases linearly (since it is uniformly distributed in time). On the other hands the signal detected increases slower and slower, because we are just gating more and more the tails of the pulses. However, too short τ affect the η_{glob} of the setup, due to the repercussions on the factor β and the factor f that we discussed in the previous paragraph. Because of this trade off, we decided that $\tau = 20ns$ is the optimum choice for the gate width in our experiment.

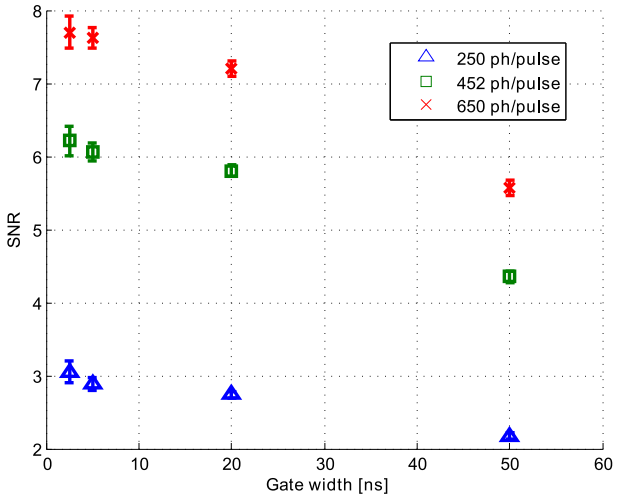

Figure 4.26: SNR in function of gate width, for different input photons per pulse

4.2.11 Conversion performances

At this point we want to test to what extent we can reduce N_{input}^{780}, being still above the noise level. We use photons with duration 45 ns (FWHM) and detection gate width $\tau = 20$ ns. The value of η_{glob} was optimized to 0.043(3)%[7], with $P_{coup}^{1550} = 146(7)\,mW$. First we set the attenuation to OD=9.02, then we measured signal and noise, varying the input number of photons. In figure 4.27 we can se the results. We see that the noise level remains constants, while the signal grows

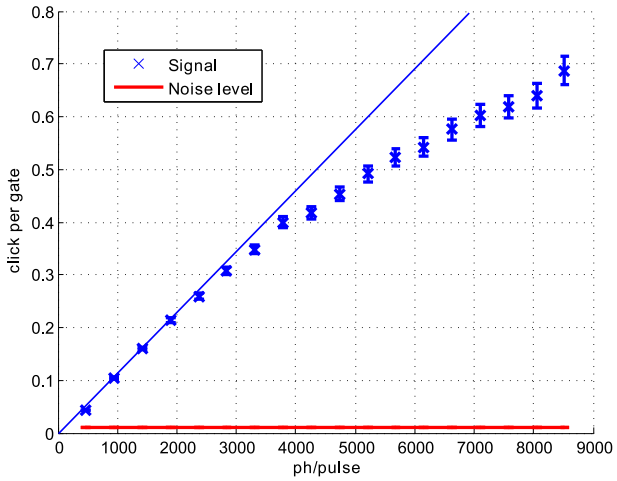

Figure 4.27: Signal detected as function of input average number of photons per pulse, with 20 ns gate width.

linearly for low values of N_{input}^{780} and then it saturates the SPAD functioning. We see that it starts to deviate from the linear regime for $N_{gate}^{click\,meas} > 0.3$. We can use this value to fix the threshold of linear functioning.

[7]Not including the f factor.

We then observed the behavior of the SNR for $\tau = 2.5, 5, 20\,ns$. The results are visible in figure 4.28: We then changed the value of the NDF attenuation to OD=11.9

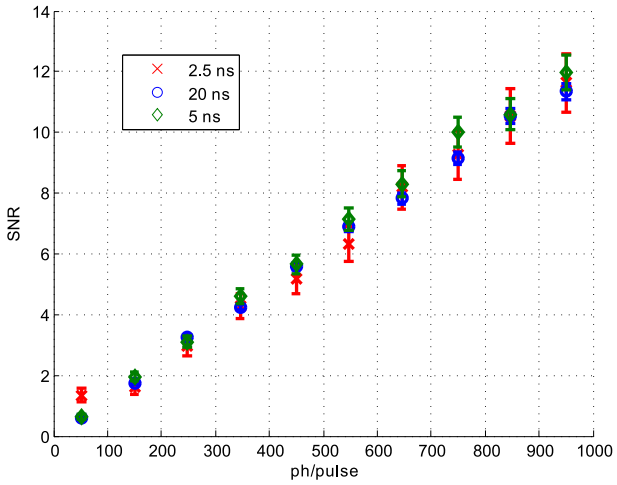

Figure 4.28: SNR in function average input photons per pulse, for different values of gate width.

and we further reduced N_{input}^{780} to see when SNR drops below 1. We did this measurement with $\tau = 20ns$. The result is visible in picture 4.29. The linear fit (done

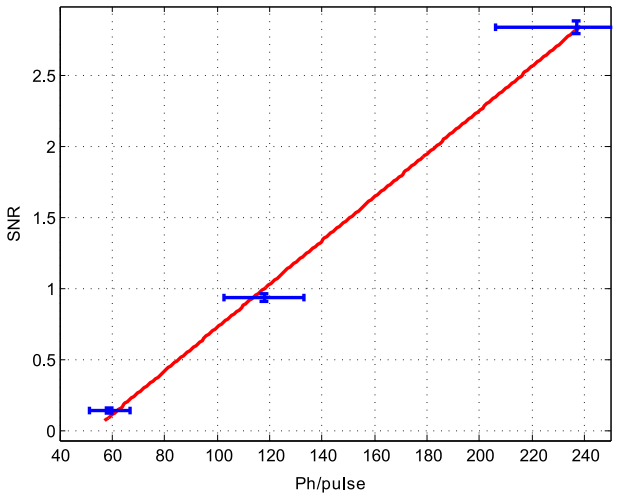

Figure 4.29: SNR in function average input photons per pulse, in a region close to SNR = 1.

with Matlab fitting toolbox) gives the equation:

$$SNR = 0.015(8) \cdot N_{input}^{780} - 0.8(1) \tag{4.32}$$

With this we can calculate the input average photons per pulse to have SNR 1 and we obtain:

$$N_{input}^{780} = 120(16)\, ph/pulse \tag{4.33}$$

From this measurement we can state that, with our setup, we are able to measure the wavelength conversion of weak coherent 780 nm pulses of 45 ns containing approxi-

mately 10^2 average number of photons per pulse. This is still far from the situation required to use this device as quantum frequency converter ($N_{input}^{780}780 < 1$). In sections **??** we will propose ways to decrease the noise.

4.2.12 Photon length

Finally, we wanted to see how the photons length influences the SNR of the detection. However, as mentioned previously the minimal pulse width we can create is around 35 ns. In order to overcome this limitation and simulate shorter pulses, we operate the 780 light in cw and vary the detection gate duration.
In this regime we have to consider the β factor (see § 4.2.2) always equal to 1 and the calculation of the average input photons per gate width is simply obtained as:

$$N_{input}^{780} = \frac{P_0^{780}}{h\nu_{780}}\tau \tag{4.34}$$

We fixed the internal trigger of the SPAD to 1 MHz and we optimized the setup to $\eta_{tot} = 0.59(3)\%$. Similarly to what we did in § 4.2.9, we varied the gate width, keeping fixed $N_{gate}^{click\,exp} = 0.3$ with a fixed attenuation OD=9.02 and adjusting consequently the input power $\widetilde{P}_{input}^{780}$. We then observed how the SNR behaves as function of the τ.
Since the signal that hit the SPAD per gate is constant, this experiment is equivalent to test the SNR of the detection with respect to the photons length, that in this case is determined by the width of the gates themselves.
In figure 4.30 we can see the result: What we observe is that SNR increases when

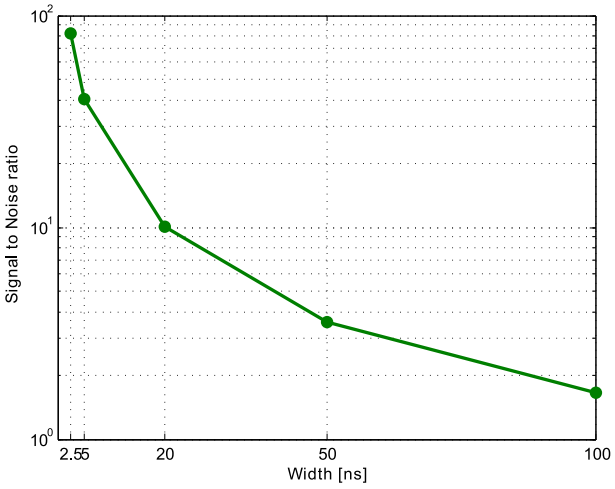

Figure 4.30: SNR in function of gate width.

the gate is smaller and, from this, we can infer that the photon detection is favored when the photons are shorter. This is perfectly reasonable, if we consider that, with

shorter photons, we concentrate the same energy in a shorter duration while the noise decreases linearly with the detection gate.
However, the photon duration is a limited degree of freedom for us, since the photons are emitted by atoms.

RESULTS DISCUSSION AND CONCLUSIONS

Experimental results discussion

In the experiment we carried out we could perform the wavelength conversion of weak coherent pulses from 780 nm to 1550 nm. However, the noise level and the conversion efficiency of the setup limit the SNR of the detection of the converted light and we are not able to resolve the conversion of input pulses containing an average number of photons smaller than $10^2\,ph$. In these conditions the setup is not suitable to perform the quantum frequency conversion of single photons, with the fidelity required for the preservation of their quantum state. To achieve this goal we must improve the SNR to be able to detect the conversion of pulses that contain a mean number of photons below 1.

Noise Reduction

The first way to improve SNR is to reduce the noise due to spurious light arriving at the SPAD. For that purpose, further noise characterization measurements[8] , with only the pump light on, have been carried out, to better understand which is the main noise source in our experiment. Another narrow band pass filter at 1570 nm (identical to IF1) mounted before the waveguide didn't produce any appreciable effect on the noise counts registered by the SPAD. This means that the contribution due to the amplified spontaneous emission in the EDFA is not the main cause.

[8]these measurements have been carried out by Marcel · lí Grimau Puigibert, a Physics master student at the "Universitat de Barcelona" (UB), that joined the project as "Caixa Catalunya ICFO Summer Fellow".

On the contrary, the same filter mounted after the waveguide caused a significant reduction (factor 7) of them. This proved that the main noise source that affects our setup is represented by spurious light close to 1550 nm that is generated inside the PP-KTP crystal most likely via Raman scattering due to the presence of the pump.
In § 4.2.1 we estimated the noise at the output of the crystal as $\widetilde{R}_{noise}^{KTP} \approx 10^{-3}\, ph/(ns \cdot mW)$. Using the data presented in [56] we can make the same estimation for the Raman scattering noise generated in a PP-LN crystal and we obtain $\widetilde{R}_{noise}^{LN} \approx 3.5 \times 10^{-5}\, ph/(ns \cdot mW)$. First of all we notice that using 450 mw of pump power, we produce a noise count probability of $1.3 \times 10^{-3}\, (ns)^{-1}$. If we compare this result with the dark count probability, estimated in § 4.2.1 to be equal to $7 \times 10^{-6}\, (ns)^{-1}$, we see that the latter at this point is negligible. We can also see that the noise rate produced at the output of our PP-KTP waveguide is much higher (factor 20) than of a PP-LN waveguide. However, from this comparison we cannot state that PP-LN is in general better than PP-KTP because we operated with different wavelengths and the Raman spectrum is very sensitive to this parameter [59]. We observed that another diffraction grating mounted after the waveguide reduces the noise counts of a factor 5. This suggests that a more accurate narrow spectral filtering (e.g. with fiber Bragg gratings) of the converted light after the waveguide could give a good contribution in the noise suppression.
Another possibility could be to change operating wavelengths, e.g. using a pump at 1565 nm, to convert the light from 780 nm to 1555 nm, still in the telecom C-band. Studies on the Raman spectrum of KTP [59] shows that operating with closer wavelengths for the pump and the generated light reduces significantly the Raman scattering noise. We should especially measure the Raman noise for our crystal, using e.g. a monocromator, in order to better choose a suitable wavelength combination.
We highlight again that our experiment has much more stringent requirements in terms of noise suppression with respect to the others presented in §1.3, because of the characteristics of the photons (mainly longer duration and narrower spectrum) that we want to convert. In fact we demonstrated in § 4.2.12 that the SNR of the detection drops when the photon duration is increased.

Efficiency

We saw in § 4.1.4 that the maximum conversion efficiency of our setup is limited to 14 %. This represent an improvement with respect to similar experiment published in 2010 ([54],[55]), but it is well below the conversion efficiencies of around

60-70 % reported in 2011 ([56], [57]). The main limiting factor in this feature for us is the small generation efficiency η_{gen} of the crystal. Note that some PP-KTP crystals exhibit much higher efficiencies. For example, another crystal used in our lab for another experiment exhibited a conversion efficiency of 400 %/W, while we are limited to 45 %/W. A possible solution, thus, could be to use a different PP-KTP crystal with a higher value of η_{norm}. This would permit to achieve a higher conversion efficiency with lower pump power that leads also to a less generation of Raman noise.

Regarding our actual crystal, we can use what we discussed in § 2.1.6 to estimate the pump power for which we reach the total conversion of the beam at 780 nm. We compare the expressions (4.5) and (2.43) related to the weak interaction regime, to calculate η_{norm}:

$$\eta_{norm} = \frac{\eta_{gen}\frac{\lambda_{1550}}{\lambda_{780}}}{L^2} = 0.13\,\frac{1}{W cm^2} \tag{4.35}$$

We used the nominal value for $L = 2.6\,cm$ for the length of the waveguide. In figure 4.31 we can see the plot of the 2.42, using our experimental parameters. With the

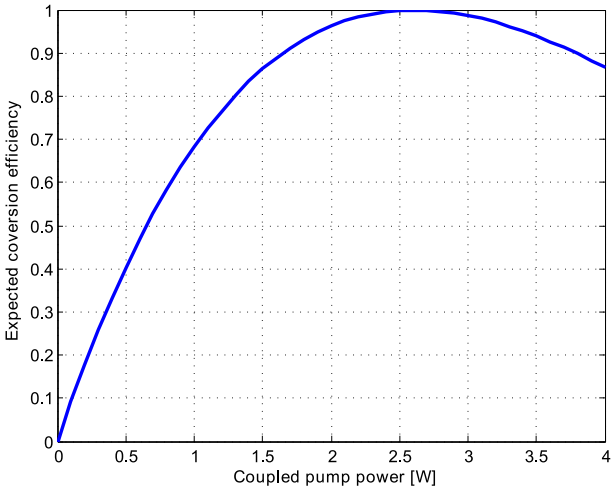

Figure 4.31: Theoretical behavior of the conversion efficiency in function of the pump power, considering $\eta_{norm} = 0.13$ and $L = 2.6\,cm$.

value calculated for η_{norm}, we can use eq. 2.44 to calculate the pump power that leads to 100 % conversion efficiency:

$$P_{max}^{1570} = \frac{\pi^2}{4\eta_{norm}L^2} = 2,8\,W \tag{4.36}$$

We see that we are considerably far from this value. This means that we can improve η_{conv} improving either the coupling of the pump in the waveguide or using a more powerful pump source. Note that this factor alone will not improve the SNR, since the noise is proportional to the pump power

In order to increase the coupling efficiencies of pump and and signal into the waveguide (both limited to 30 %), we could replace the 11 mm focal aspheric lens (AL1), that we use to focus the beams on the waveguide facet, with a more sophisticated microscope objective, specially designed to compensate both spherical and chromatical aberrations, for for the two wavelengths simultaneously. In addition, a mode shaping of the two beams implemented with proper telescopes, can help in the coupling efficiencies improvement.
Finally we mention that there is still room for improvement for the losses after the waveguide (identified with $\eta_{filt} = 14\%$), e.g. optimizing the diffraction efficiency, the fiber coupling and the fiber connection to the single photon detector.

Conclusions and future perspective

In this work we demonstrated the frequency down conversion of photons having the required spectral and temporal properties to be compatible with atomic quantum memories. In particular, we performed the conversion of weak coherent pulses (45 ns FWHM) from 780 nm to 1550 nm, via difference frequency generation in a non linear PP-KTP crystal. The maximum internal conversion efficiency we observed is 14 %. Taking into account all the optical losses (excluding detection), the device efficiency drops to 0.6 %. We believe that the optical noise that affects our measurements arises mainly from Raman scattering of the pump inside the crystal and it prevents us to detect the conversion of pulses that contain an average number of photons smaller than 100. This limits the fidelity of our setup below the threshold to work as quantum device and thus, at the state of the art, it cannot be used as quantum frequency converter for single photons. Nevertheless, with this experiment, we could understand which are the most critical limiting factors and we identified some ways to improve the actual performances. We believe that, working in this direction, it is possible to enhance the SNR of the setup, up to the level required to operate at the single photon level. When such a result is achieved, it will be necessary to demonstrate that the conversion maintains the phase of the input pulses, with interferometric experiments. Finally, if we can significantly reduce the noise, the down conversion will be realized on non classical light (single photons) emitted by the atomic ensemble. In case of success, we will have realized a quantum frequency converter suitable for quantum repeater applications.

BIBLIOGRAPHY

[1] Sangouard N., Simon C., de Riedmatten H., and Gisin N. Quantum repeater based on atomic ensembles and linear optics. *Rewew of modern physics*, 83, 33, 2011. part I.

[2] Sangouard N., Simon C., de Riedmatten H., and Gisin N. Quantum repeater based on atomic ensembles and linear optics. *Rewew of modern physics*, 83, 33, 2011. part IV.

[3] Sangouard N., Simon C., de Riedmatten H., and Gisin N. Quantum repeater based on atomic ensembles and linear optics. *Rewew of modern physics*, 83, 33, 2011. part II.

[4] Bouwmeeste D., Ekert A., and Zeilinger A. *The physics of quantum computation*, chapter Preface. Springer, 2000.

[5] Benenti G., Casati G., and Strini G. *Principles of quantum computation and information, vol I*, chapter introduction. World scientific, 2004.

[6] Feynman R. Simulating phisics with computers. *Int. J. Theor. Phys.*, 21.467, 1982.

[7] Shor P. W. Polynomial-time algorithms for prime fctorization and discrete logarithms on a quantum computer. *SIAM J. Sci. Statist. Comput.*, 26, 1484, 1997.

[8] Grover L. K. Quantum mechanics helps in searching for a needle in a haystack. *Phis. Rev. Lett.*, 79, 327, 1997.

[9] Bennet C. H. and Brassard G. Quantum cryptography: public key distribution and coin tossing. In *Int. conf, systems and signal processing*, 1984. New York.

[10] Bouwmeeste D., Ekert A., and Zeilinger A. *The physics of quantum computation*, chapter 1.3. Springer, 2000.

[11] Benenti G., Casati G., and Strini G. *Principles of quantum computation and information, vol I*, chapter 3.1. World scientific, 2004.

[12] Griffhits D. J. *Introduction to quantum mechanics*, chapter Afterword. Prentice Hall, 1995.

[13] Einstein A., Podolsky B., and Rosen N. Can quantum mechanical decription of physical reality be conserdered complete? *Phis. Rev.*, 47, 777, 1935.

[14] Bohr N. Can quantum mechanical decription of physical reality be conserdered complete? *Phis. Rev.*, 48, 696, 1935.

[15] Bell J. S. On the einstein-podolsky-rosen paradox. *Phisics*, 1, 195, 1964.

[16] Weihs G et al. Violation of bell's inequality under strict einstein locality conditions. *Phis. Rev. Lett.*, 81, 5039, 1998.

[17] Aspect A. et al. Experimental tests of realistic local theories via bell's theorem. *Phis. Rev.*, 47,460, 1981.

[18] Benenti G., Casati G., and Strini G. *Principles of quantum computation and information, vol I*, chapter 4.2. World scientific, 2004.

[19] Wootters W. K. and Zurek W. H. A single quantum cannot be cloned. *Nature*, 299, 941, 1982.

[20] Gisin N. and Massar S. Optimal quantum cloning machine. *Phys. Rev. Lett.*, 74, 145, 2002.

[21] Benenti G., Casati G., and Strini G. *Principles of quantum computation and information, vol II*, chapter 6. World scientific, 2004.

[22] Cirac J. J. and Zoller P. Quantum computation withs with cold trapped ions. *Phys. Rev. Lett.*, 74, 4091, 1995.

[23] Zhang C., Rolston S. L., and Das sarma S.l. Manipulation of single neutral atoms in optical lattices. *Phys. rev. A*, 74, 042316, 2006.

[24] Jones J.A. Nmr quantum computation. *Prog. NMR spectr.*, 38, 325, 2001.

[25] Yamamoto T. et al. Demonstration of conditional gate operation using superconducting charge qubits. *Nature*, 425, 941, 2003.

[26] Loss D. and Di Vinceno D. P. Quantum computation with quantum dots. *Phys. Rev. A*, 57, 120, 1998.

[27] Zalka C. Efficient simulation of quantum systems by quantum computers. *Fortschr. Phys.*, 46, 877, 1998.

[28] Vandersypen et al. Experimental realization of shor's quantum factoring algorithm using nuclear magnetic resonance. *Nature*, 414, 803, 2001.

[29] Simon J. et al. Quantum simulation of antiferromagnetic spin chains in an optical lattice. *Nature*, 472, 307, 2011.

[30] Stucki D., Gisin N., Guinnard O., Ribordy G., and Zbinden H. Quantum key distribution over 67 km with a plug and play system. *New Journal of Physics*, 4, 41, 2002.

[31] Elliott C., Colvin A., Pearson D., Pikalo O., Schlafer J., and Yeh H. Current status of the darpa quantum network, 2005.

[32] Bennet C. H. and Wiesner S. J. Cmmunication via one- and two- particle opertors on einstein podolsky rosen states. *Phys. rew. Lett.*, 69, 2881, 1992.

[33] Bennet C.H. et al. Teleporting an unknown quantum state via dual classical epr channels. *Phys. Rew. Lett.*, 70, 1895, 1993.

[34] Mattle K. et al. Dense coding in experimental quantum communication. *Phys. Rew. Lett.*, 76, 4656, 1996.

[35] Boschi D. et al. Experimental realization of teleporting an unknown pure quantum state via dual classical and epr channels. *Phys. Rew. Lett.*, 80, 1121, 1998.

[36] Gisin N. et al. Quantum cryptography. *Reviews of modern physics*, 74, 145, 2002.

[37] Shannon C. Communication theory of secrecy systems. *Bell System Technical Journal*, 28, 656, 1949.

[38] Trappe W. and Washington L.. *Introduction to cryptography with coding theory.* Pearson education, 2006.

[39] Ekert A. K. et al. Quantum cryptography based on bell's theorem. *Phys. Rew. Lett.*, 67, 661.

[40] Lydersen L. et al. Hacking commercial quantum cryptography systems by tailored bright illumination. *Nat. Photonics*, 4, 686.

[41] Valerio Scarani, Helle Bechmann-pasquinucci, Nicolas J. Cerf, Miloslav Dušek, Norbert Lütkenhaus, and Momtchil Peev. The security of practical quantum key distribution, 2009.

[42] Briegel H. J. et al. Quantum repeaters: the role of imperfect local operations in quantum communication. *Phys. Rew. Lett.*, 46, 493.

[43] Sangouard N., Simon C., de Riedmatten H., and Gisin N. Quantum repeater based on atomic ensembles and linear optics. *Rewew of modern physics*, 83, 33, 2011. part V.

[44] Duan L. M., Lukin M. D. aand Cirac J. I., and Zoller P. Long distance quantum communication with atomic ensembles and linear optics. *Nature*, 414, 413, 2001.

[45] De Riedmatten H., Afzelius M., Staudt M., Simon C, and Gisin N. A solid state light matter interface at the single photon level. *Nature*, 456, 773, 2008.

[46] Lan S. Y. et al. A multiplexed quantum memory. *Optics Expres*, 17, 16, 2009.

[47] Lauritzen B. et al. Telecommunication-wavelength solid-state memory at the single photon level. *Phys. Rev. Lett.*, 104,080502, 2010. part IV.

[48] Rostilav V. et al. Periodically poled lithium niobate waveguide sum-frequency generator for efficient single-photon detection at communication wavelength. *Optics letters*, 29, 13, 2004.

[49] Langrock C. et al. Higlhy efficiet single-photon detection at communication wavelengths by use of up-conversion in reverse-proton-exchanged periodically poled linbo3 waveguides. *Optics letters*, 30, 13, 2005.

[50] Tanzilli S. et al. A photonic quantum information interface. *Nature*, 437, 116, 2005.

[51] Rakher M. et al. Simultaneous wavelength translation and amplitude modulation of single photons from a quantum dot. *Quant. Photonics*, 786, 2010.

[52] McGuinness H. J. et al. Quantum frequency translation of single-photon states in a photonic crystal fiber. *Phys. Rev. Lett.*, 105, 093604, 2010.

[53] Ding Y. and Ou Z. Y. Frequency downconversion for a quantum network. *Optics Letters*, 35, 2591, 2010.

[54] Kurtz N., Thew R., Simon C., Gisin N., and Zbinden H. Coherent frequency-down-conversion interface for quantum repeaters. *Optic express*, 18, 2010.

[55] Takesue H. Single photon frequency dow-conversion experiment. *Physical review A*, 82, 2010.

[56] Zaske S., Lenhard A., and Becher C. Efficient frequency downconversion at the single photon level from the red spectral range to the telecommunications c-band. *Optics Expres*, 19, 13, 2011.

[57] Ikuta R. et al. Wide-band quantum interface for visible-to-telecommunication wavelength conversion. preprint (9 June 2011), available at url = http://arxiv.org/abs/1106.1758.

[58] Radnaev A. G. et al. A quantum memory with telecom-wavelength conversion. *Nature physics*, 6, 894, 2010.

[59] Savatinova I. et al. A comparative analysis of rb:ktp and cs:ktp optical waveguides. *J. Phys. D: Appl. Phys.*, 31, 1667, 1998.